Advanced Optical Imaging with Scattering Lenses

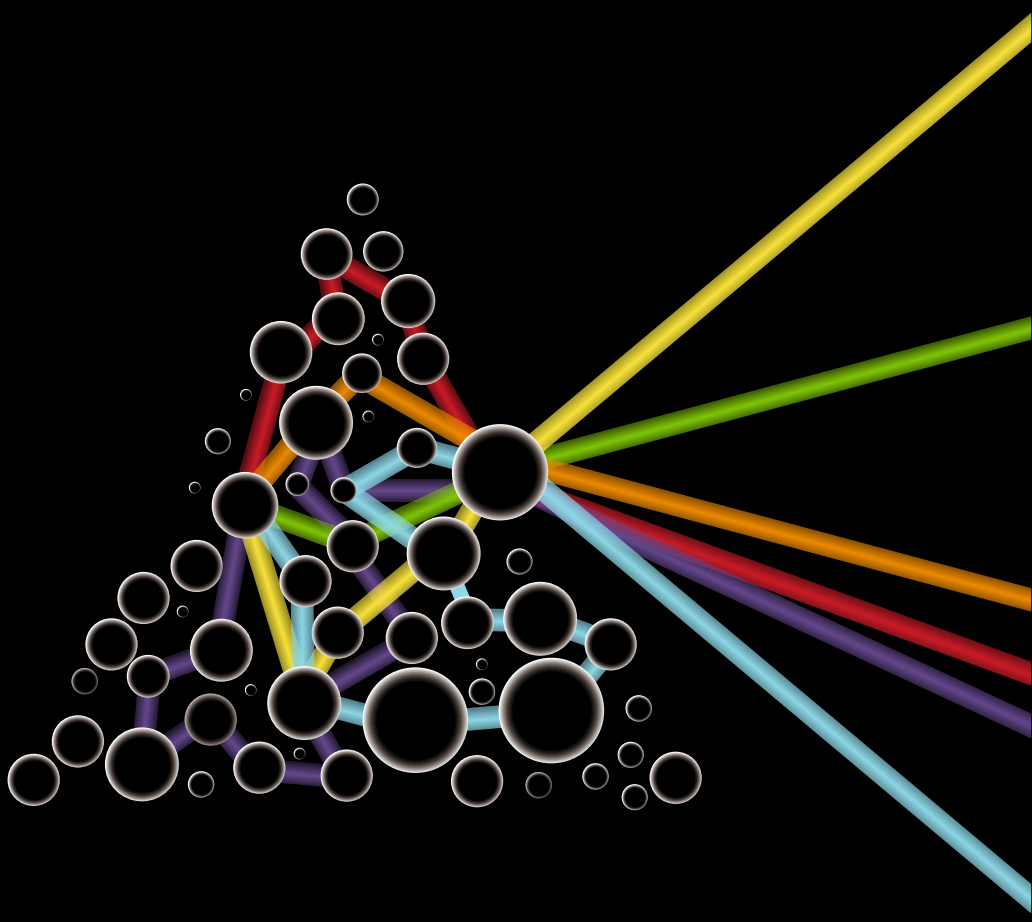

Hasan Yılmaz

ADVANCED OPTICAL IMAGING WITH SCATTERING LENSES

Geavanceerd Optisch Afbeelden met Verstrooiende Lenzen

Promotiecommissie

Promotor	Prof. Dr. A. P. Mosk
Overige leden	Dr. J. Bertolotti
	Prof. Dr. R. Carminati
	Prof. Dr. W. M. J. M. Coene
	Prof. Dr. A. Lagendijk
	Dr. S. Manohar
	Prof. Dr. W. L. Vos

The work described in this thesis is financially supported by the stichting FOM
which is financially supported by the
'Nederlandse Organisatie voor Wetenschappelijk Onderzoek' (NWO).
Additional funding is provided by ERC, ANP, and MESA+.

It was carried out at the
Complex Photonic Systems Group,
Department of Science and Technology
and MESA+ Institute for Nanotechnology,
University of Twente, P.O. Box 217,
7500 AE Enschede, The Netherlands.

ADVANCED IMAGING WITH SCATTERING LENSES

PROEFSCHRIFT

ter verkrijging van
de graad van doctor aan de Universiteit Twente,
op gezag van de rector magnificus,
prof. dr. H. Brinksma,
volgens besluit van het College voor Promoties
in het openbaar te verdedigen
op woensdag 1 juli 2015 om 14.45 uur

door

Hasan Yılmaz

geboren op 23 mei 1985
te Çanakkale, Turkije

Dit proefschrift is goedgekeurd door:

Prof. Dr. A. P. Mosk

"All of the books in the world contain
no more information than is broadcast as video
in a single large American city in a single year.
Not all bits have equal value."

Carl Sagan

Contents

CHAPTER 1
Introduction

Understanding sight has been a great interest among humankind for centuries. It has already been known centuries ago that light travels in straight lines. However, there have been contradicting theories on how the image of an object is seen. According to extramission theory, the image of an object was constructed by light rays emitted by the eyes. Later, this theory was replaced by intromission theory which states the image of an object is constructed by light rays emitted by the object. Today we know that image formation is accomplished by the detection of light waves that are emitted or scattered by a physical object. In the science of optics we study how light waves scatter, propagate, and form an image of an object [1–5].

The invention of the compound microscope has revolutionized our understanding of image formation and enabled visualization of microscopic objects such as bacteria [6]. An enormous research effort has been made to enhance the spatial resolution of optical microscopes much of it by perfection of glass optics and eliminating scattering. With the emergence of information technology, optical information can be digitized and computationally processed. Several high-resolution microscopy methods that benefit from image processing algorithms have been developed.

In this thesis, we introduce new high-resolution optical imaging methods that are based on computational processing of optical information that is gathered by spatial control of light scattering through disordered materials. The combination of new optical methods with information technology now extends our sight to the nanometer-scale regime.

1.1 Optical imaging

Non-invasive investigation of morphology and function of structures with a high spatial resolution is essential in materials science, life sciences, and medical diagnosis [7]. Optical imaging has the advantage of high spatial resolution and non-invasive characterization. However, the standard resolution of optical systems is still low compared to invasive methods such as electron microscopy [8, 9], X-ray imaging [10], near-field optical microscopy [11, 12], or atomic force microscopy [13]. Several methods have been developed to enhance the resolution of optical imaging systems [14–23]. However, these methods either require labeling of structures using dyes with specific photophysics or are very sensitive to optical

aberrations that are introduced by samples. With adaptive optics, aberrations of low order can be compensated [24, 25]. In a regime that strongly scattering is involved, low order aberration compensation approach of adaptive optics is insufficient. With the technological advancement of the spatial light modulators (SLM), high order aberrations can be compensated [26] and surprisingly light propagation can be controlled through strongly scattering materials [27, 28]. It has been shown that the transmission matrix of an arbitrarily complex scattering medium can be measured [29, 30] which allows reconstruction of high-resolution images through strongly scattering media [31–33].

1.2 Optical resolution

Resolution is an essential property of an optical imaging system. Resolution defines the ability of the imaging system to separate the presence of two adjacent source points of an object. In principle, diffraction limits the resolution of a conventional optical imaging system [34, 35]. However, optical aberrations and signal-to-noise ratio are limiting factors in many practical cases [36–39]. In a conventional optical imaging system with good signal-to-noise and no aberrations, the diffraction-limited resolution is determined by the numerical aperture (NA $= n\sin\theta$) of the imaging lens where n is the refractive index of the surrounding medium and θ the angle of the highest wave vector that is accessible. It is shown in Fig. 1.1 that a plane wave is focused using an optical lens. In the focal plane of a lens with cylindrical symmetry, the intensity is given by an Airy disk function which is

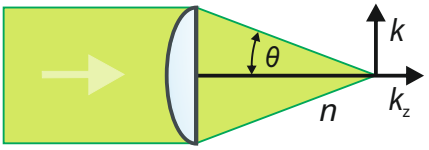

Figure 1.1: Focusing of a light beam with an optical lens. An optical lens generates a focal spot from a plane wave in the focal plane. θ is the maximum angle that is refracted by the lens, n the refractive index of the surrounding medium, k the radial component of the wave vector, and k_z the longitudinal component of the wave vector of light.

$$I(r) = I_0 \left[k_{\max}^2 \frac{J_1(k_{\max} r)}{k_{\max} r} \right]^2 , \tag{1.1}$$

where I_0 is a prefactor, r the position in cylindrical coordinates, $k_{\max}$ the maximum wave vector in the radial direction, J_1 a Bessel function of the first kind. In essence, the Airy disk function is the impuls response of the system and is called the incoherent point spread function (PSF).

It is necessary to define a figure of merit for quantitative analysis of the diffraction-limited resolution of optical imaging systems. There are three different

resolution criteria that are used for resolution that are given in Fig. 1.2; Abbe's resolution limit, Sparrow's resolution limit, and Rayleigh's resolution limit. Here, we give the definition of resolution only for incoherent imaging modalities. Abbe's resolution limit is given by

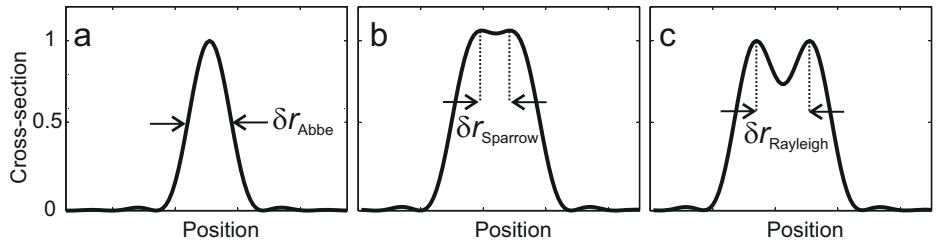

Figure 1.2: The resolution criteria. (a) Abbe's resolution limit, (b) Sparrow's resolution limit, (c) Rayleigh's resolution limit.

$$\delta r_{\text{Abbe}} = \frac{0.5\lambda}{\text{NA}} \tag{1.2}$$

and approximately equal to the full width half maximum of the PSF. Abbe's resolution limit characterizes the PSF of the system and usually is not appropriate for determining resolution of images. It is more suitable to use either Sparrow's or Rayleigh's resolution criteria to determine resolution of an image since they both give information on how the system can resolve two separated point sources. For two Airy disk functions, Sparrow's resolution limit is given by

$$\delta r_{\text{Sparrow}} = \frac{0.47\lambda}{\text{NA}}. \tag{1.3}$$

By definition, Sparrow's resolution criterion is the distance where the minimum between two separated PSFs disappears. Rayleigh's resolution criterion is slightly more strict compared to Sparrow's resolution criterion. According to Rayleigh's resolution criterion, the separation between two Airy disk PSFs must be such that the minimum of the first Airy disk should correspond to the maximum of the second Airy disk and this distance is given by

$$\delta r_{\text{Rayleigh}} = \frac{0.61\lambda}{\text{NA}}. \tag{1.4}$$

Rayleigh's resolution criterion only applies to optical imaging systems which have an Airy disk as PSF.

In this section, we reviewed the criteria that are generally used to predict the diffraction-limited resolution of optical imaging systems. However, for optical systems that are not diffraction-limited the effect of optical aberrations and finite signal-to-noise must be taken into consideration [36–39]. The quest for high-resolution therefore involves not only reduction of the size of the PSF, but also

obtaining sufficient signal-to-noise to resolve the finest details of an object.

1.3 Outline of this thesis

In this thesis, we present new high-resolution imaging methods that are based on light scattering of disordered materials and advanced image reconstruction methods. This thesis is organized as follows:

In **Chapter 2**, we introduce basic concepts of light and optical imaging systems that are widely used for high-resolution optical imaging and are also employed in the further chapters of this thesis.

In **Chapter 3**, we demonstrate a method to find the optimal enhancement in a wavefront shaping experiment in the presence of camera noise, laser intensity noise and shot-noise in the photodetection process. We use a sequential stepwise optimization algorithm to find the optimal phase pattern on the spatial light modulator (SLM). In this algorithm, one row of the transmission matrix of the scattering medium is measured and phase conjugated [27, 40]. In the absence of noise, the perfect phase pattern is obtained in one iteration. To find the optimal phase pattern in the presence of noise, we use a two-step method. First, we run a pre-optimization with coarse pixels, giving a low enhancement. Then, the algorithm is re-run with fine pixelation to obtain a high enhancement. In many cases pre-optimization improves the signal-to-noise ratio up to shot-noise limit. We present a method to choose the correct pre-optimization in order to obtain the maximal signal-to-noise ratio. Our results are equally relevant for other focusing methods such as using the measured optical transmission matrix [29, 41] and optical phase conjugation [42, 43].

In **Chapter 4**, we present a new type of scattering solid immersion lens (SSIL) that is based on gallium phosphide (GaP), of which one surface is rough and one surface is polished and coated with an absorptive anti-reflection silicon (Si) coating. We demonstrate a new method to characterize the high internal angle scattering of high-index substrates and apply our method to characterize our new SSIL. Our new SSIL enables better signal-to-noise ratio compared to previously used porous GaP SSILs. We image the cross-section of a gold nanoparticle using our SSIL and demonstrate a sub-100 nm optical resolution with visible light.

In **Chapter 5**, we report speckle correlation resolution enhancement (SCORE) microscopy which exploits correlations in speckle illumination through a randomly scattering high-index medium. Parallel detection of the speckle pattern provides wide-field imaging beyond the range of the optical memory effect. We obtain a high-resolution and wide-field two-dimensional fluorescence image of dye-doped nanospheres with a diameter of 100 nm. We have developed a new image reconstruction algorithm that converges even for complex object structures. Our method works with general fluorescent dyes and we demonstrate a deconvolved resolution of 116 nm with a field of view of 10 µm × 10 µm.

In **Chapter 6**, we demonstrate a new high-resolution, high-contrast fluorescence imaging method that is based on periodic pattern illumination through a GaP SSIL. Our method enables direct access to Fourier components of a fluores-

cent object through a scattering layer and does not require a computer algorithm to retrieve an additional information for a high-resolution image reconstruction. This method has potentially higher resolution compared to the method of SCORE that is presented in chapter 5.

In **Chapter 7**, we provide a summary and outlook of the thesis.

Bibliography

[1] H. C. van de Hulst, *Light scattering by small particles* (Dover Publications, Inc. New York, 1981). — p.9.

[2] E. Hecht, *Optics* (Addison Wesley Longman, Inc., 1998). — p.9.

[3] L. Novotny and B. Hecht, *Principles of nano-optics* (Cambridge Univ. Press, Cambridge, U.K., 2006). — p.9, 67, 81.

[4] J. Bertolotti, *Light transport beyond diffusion*, Ph.D. thesis, University of Florence, 2008. — p.9.

[5] S. Faez, *Universal wave phenomena in multiple scattering media*, Ph.D. thesis, University of Amsterdam, 2011. — p.9.

[6] N. Zheludev, *What diffraction limit?*, Nat. Mater. **7**, 420 (2008). — p.9.

[7] S. Manohar, S. E. Vaartjes, J. C. G. van Hespen, J. M. Klaase, F. M. van den Engh, W. Steenbergen, and T. G. Van Leeuwen, *Initial results of in vivo non-invasive cancer imaging in the human breast using near-infrared photoacoustics*, Opt. Express **15**, 12277 (2007). — p.9.

[8] J. J. Bozzola and L. D. Russell, *Electron microscopy: Principles and techniques for biologists* (Jones & Bartlett Learning, 1999). — p.9.

[9] W. Coene, G. Janssen, M. O. de Beeck, and D. Van Dyck, *Phase retrieval through focus variation for ultra-resolution in field-emission transmission electron microscopy*, Phys. Rev. Lett. **69**, 3743 (1992). — p.9.

[10] V. E. Cosslett and W. C. Nixon, *X-Ray microscopy* (Cambridge University Press, Cambridge, 2014). — p.9.

[11] E. Betzig, A. Lewis, A. Harootunian, M. Isaacson, and E. Kratschmer, *Near field scanning optical microscopy (NSOM): Development and biophysical applications*, Biophys. J. **49**, 269 (1986). — p.9, 19, 67.

[12] J. A. Porto, R. Carminati, and J.-J. Greffet, *Theory of electromagnetic field imaging and spectroscopy in scanning near-field optical microscopy*, J. Appl. Phys. **88**, 4845 (2000). — p.9.

[13] G. Binnig, C. F. Quate, and C. Gerber, *Atomic force microscope*, Phys. Rev. Lett. **56**, 930 (1986). — p.9.

[14] P. Davidovits and D. Egger, *Scanning laser microscope*, Nature **223**, 831 (1969). — p.9.

[15] S. M. Mansfield and G. S. Kino, *Solid immersion microscope*, Appl. Phys. Lett. **57**, 2615 (1990). — p.9, 51, 105, 111.

[16] S. W. Hell and J. Wichmann, *Breaking the diffraction resolution limit by stimulated emission: Stimulated-emission-depletion fluorescence microscopy*, Opt. Lett. **19**, 780 (1994). — p.9, 19, 67, 91, 107.

[17] X. Chen and S. R. J. Brueck, *Imaging interferometric lithography: Approaching the resolution limits of optics*, Opt. Lett. **24**, 124 (1999). — p.9, 25.

[18] R. Heintzmann and C. Cremer, *Lateral modulated excitation microscopy: Improvement of resolution by using a diffraction grating*, Proc. SPIE **3568**, 185 (1999). — p.9, 19, 67, 68, 91.

[19] M. G. L. Gustafsson, *Surpassing the lateral resolution limit by a factor of two using structured illumination microscopy*, J. Microsc. **198**, 82 (2000). — p.9, 19, 25, 67, 68, 91.

[20] E. Betzig, G. H. Patterson, R. Sougrat, O. W. Lindwasser, S. Olenych, J. S. Bonifacino, M. W. Davidson, J. Lippincott-Schwartz, and H. F. Hess, *Imaging intracellular fluorescent proteins at nanometer resolution*, Science **313**, 1642 (2006). — p.9, 19, 67, 91.

[21] M. J. Rust, M. Bates, and X. Zhuang, *Sub-diffraction-limit imaging by stochastic optical reconstruction microscopy (STORM)*, Nat. Methods **3**, 793 (2006). — p.9, 19, 67, 91.

[22] S. W. Hell, *Far-field optical nanoscopy*, Science **316**, 1153 (2007). — p.9, 19, 67, 91, 107.

[23] T. Dertinger, R. Colyer, G. Iyer, S. Weiss, and J. Enderlein, *Fast, background-free, 3D super-resolution optical fluctuation imaging (SOFI)*, Proc. Natl. Acad. Sci. U.S.A. **106**, 22287 (2009). — p.9, 19, 67, 91.

[24] J. M. Beckers, *Adaptive optics for astronomy - principles, performance, and applications*, Annual review of astronomy and astrophysics **31**, 13 (1993). — p.10.

[25] R. K. Tyson, *Principles of Adaptive Optics* (Academic, 1998). — p.10.

[26] C. Maurer, A. Jesacher, S. Bernet, and M. Ritsch-Marte, *What spatial light modulators can do for optical microscopy*, Laser & Photonics Reviews **5**, 81 (2011). — p.10.

[27] I. M. Vellekoop and A. P. Mosk, *Focusing coherent light through opaque strongly scattering media*, Opt. Lett. **32**, 2309 (2007). — p.10, 12, 27, 60.

[28] A. P. Mosk, A. Lagendijk, G. Lerosey, and M. Fink, *Controlling waves in space and time for imaging and focusing in complex media*, Nature Photon. **6**, 283 (2012). — p.10, 37, 58, 60.

[29] S. M. Popoff, G. Lerosey, R. Carminati, M. Fink, A. C. Boccara, and S. Gigan, *Measuring the transmission matrix in optics: An approach to the study and control of light propagation in disordered media*, Phys. Rev. Lett. **104**, 100601 (2010). — p.10, 12.

[30] E. G. van Putten and A. P. Mosk, *The information age in optics: Measuring the transmission matrix*, Physics **3**, 22 (2010). — p.10.

[31] S. Popoff, G. Lerosey, M. Fink, A. C. Boccara, and S. Gigan, *Image transmission through an opaque material*, Nat. Commun. **1**, (2010). — p.10, 27, 76.

[32] Y. Choi, T. D. Yang, C. Fang-Yen, P. Kang, K. J. Lee, R. R. Dasari, M. S. Feld, and W. Choi, *Overcoming the diffraction limit using multiple light scattering in a highly disordered medium*, Phys. Rev. Lett. **107**, 023902 (2011). — p.10, 27, 76.

[33] Y. Choi, M. Kim, C. Yoon, T. D. Yang, K. J. Lee, and W. Choi, *Synthetic aperture microscopy for high resolution imaging through a turbid medium*, Opt. Lett. **36**, 4263 (2011). — p.10, 27.

[34] E. Abbe, *Beiträge zur theorie des mikroskops und der mikroskopischen wahrnehmung*, Archiv für Mikroskopische Anatomie **9**, 413 (1873). — p.10, 19.

[35] C. W. McCutchen, *Superresolution in microscopy and the Abbe resolution limit*, J. Opt. Soc. Am. **57**, 1190 (1967). — p.10.

[36] I. J. Cox and C. J. R. Sheppard, *Information capacity and resolution in an optical system*, J. Opt. Soc. Am. A **3**, 1152 (1986). — p.10, 11, 21.

[37] M. A. Neifeld, *Information, resolution, and space-bandwidth product*, Opt. Lett. **23**, 1477 (1998). — p.10, 11, 82.

[38] E. Stelzer, *Contrast, resolution, pixelation, dynamic range and signal-to-noise ratio: Fundamental limits to resolution in fluorescence light microscopy*, J. Microsc. **189**, 15 (1998). — p.10, 11.

[39] J. W. Goodman, *Introduction to Fourier Optics* (Roberts & Company, Englewood, 2005). — p.10, 11, 19, 21, 71, 80.

[40] I. M. Vellekoop and A. P. Mosk, *Phase control algorithms for focusing light through turbid media*, Opt. Comm. **281**, 3071 (2008). — p.12.

[41] D. Akbulut, *Measurements of strong correlations in the transport of light through strongly scattering materials*, Ph.D. thesis, University of Twente, 2013. — p.12, 106.

[42] Z. Yaqoob, D. Psaltis, M. S. Feld, and C. Yang, *Optical phase conjugation for turbidity suppression in biological samples*, Nature Photon. **2**, 110 (2008). — p.12.

[43] C.-L. Hsieh, Y. Pu, R. Grange, and D. Psaltis, *Digital phase conjugation of second harmonic radiation emitted by nanoparticles in turbid media*, Opt. Express **18**, 12283 (2010). — p.12.

CHAPTER 2

Spatially controlled light for high-resolution optical imaging

2.1 Introduction

Optical imaging with a high spatial resolution is necessary to study morphology and function of structures at nanoscale. The resolution of standard optical imaging is limited due to diffraction as noted by Abbe [1]. Several methods have been developed to obtain an optical resolution beyond Abbe's resolution limit [2–10]. Structured illumination microscopy (SIM) stands out because of its wide field of view, applicability to any object that fluoresces, and its speed compared to nonlinear optical microscopy methods [11]. SIM is based on illumination of the sample with periodically patterned light. The information of several images taken with different periodically patterned light is combined to enhance the resolution of the wide-field image of a conventional optical microscope. Typically, SIM enables a resolution that is two times greater compared to a conventional optical microscope [11]. There have been several approaches such as using a nonlinear photoresponse [5] or periodically patterned surface plasmon polariton waves for illumination [12–18] to improve the resolution of SIM further. Recently, SIM has been generalized for non-periodic pattern illumination [19, 20].

In this chapter, we review the essential concepts of resolution in optical imaging systems. The concepts are then used in chapters 5 and 6. This is then applied to analyze resolution enhancement strategies in optical imaging that are based on the exploitation of spatially controlled illumination. In this chapter we follow conventions and notations from the literature on structured illumination microscopy and especially *Introduction to Fourier Optics* by J. W. Goodman [21]. In section 2, we introduce the concept of degree of coherence and its relevance in optical imaging. In section 3, we describe transfer functions that are used for coherent and incoherent imaging modalities. In sections 4 and 5, we review the methods for resolution enhancement that are based on periodic and non-periodic pattern illumination. In the last section of this chapter, we summarize the discussions.

2.2 Coherence in optical imaging

Optical imaging deals with measurement or reconstruction of the scattered light intensity by a physical object. The statistics of the time behavior of the phases of the scattered light field influences the observed time-averaged scattered light intensity. The field correlation between two points P_1 and P_2 of the object in case when the polarization of light is neglected is given by the degree of coherence [22] as

$$\gamma_{12}(\tau) = \frac{\left|\int \mathbf{E_1}(t) \cdot \mathbf{E_2}^*(t-\tau)\mathrm{d}t\right|}{\sqrt{\int |\mathbf{E_1}(t)|^2 \,\mathrm{d}t \int |\mathbf{E_2}(t)|^2 \,\mathrm{d}t}} \tag{2.1}$$

where $\mathbf{E_1}(t)$ is the scattered light field by P_1 at time t, $\mathbf{E_2}^*(t-\tau)$ the complex conjugate of the scattered light field by P_2 at time $t-\tau$. In essence, equation 2.1 gives spatial coherence for $P_1 \neq P_2$ and $\tau = 0$, and temporal coherence for $P_1 = P_2$. The degree of coherence quantifies how the diffracted light field of an extended incoherent light source (or an object) is correlated in far-field. In general one deals with light sources with limited temporal and spatial coherence, therefore partially coherent light sources. In advanced optical imaging methods such as phase contrast microscopy [23–27], optical coherence tomography [28], or interferometric synthetic aperture microscopy [29], the behavior of partially coherent light has to be taken into consideration [22]. For several optical imaging methods, it is sufficient to assume the light field is either completely coherent ($\gamma_{12} = 1$) or completely incoherent ($\gamma_{12} = 0$). Coherent and incoherent imaging are fundamentally very different. Young's double slit experiment is a useful

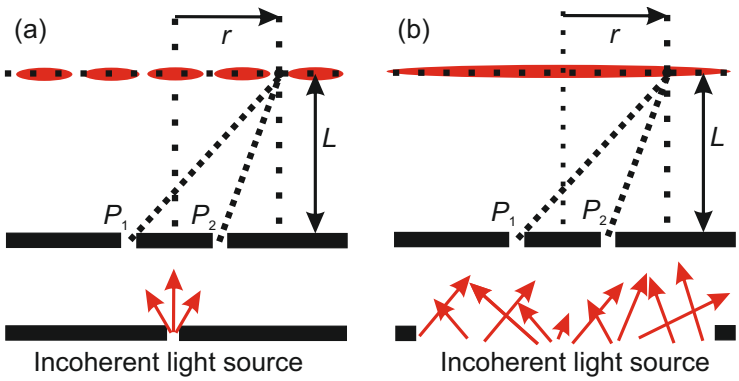

Figure 2.1: Young's double slit experiment (a) for a point light source, (b) for an extended light source. A fringe pattern is observed in far-field of the screen for a point light source. For an extended light source, the fringe pattern disappears.

example to illustrate the difference of two cases. Suppose we have an object that is made of two slits P_1 and P_2 in two different positions on a screen as

shown in Fig. 2.1a. We illuminate the slits with an incoherent point light source. We detect the transmitted light intensity with a point detector at a distance L behind the screen. The transverse position of the point detector with respect to the center of the slits is given by r. Assuming the response time of our detector is much slower than the optical frequencies and the coherence times, we will detect the time-averaged intensity $\langle I \rangle$ that is given by

$$\langle I \rangle = (E_1 + E_2)^2 = E_1^2 + E_2^2 + 2E_1E_2 \langle \cos\Delta\phi \rangle , \tag{2.2}$$

where E_1 is the amplitude of the scattered light from P_1, E_2 the amplitude of the scattered light from P_2, and $\Delta\phi$ the phase difference between the two scattered light fields. In the case that the size of the illuminating light source is extended to a very large area (Fig. 2.1b), $\langle \cos\Delta\phi \rangle$ term vanishes, therefore the detected time-averaged intensity simplifies to

$$\langle I \rangle = (E_1 + E_2)^2 = E_1^2 + E_2^2. \tag{2.3}$$

Angular extension of light illumination in an optical imaging system is always limited, therefore a typical optical imaging system enables either partially coherent or coherent imaging and can never enable fully incoherent imaging unless there is an incoherent process such as fluorescence is involved [30]. Therefore equation 2.3 is only strictly valid for optical imaging modalities with an incoherent process such as fluorescence.

2.3 Transfer functions for coherent and incoherent imaging

We can assume an optical imaging system as a black box that has a certain response function to the object's spatial frequency components [21]. The frequency response of an optical imaging system is given by its transfer function. It is essential to consider the coherence of the light and the object to employ the correct transfer function. Coherent optical imaging is linear in complex amplitude. In coherent optical imaging, the complex amplitude image $B(x, y)$ of a complex amplitude object $A(x, y)$ is given by

$$B(x, y) = \iint h(x - \delta x, y - \delta y) A(\delta x, \delta y) \mathrm{d}\delta x \mathrm{d}\delta y \tag{2.4}$$

where h is the complex amplitude point spread function of the imaging system, and the intensity image $I(x, y)$ is given by

$$I(x, y) = |B(x, y)|^2 . \tag{2.5}$$

The spatial Fourier transforms of $A(x, y)$ and $B(x, y)$ are given by

$$\widetilde{A}(k_{\mathrm{x}}, k_{\mathrm{y}}) = \iint A(x, y)\mathrm{e}^{-\mathrm{i}2\pi(k_{\mathrm{x}}x+k_{\mathrm{y}}y)}\mathrm{d}x\mathrm{d}y, \tag{2.6}$$

$$\widetilde{B}(k_{\mathrm{x}}, k_{\mathrm{y}}) = \iint B(x, y)\mathrm{e}^{-\mathrm{i}2\pi(k_{\mathrm{x}}x+k_{\mathrm{y}}y)}\mathrm{d}x\mathrm{d}y \tag{2.7}$$

respectively. The frequency response of the imaging system to the complex amplitude point spread function $h(x, y)$ is the complex amplitude transfer function (ATF $= \tilde{h}(k_{\mathrm{x}}, k_{\mathrm{y}})$) and given by

$$\tilde{h}(k_{\mathrm{x}}, k_{\mathrm{y}}) = \iint h(x, y)\mathrm{e}^{-\mathrm{i}2\pi(k_{\mathrm{x}}x+k_{\mathrm{y}}y)}\mathrm{d}x\mathrm{d}y. \tag{2.8}$$

By applying the convolution theorem to equation 2.4, the complex amplitude spectrum $\widetilde{A}$ of the object can be mapped to the complex amplitude spectrum $\widetilde{B}$ of the image linearly with the complex amplitude transfer function as

$$\widetilde{B}(k_{\mathrm{x}}, k_{\mathrm{y}}) = \tilde{h}(k_{\mathrm{x}}, k_{\mathrm{y}})\widetilde{A}(k_{\mathrm{x}}, k_{\mathrm{y}}) \tag{2.9}$$

and the Fourier transform of the intensity image $I(x, y)$ is found to be

$$F(k_{\mathrm{x}}, k_{\mathrm{y}}) = \widetilde{B}(k_{\mathrm{x}}, k_{\mathrm{y}}) \star \widetilde{B}(k_{\mathrm{x}}, k_{\mathrm{y}}) \tag{2.10}$$

where $\star$ denotes autocorrelation. Here it is evident that an optical imaging system behaves as a band-pass filter. For an optical imaging system with circularly symmetric transfer function, the highest spatial frequency $k_{\max}$ determines the resolution of the optical imaging system and given by

$$k_{\max} = \frac{2\pi\mathrm{NA}}{\lambda} \tag{2.11}$$

where NA is the numerical aperture of the imaging system, and λ the wavelength of the light.

In incoherent imaging such as in fluorescence imaging, the object responds to the intensity linearly. Therefore the intensity image $I(x, y)$ is related to intensity object $O(x, y)$ via the convolution integral

$$I(x, y) = \iint \left|h(x - \delta x, y - \delta y)\right|^2 O(\delta x, \delta y)\mathrm{d}\delta x\mathrm{d}\delta y. \tag{2.12}$$

The normalized spatial frequency components of $I(x, y)$ and $O(x, y)$ with respect to their zero spatial frequencies are given by

$$F(k_{\mathrm{x}}, k_{\mathrm{y}}) = \frac{\iint I(x, y)\mathrm{e}^{-\mathrm{i}2\pi(k_{\mathrm{x}}x+k_{\mathrm{y}}y)}\mathrm{d}x\mathrm{d}y}{\iint I(x, y)\mathrm{d}x\mathrm{d}y}, \tag{2.13}$$

$$\widetilde{O}(k_{\mathrm{x}}, k_{\mathrm{y}}) = \frac{\iint O(x, y)\mathrm{e}^{-\mathrm{i}2\pi(k_{\mathrm{x}}x+k_{\mathrm{y}}y)}\mathrm{d}x\mathrm{d}y}{\iint O(x, y)\mathrm{d}x\mathrm{d}y} \tag{2.14}$$

respectively. For the frequency components of a positive and real function such as $I(x, y)$ and $O(x, y)$, the maximum is always at zero frequency, therefore these functions are usually normalized with respect to their values at zero frequency. Similarly, the normalized transfer function for incoherent optical imaging is represented by

$$\widetilde{H}(k_{\mathrm{x}}, k_{\mathrm{y}}) = \frac{\iint |h(x,y)|^2 \, \mathrm{e}^{-\mathrm{i}2\pi(k_{\mathrm{x}}x + k_{\mathrm{y}}y)} \mathrm{d}x\mathrm{d}y}{\iint |h(x,y)|^2 \, \mathrm{d}x\mathrm{d}y}. \tag{2.15}$$

The transfer function for incoherent optical imaging $\widetilde{H}(k_x, k_y)$ is called optical transfer function (OTF). The convolution theorem leads to the linear relation between $F(k_{\mathrm{x}}, k_{\mathrm{y}})$ and $\widetilde{O}(k_{\mathrm{x}}, k_{\mathrm{y}})$ via OTF as

$$F(k_{\mathrm{x}}, k_{\mathrm{y}}) = \widetilde{H}(k_{\mathrm{x}}, k_{\mathrm{y}}) \widetilde{O}(k_{\mathrm{x}}, k_{\mathrm{y}}). \tag{2.16}$$

Similar to coherent imaging case, the highest spatial frequency k_{max} determines the resolution of the optical imaging system, which is given by equation 2.11 for an optical imaging system with a circularly symmetric transfer function.

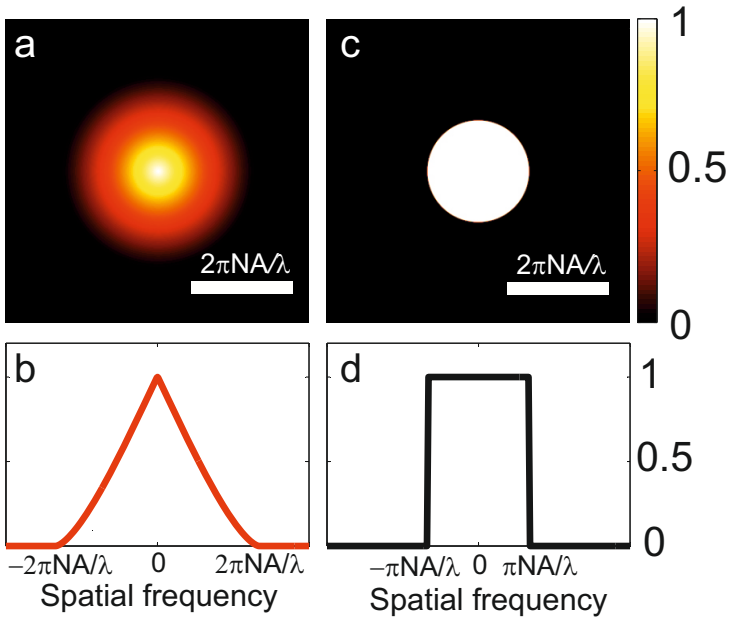

Figure 2.2: The transfer functions for a diffraction-limited optical imaging system. (a) The optical transfer function (OTF) used for incoherent imaging and (b) its cross-section. (c) The amplitude transfer function (ATF) used for coherent imaging and (d) its cross-section. It is noteworthy that cut-off frequency of ATF is for field modulation and the cut-off frequency of OTF is for intensity modulation.

It is clear in equations 2.8 and 2.15 that both ATF and OTF are related to the complex point spread function $h(x, y)$. This relation leads to the one of the most important relation in Fourier optics which is

$$OTF(\Delta k_{\mathrm{x}}, \Delta k_{\mathrm{y}}) = \frac{[ATF \star ATF^{*}]\,(\Delta k_{\mathrm{x}}, \Delta k_{\mathrm{y}})}{\iint |ATF(k_{\mathrm{x}}, k_{\mathrm{y}})|^{2}\,\mathrm{d}k_{\mathrm{x}}\mathrm{d}k_{\mathrm{y}}}. \tag{2.17}$$

This autocorrelation relation leads to a difference in the sensitivity of the resolution of the system to noise between coherent and incoherent imaging modalities. Generally, images of an incoherent imaging modality have lower contrast compared to coherent imaging modality because of the peak at the zero frequency of the OTF. In an optical imaging system with a finite dynamic range and signal-to-noise, higher spatial frequencies of an incoherent object are suppressed by the OTF and may disappear in the noise. In Fig. 2.2 OTF and ATF of a diffraction-limited optical imaging system are shown. Figs. 2.2a,b are the OTF and the cross-section of the OTF and Figs. 2.2c,d the corresponding ATF and the cross-section of the ATF of the same imaging system. It is evident that the high spatial frequencies of an incoherent object are more likely to be affected by noise compared to the low spatial frequencies, due to the low value of the OTF at high spatial frequencies. However, the effect of the ATF on the signal-to-noise is equal for all spatial frequency components of a coherent object with a coherent illumination such as in reference [31].

2.4 Periodic structured illumination

Structured illumination microscopy (SIM) enables resolution enhancement of incoherent imaging approximately up to two times higher resolution compared to Abbe's resolution limit [4, 11]. With a similar approach the resolution can be improved also for coherent imaging with full-field holographic detection [32–35] or Fourier ptychography [36]. SIM is based on illuminating a fluorescent object with a series of periodic intensity patterns with a few translations and rotations. For each illumination, wide-field fluorescence images are recorded and a high-resolution, wide-field image is reconstructed.

The reconstruction procedure in SIM is straightforward. The multiplication operation between the object and the periodic illumination pattern in the object domain is a convolution operation in the Fourier domain. In the Fourier domain, the measured fluorescence image using a periodic illumination pattern with a spatial frequency k_{ill} is given by

$$F_{\Delta\phi}(k) = I_0 \left(F(k) + 0.5 \left(F(k + k_{\mathrm{ill}}) \mathrm{e}^{\mathrm{i}(\Delta\phi + \delta\phi)} + F(k - k_{\mathrm{ill}}) \mathrm{e}^{-\mathrm{i}(\Delta\phi + \delta\phi)} \right) \right) \tag{2.18}$$

where I_0 is a prefactor, $\Delta\phi$ the phase difference of the two beams that generate the periodic illumination pattern, $\delta\phi$ the phase offset of the periodic illumination pattern which is typically $\delta\phi = 0$ for SIM, $F(k)$ the spatial Fourier transform of the object; $F(k + k_{\mathrm{ill}})$ and $F(k - k_{\mathrm{ill}})$ are the shifted high-frequency Fourier components of the object. Three measurements with $\Delta\phi = 0, 2\pi/3, 4\pi/3$ are taken, which corresponds to translations of the periodic illumination pattern. The spatial Fourier components $F(k)$, $F(k + k_{\mathrm{ill}})$, and $F(k - k_{\mathrm{ill}})$ are extracted using the relation

$$\begin{bmatrix} F(k) \\ F(k + k_{\mathrm{ill}}) \\ F(k - k_{\mathrm{ill}}) \end{bmatrix} = \begin{bmatrix} 1 & 0.5 & 0.5 \\ 1 & 0.5\mathrm{e}^{\mathrm{i}2\pi/3} & 0.5\mathrm{e}^{-\mathrm{i}2\pi/3} \\ 1 & 0.5\mathrm{e}^{\mathrm{i}4\pi/3} & 0.5\mathrm{e}^{-\mathrm{i}4\pi/3} \end{bmatrix}^{-1} \begin{bmatrix} F_0(k) \\ F_{2\pi/3}(k) \\ F_{4\pi/3}(k) \end{bmatrix}. \tag{2.19}$$

Finally, $F(k + k_{\mathrm{ill}})$ and $F(k - k_{\mathrm{ill}})$ are shifted in the opposite directions in the Fourier domain by a factor of k_{ill}. This procedure enhances the resolution on one axis. The same procedure is repeated for at least two more axes to obtain a resolution enhancement in two-dimensions. The resolution of SIM is given by

$$\delta r = \frac{\pi}{k_{\mathrm{ill}} + k_{\mathrm{det}}} \tag{2.20}$$

where the spatial frequency of the illumination pattern is $k_{\mathrm{ill}} = 2\pi \mathrm{NA}_{\mathrm{ill}}/\lambda_{\mathrm{ill}}$, $\mathrm{NA}_{\mathrm{ill}}$ is the numerical aperture of the illumination optics, λ_{ill} the wavelength of the illumination beam, $k_{\mathrm{det}} = 2\pi \mathrm{NA}_{\mathrm{det}}/\lambda_{\mathrm{flu}}$ the highest spatial frequency in the detection, $\mathrm{NA}_{\mathrm{det}}$ the numerical aperture of the detection optics, and λ_{flu} the center wavelength of the fluorescence light.

The reconstruction procedure is shown in Fig. 2.3. For clarity the optical transfer function (OTF) of the detection optics is depicted narrower than the

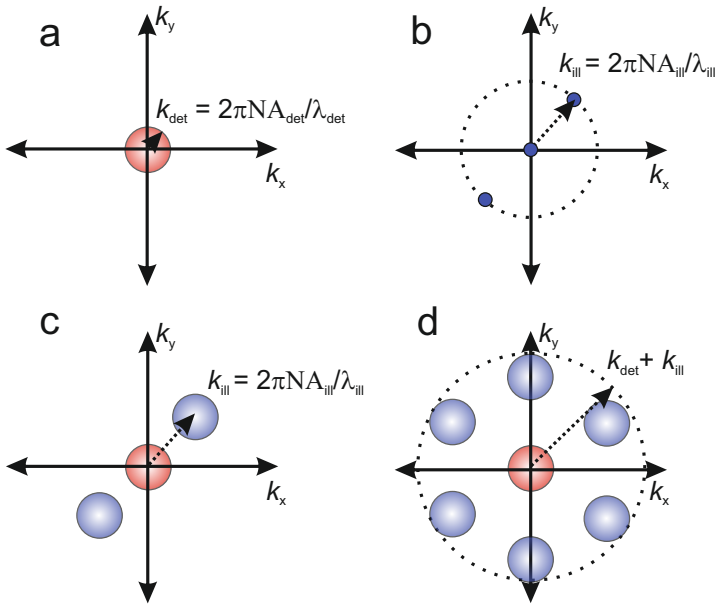

Figure 2.3: The cartoon shows the high-resolution image reconstruction of SIM data in the Fourier domain. (a) The optical transfer function (OTF) of the detection optics. (b) The Fourier transform of the illumination pattern. (c) Shifting the high-resolution information to the correct position in the Fourier domain. (d) Repeating the procedure with illumination patterns in other axes in the Fourier domain.

spatial frequency of the illumination. Typically they are equal so that the circles overlap. The fluorescent object is low-pass filtered at k_{det} in the Fourier domain by the OTF of the detection optics (Fig. 2.3a). The illumination pattern contains spatial frequency components, represented by three delta functions, one at the center, the other two positioned at a distance of k_{ill} to the center (Fig. 2.3b). The superimposed high-k information is extracted and shifted to the correct position in the Fourier domain (Fig. 2.3c). The procedure is repeated for other axes in the Fourier domain to obtain resolution enhancement for a two-dimensional image.

2.5 Non-periodic structured illumination: Speckle pattern illumination

When monochromatic light beam impinges on a scattering medium, the transmitted light forms a speckle pattern with randomly distributed bright and dark regions. There are two main imaging approaches that are based on speckle pattern illumination: Restructuring the speckle pattern using wavefront shaping [37], or using the speckle pattern itself. Speckle patterns can be modified and a bright focus can be generated through the scattering medium by wavefront shaping [37, 38]. Wavefront shaping has opened a new window in imaging science and already several new imaging methods are demonstrated that are based on wavefront shaping [39–45]. However, wavefront shaping based approaches require an access to the object or a guide star for a feedback signal and an extra calibration time to characterize the scattering medium. Another approach is directly using speckle pattern illumination for imaging [19, 20, 46–55].

In this section, we describe speckle scanning microscopy, that is based on fluorescence imaging using single speckle pattern illumination. Speckle scanning microscopy has been employed in various imaging scenarios such as high-resolution imaging [20, 46, 55] and imaging hidden objects by a scattering medium [50–53]. In speckle scanning microscopy, the speckle pattern is translated on the object using a speckle correlation effect known as the optical memory effect [43, 56–58] and total intensity of the object is recorded for each speckle pattern position. In some studies the object is translated instead of the speckle pattern which is mathematically identical [20, 46].

In Fig. 2.4 the geometry of the optical memory effect based speckle scanning microscopy is shown. A laser light beam is incident on a scattering medium. The scattering medium generates a speckle pattern on the fluorescent object behind itself. A tilt of $\Delta\theta_{\mathrm{x}}$ and $\Delta\theta_{\mathrm{y}}$ of the incident laser beam results in perpendicular speckle pattern displacements $\Delta x \approx \Delta\theta_{\mathrm{x}} L$ and $\Delta y \approx \Delta\theta_{\mathrm{y}} L$ on the object, where L is the distance of the object to the medium. The speckle pattern does not change significantly as long as the tilt is $\Delta\theta < \lambda/2\pi d$ (λ is the wavelength of light and d the thickness of the scattering medium). For an arbitrary position of the detector, the total fluorescence can be recorded for each speckle pattern position.

In a speckle scanning microscopy experiment, the measured total intensity as

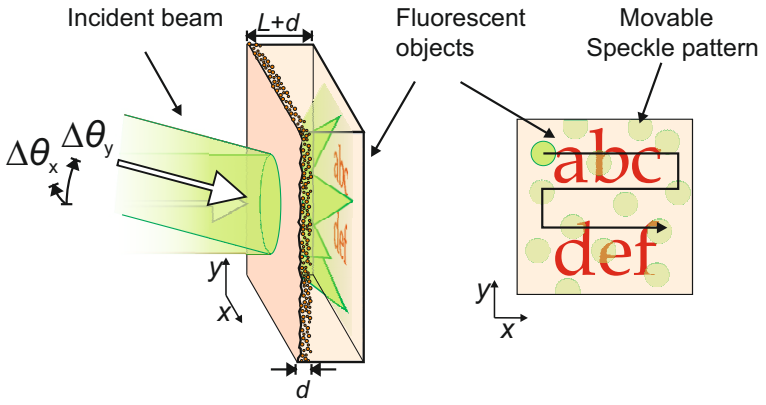

Figure 2.4: The geometry of the optical memory effect based speckle scanning microscopy. A beam of laser light illuminates a scattering medium with a thickness of d. A speckle pattern is formed on the objects which are at a distance L behind the medium. The inset shows a detail of the object plane on which fluorescent objects represented with six letters of the Latin alphabet are placed. By tilting the incident beam over an angle, the speckle pattern is scanned across the objects. This figure is adapted from reference [59].

a function of shift Δx and Δy of the speckle pattern $S(x, y)$ is given by

$$I(\Delta x, \Delta y) = \iint S(x - \Delta x, y - \Delta y) O(x, y) \mathrm{d}x\mathrm{d}y \tag{2.21}$$

$$= [O(x, y) * S(-x, -y)](\Delta x, \Delta y) \tag{2.22}$$

where $*$ denotes a convolution product and $O(x, y)$ the fluorescent object. The image of $O(x, y)$ can be retrieved by deconvolving $I(\Delta x, \Delta y)$ with the known speckle pattern $S(x, y)$ [46]. There is a recent approach where the image can be retrieved without any knowledge of $S(x, y)$ [50, 59]. Using the associative property of the convolution the autocorrelation $[I \star I](\delta x, \delta y)$ is equal to

$$\begin{aligned}
[I \star I](\delta x, \delta y) &= [(O * S(-x, -y)) \star (O * S(-x, -y))](\delta x, \delta y) \\
&= [(O \star O) * (S(-x, -y) \star S(-x, -y))](\delta x, \delta y) \\
&= [(O \star O) * (S \star S)](\delta x, \delta y),
\end{aligned} \tag{2.23}$$

where we use the fact that S is always real because we consider the speckle pattern intensity. In Fig. 2.5a a speckle pattern that is captured by a CCD camera and in Fig. 2.5b its autocorrelation is shown. The autocorrelation of the speckle pattern $(S \star S)$ has a sharp peak with an average speckle grain size [60, 61] which results in

$$[I \star I](\delta x, \delta y) \approx [O \star O](\delta x, \delta y). \tag{2.24}$$

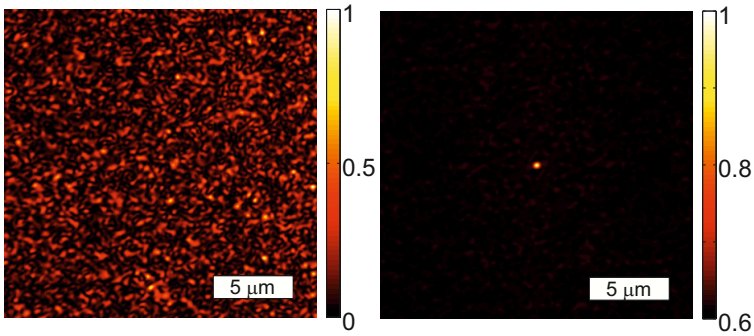

Figure 2.5: The intensity point spread function (PSF) of speckle scanning microscopy. (a) A CCD camera image of a speckle pattern that is generated by shining a coherent laser beam on a scattering medium. The speckle pattern is imaged behind the scattering medium on a CCD camera. (b) The autocorrelation of the speckle pattern is a sharp peak at the center on top of a background. The size of the peak is equal to the average speckle grain size. The autocorrelation of the speckle pattern is the intensity point spread function (PSF) in a speckle scanning microscopy experiment.

By applying convolution theorem to equation 2.24 we obtain

$$\mathcal{F}\{O \star O\} = \mathcal{F}\{O\}\,\mathcal{F}\{O\}^* = |\mathcal{F}\{O\}|^2 \tag{2.25}$$

where $\mathcal{F}\{\}$ denotes a Fourier transform. It is seen that the magnitude of the Fourier components of the object is retained in a speckle scanning microscopy experiment. However, the phases of the Fourier components of the object are lost due to random nature of the speckle pattern. The phase information of the Fourier components of the object can be retrieved by an iterative phase retrieval algorithm [62–65] which enables reconstruction of a high-resolution image of the object under the assumptions that the object size is smaller than the optical memory effect range, the object can be represented by real and positive numbers and there is sufficient signal-to-noise. The resolution is given by the average speckle grain size [50, 55, 59].

Speckle scanning microscopy can be used for scenarios where the spatial information of an object cannot be imaged completely or partially using direct optical methods. Unknown speckle pattern illumination enables extraction of spatial information of objects that cannot be seen directly. Speckle scanning microscopy can provide spatial information of an object when the object is hidden behind or around a corner of a scattering medium [50–53]. In chapter 5, we demonstrate that speckle scanning microscopy also enables high-resolution imaging of objects when there is direct optical access only to low spatial frequency information of the object [55].

We have discussed speckle scanning microscopy using only total intensity measurements of the object response. With a spatially resolved measurement of the

object response, the resolution of speckle scanning microscopy can be enhanced beyond Abbe's resolution limit as in the reference [20].

2.6 Summary

In this chapter we discussed the concept of coherence and its effect on optical imaging that is based on spatially shaped illumination patterns. We described the transfer functions that are used for incoherent and coherent imaging modalities. We briefly explain the procedure of structured illumination microscopy with periodic pattern illumination and speckle pattern illumination. We showed that with spatial control over the wavefront it is possible to obtain images with finer resolution than Abbe's resolution limit.

Bibliography

[1] E. Abbe, *Beiträge zur theorie des mikroskops und der mikroskopischen wahrnehmung*, Archiv für Mikroskopische Anatomie **9**, 413 (1873). — p.10, 19.

[2] E. Betzig, A. Lewis, A. Harootunian, M. Isaacson, and E. Kratschmer, *Near field scanning optical microscopy (NSOM): Development and biophysical applications*, Biophys. J. **49**, 269 (1986). — p.9, 19, 67.

[3] R. Heintzmann and C. Cremer, *Lateral modulated excitation microscopy: Improvement of resolution by using a diffraction grating*, Proc. SPIE **3568**, 185 (1999). — p.9, 19, 67, 68, 91.

[4] M. G. L. Gustafsson, *Surpassing the lateral resolution limit by a factor of two using structured illumination microscopy*, J. Microsc. **198**, 82 (2000). — p.9, 19, 25, 67, 68, 91.

[5] M. G. L. Gustafsson, *Nonlinear structured-illumination microscopy: Wide-field fluorescence imaging with theoretically unlimited resolution*, Proc. Natl. Acad. Sci. U.S.A. **102**, 13081 (2005). — p.19, 67, 92.

[6] S. W. Hell and J. Wichmann, *Breaking the diffraction resolution limit by stimulated emission: Stimulated-emission-depletion fluorescence microscopy*, Opt. Lett. **19**, 780 (1994). — p.9, 19, 67, 91, 107.

[7] S. W. Hell, *Far-field optical nanoscopy*, Science **316**, 1153 (2007). — p.9, 19, 67, 91, 107.

[8] M. J. Rust, M. Bates, and X. Zhuang, *Sub-diffraction-limit imaging by stochastic optical reconstruction microscopy (STORM)*, Nat. Methods **3**, 793 (2006). — p.9, 19, 67, 91.

[9] E. Betzig, G. H. Patterson, R. Sougrat, O. W. Lindwasser, S. Olenych, J. S. Bonifacino, M. W. Davidson, J. Lippincott-Schwartz, and H. F. Hess, *Imaging intracellular fluorescent proteins at nanometer resolution*, Science **313**, 1642 (2006). — p.9, 19, 67, 91.

[10] T. Dertinger, R. Colyer, G. Iyer, S. Weiss, and J. Enderlein, *Fast, background-free, 3D super-resolution optical fluctuation imaging (SOFI)*, Proc. Natl. Acad. Sci. U.S.A. **106**, 22287 (2009). — p.9, 19, 67, 91.

[11] R. Heintzmann and M. G. L. Gustafsson, *Subdiffraction resolution in continuous samples*, Nature Photon. **3**, 362 (2009). — p.19, 25, 91.

[12] F. Wei and Z. Liu, *Plasmonic structured illumination microscopy*, Nano Lett. **10**, 2531 (2010). — p.19, 92.

[13] B. Gjonaj, J. Aulbach, P. M. Johnson, A. P. Mosk, L. Kuipers, and A. Lagendijk, *Active spatial control of plasmonic fields*, Nature Photon. **5**, 360 (2011). — p.19.

[14] B. Gjonaj, J. Aulbach, P. M. Johnson, A. P. Mosk, L. Kuipers, and A. Lagendijk, *Optical control of plasmonic bloch modes on periodic nanostructures*, Nano Lett. **12**, 546 (2012). — p.19.

[15] B. Gjonaj, *Digital plasmonics: From concept to microscopy*, Ph.D. thesis, University of Twente, 2012. — p.19.

[16] B. Gjonaj, J. Aulbach, P. M. Johnson, A. P. Mosk, L. Kuipers, and A. Lagendijk, *Focusing and scanning microscopy with propagating surface plasmons*, Phys. Rev. Lett. **110**, 266804 (2013). — p.19.

[17] F. Wei, D. Lu, W. Shen, H. Wan, J. L. Ponsetto, E. Huang, and H. Liu, *Wide field super-resolution surface imaging through plasmonic structured illumination microscopy*, Nano Lett. **14**, 4634 (2014). — p.19, 92.

[18] A. I. Fernández-Domínguez, Z. Liu, and J. B. Pendry, *Coherent four-fold super-resolution imaging with composite photonic-plasmonic structured illumination*, ACS Photonics **2**, 341 (2015). — p.19, 92.

[19] E. Mudry, K. Belkebir, J. Girard, J. Savatier, E. Le Moal, C. Nicoletti, M. Allain, and A. Sentenac, *Structured illumination microscopy using unknown speckle patterns*, Nature Photon. **6**, 312 (2012). — p.19, 27, 67, 68, 73, 75, 92.

[20] S. Dong, P. Nanda, R. Shiradkar, K. Guo, and G. Zheng, *High-resolution fluorescence imaging via pattern-illuminated Fourier ptychography*, Opt. Express **22**, 20856 (2014). — p.19, 27, 30, 73, 92.

[21] J. W. Goodman, *Introduction to Fourier Optics* (Roberts & Company, Englewood, 2005). — p.10, 11, 19, 21, 71, 80.

[22] F. Zernike, *The concept of degree of coherence and its application to optical problems*, Physica **5**, 785 (1938). — p.20, 52.

[23] F. Zernike, *Phase contrast, a new method for the microscopic observation of transparent objects*, Physica **9**, 686 (1942). — p.20.

[24] F. Zernike, *Phase contrast, a new method for the microscopic observation of transparent objects part II*, Physica **9**, 974 (1942). — p.20.

[25] G. Popescu, T. Ikeda, R. R. Dasari, and M. S. Feld, *Diffraction phase microscopy for quantifying cell structure and dynamics*, Opt. Lett. **31**, 775 (2006). — p.20.

[26] A. B. Parthasarathy, K. K. Chu, T. N. Ford, and J. Mertz, *Quantitative phase imaging using a partitioned detection aperture*, Opt. Lett. **37**, 4062 (2012). — p.20.

[27] T. N. Ford, K. K. Chu, and J. Mertz, *Phase-gradient microscopy in thick tissue with oblique back-illumination*, Nat. Methods **9**, 1195 (2012). — p.20.

[28] D. Huang, E. A. Swanson, C. P. Lin, J. S. Schuman, W. G. Stinson, W. Chang, M. R. Hee, T. Flotte, K. Gregory, C. A. Puliafito, and J. G. Fujimoto, *Optical coherence tomography*, Science **254**, 1178 (1991). — p.20.

[29] T. S. Ralston, D. L. Marks, P. S. Carney, and S. A. Boppart, *Interferometric synthetic aperture microscopy*, Nature Phys. **3**, 129 (2007). — p.20.

[30] I. J. Cox and C. J. R. Sheppard, *Information capacity and resolution in an optical system*, J. Opt. Soc. Am. A **3**, 1152 (1986). — p.10, 11, 21.

[31] S. Fürhapter, A. Jesacher, S. Bernet, and M. Ritsch-Marte, *Spiral phase contrast imaging in microscopy*, Opt. Express **13**, 689 (2005). — p.24.

[32] X. Chen and S. R. J. Brueck, *Imaging interferometric lithography: Approaching the resolution limits of optics*, Opt. Lett. **24**, 124 (1999). — p.9, 25.

[33] C. J. Schwarz, Y. Kuznetsova, and S. R. J. Brueck, *Imaging interferometric microscopy*, Opt. Lett. **28**, 1424 (2003). — p.25.

[34] V. Mico, Z. Zalevsky, P. García-Martínez, and J. García, *Synthetic aperture superresolution with multiple off-axis holograms*, J. Opt. Soc. Am. A **23**, 3162 (2006). — p.25.

[35] V. Mico, Z. Zalevsky, and J. García, *Synthetic aperture microscopy using off-axis illumination and polarization coding*, Opt. Commun. **276**, 209 (2007). — p.25.

[36] G. Zheng, R. Horstmeyer, and C. Yang, *Wide-field, high-resolution Fourier ptychographic microscopy*, Nature Photon. **7**, 739 (2013). — p.25, 72.

[37] I. M. Vellekoop, *Controlling the propagation of light in disordered scattering media*, Ph.D. thesis, University of Twente, 2008. — p.27.

[38] I. M. Vellekoop and A. P. Mosk, *Focusing coherent light through opaque strongly scattering media*, Opt. Lett. **32**, 2309 (2007). — p.10, 12, 27, 60.

[39] C. L. Hsieh, Y. Pu, R. Grange, G. Laporte, and D. Psaltis, *Imaging through turbid layers by scanning the phase conjugated second harmonic radiation from a nanoparticle*, Opt. Express **18**, 20723 (2010). — p.27, 58, 69, 76.

[40] I. M. Vellekoop and C. Aegerter, *Scattered light fluorescence microscopy: Imaging through turbid layers*, Opt. Lett. **35**, 1245 (2010). — p.27, 58, 69.

[41] E. G. van Putten, D. Akbulut, J. Bertolotti, W. L. Vos, A. Lagendijk, and A. P. Mosk, *Scattering lens resolves sub-100 nm structures with visible light*, Phys. Rev. Lett. **106**, 193905 (2011). — p.27, 52, 54, 58, 60, 62, 68, 69, 75, 76, 78, 92, 105, 111.

[42] O. Katz, E. Small, and Y. Silberberg, *Looking around corners and through thin turbid layers in real time with scattered incoherent light*, Nature Photon. **6**, 549 (2012). — p.27, 58, 69.

[43] X. Yang, C. L. Hsieh, Y. Pu, and D. Psaltis, *Three-dimensional scanning microscopy through thin turbid media*, Opt. Express **20**, 2500 (2012). — p.27, 58.

[44] H. He, Y. Guan, and J. Zhou, *Image restoration through thin turbid layers by correlation with a known object*, Opt. Express **21**, 12539 (2013). — p.27, 69.

[45] O. Katz, Y. Small, E.and Guan, and Y. Silberberg, *Noninvasive nonlinear focusing and imaging through strongly scattering turbid layers*, Optica **1**, 170 (2014). — p.27.

[46] J. García, Z. Zalevsky, and D. Fixler, *Synthetic aperture superresolution by speckle pattern projection*, Opt. Express **13**, 6073 (2005). — p.27, 28, 68, 75.

[47] S. Popoff, G. Lerosey, M. Fink, A. C. Boccara, and S. Gigan, *Image transmission through an opaque material*, Nat. Commun. **1**, (2010). — p.10, 27, 76.

[48] Y. Choi, M. Kim, C. Yoon, T. D. Yang, K. J. Lee, and W. Choi, *Synthetic aperture microscopy for high resolution imaging through a turbid medium*, Opt. Lett. **36**, 4263 (2011). — p.10, 27.

[49] Y. Choi, T. D. Yang, C. Fang-Yen, P. Kang, K. J. Lee, R. R. Dasari, M. S. Feld, and W. Choi, *Overcoming the diffraction limit using multiple light scattering in a highly disordered medium*, Phys. Rev. Lett. **107**, 023902 (2011). — p.10, 27, 76.

[50] J. Bertolotti, E. G. van Putten, C. Blum, A. Lagendijk, W. L. Vos, and A. P. Mosk, *Non-invasive imaging through opaque scattering layers*, Nature **491**, 232 (2012). — p.27, 28, 29, 38, 58, 69, 72, 99, 106, 112.

[51] X. Yang, Y. Pu, and D. Psaltis, *Imaging blood cells through scattering biological tissue using speckle scanning microscopy*, Opt. Express **22**, 3405 (2014). — p.27, 29, 69, 72, 106, 112.

[52] O. Katz, P. Heidmann, M. Fink, and S. Gigan, *Non-invasive single-shot imaging through scattering layers and around corners via speckle correlations*, Nature Photon. **8**, 784 (2014). — p.27, 29, 69, 72, 106, 112.

[53] K. T. Takasaki and J. W. Fleischer, *Phase-space measurement for depth-resolved memory-effect imaging*, Opt. Express **22**, 31426 (2015). — p.27, 29, 58.

[54] S. Kang, S. Jeong, W. Choi, H. Ko, T. D. Yang, J. H. Joo, J.-S. Lee, Y.-S. Lim, Q.-H. Park, and W. Choi, *Imaging deep within a scattering medium using collective accumulation of single-scattered waves*, Nature Photon. **9**, 253 (2015). — p.27.

[55] H. Yılmaz, *Advanced optical imaging with scattering lenses, Chapter 5*, Ph.D. thesis, University of Twente, 2015. — p.27, 29.

[56] S. Feng, C. Kane, P. A. Lee, and A. D. Stone, *Correlations and fluctuations of coherent wave transmission through disordered media*, Phys. Rev. Lett. **61**, 834 (1988). — p.27, 58, 69, 97, 106, 112.

[57] I. Freund, M. Rosenbluh, and S. Feng, *Memory effects in propagation of optical waves through disordered media*, Phys. Rev. Lett. **61**, 2328 (1988). — p.27, 58, 69, 97, 106, 112.

[58] B. Judkewitz, R. Horstmeyer, I. M. Vellekoop, and C. Yang, *Translation correlations in anisotropically scattering media*, arXiv:1411.7157 (2014). — p.27, 58.

[59] E. G. van Putten, *Disorder-enhanced imaging with spatially controlled light*, Ph.D. thesis, University of Twente, 2011. — p.28, 29, 53, 61.

[60] J. W. Goodman, *Statistical Optics* (Wiley, New York, 2000). — p.71.

[61] J. W. Goodman, *Speckle Phenomena in Optics* (Roberts & Company, Englewood, 2006). — p.28.

[62] J. R. Fienup, *Reconstruction of an object from the modulus of its Fourier transform*, Opt. Lett. **3**, 27 (1978). — p.29, 71, 99, 106, 112.

[63] J. R. Fienup, *Phase retrieval algorithms: A comparison*, Appl. Opt. **21**, 2758 (1982). — p.29, 71, 78, 99, 106, 112.

[64] R. P. Millane, *Phase retrieval in crystallography and optics*, J. Opt. Soc. Am. A **7**, 394 (1990). — p.29, 71, 72, 106, 112.

[65] Y. Shechtman, Y. C. Eldar, O. Cohen, H. N. Chapman, J. Miao, and M. Segev, *Phase retrieval with application to optical imaging: A contemporary overview*, IEEE Signal Processing Mag. **32**, 87 (2015). — p.29, 72, 99, 106, 112.

CHAPTER 3

Optimal control of light propagation through multiple-scattering media in the presence of noise

We study the control of coherent light propagation through multiple-scattering media in the presence of measurement noise. In our experiments, we use a two-step optimization procedure to find the optimal incident wavefront that generates a bright focal spot behind the medium. We conclude that the control of coherent light propagation through a multiple-scattering medium is only determined by the number of photoelectrons detected per optimized segment. The prediction of our model agrees well with the experimental results. Our results offer opportunities for imaging applications through scattering media such as biological tissue in the shot noise limit.

3.1 Introduction

Spatial inhomogeneities in the refractive index of a material such as paper, white paint or biological tissue cause multiple scattering of light. Light propagates diffusively through such materials, which makes the control of light propagation through these kind of materials impossible with conventional optics. A multiple-scattering medium has for a long time been considered as a barrier to optical propagation. It has been theoretically predicted that a multiple-scattering medium can act as a high-precision optical device such as a thin lens, mirror, polarizer or Fourier analyser [1]. The first optical lens made of multiple-scattering medium was demonstrated by manipulating the incident light field, which starts a new research topic in optics called wavefront shaping [2].

Many applications of wavefront shaping have recently been demonstrated in advanced optics, biophotonics, nanotechnology, and biomedical imaging [3]. Optical pulse compressors have been realized using wavefront shaping [4–6]. It has been shown that a multiple-scattering medium can be used as a high numerical aperture lens [7] that enables sub-100 nm optical resolution [8]. Recently, wave plates and spectral filters made of multiple-scattering media have been realized [9–12]. Fluorescence imaging inside biological tissue has been demonstrated

This chapter has been published as: H. Yılmaz, W. L. Vos, and A. P. Mosk, Biomed. Opt. Express **4**, 759-1768 (2013).

by scanning the optical focus guided by acoustic focus [13, 14]. In addition, a non-invasive imaging technique was reported, in which a fluorescent biological object hidden behind a scattering medium was imaged [15].

Transforming a multiple-scattering medium into a high-precision optical device requires a high degree of control of light propagation through the medium. Control over the propagation of light through a multiple-scattering medium is quantified by a figure of merit that is given by the intensity enhancement. The enhancement is equal to $\eta = I_{\text{opt}}/\langle I_{\text{A}} \rangle$ where I_{opt} is the intensity in the target after optimization and $\langle I_{\text{A}} \rangle$ is the ensemble averaged intensity in the target before the optimization [16].

Many wavefront shaping methods have been reported to focus light through multiple-scattering media [16–25]. All of these wavefront shaping methods are essentially based on the measurement of a part of the transmission matrix, which is the complex field response of the medium in the transmission to a set of input field bases. Using the information in the transmission matrix, one can synthesize the optimum field to focus light through the medium. It has been shown that the enhancement depends linearly on the number of degrees of freedom that are controlled until it reaches a saturation where practical limitations become prominent [2]. Therefore, we compare the maximal enhancements reported from various wavefront shaping and transmission matrix experiments. In early wavefront shaping experiments it was shown that one row of the transmission matrix gives the information to focus light through to a particular position behind the multiple-scattering medium resulting in an enhancement up to $\eta = 1000$ [2] using 3228 segments. An enhancement $\eta = 54$ has been reported by Popoff *et al.* using 256 segments [17]. In their experiment, the transmission matrix of a multiple-scattering medium was measured and the information of the transmission matrix was used to create a focus through the medium on any selected position [17]. Using the transmission matrix approach, the transmission of an image is demonstrated through a multiple-scattering medium [26]. Cui reported an enhancement $\eta = 270$ using a parallel optimization method with 441 segments [22]. An enhancement $\eta = 454$ has been reported by Conkey *et al.* using 1024 segments [24]. Park *et al.* reported an enhancement $\eta = 400$ using 1681 segments [9]. The optimal enhancements reported here range from 50 to 1000. It remains an open question what the cause of the wide variation of the enhancement in different experiments is. In addition, genetic algorithms have been used for wavefront shaping, and they appear to produce enhancement values in the same range [10, 23] suggesting they may be subject to similar limitations. However, non-linear algorithms such as genetic algorithms [27, 28] are not within the scope of this paper and investigation of the fundamental limitation of the enhancement factor using genetic algorithms is an interesting subject for further research.

It has been suggested that measurement noise causes phase errors in the optimization (such as noise causes phase errors in phase contrast imaging techniques [29]) which limit the enhancement [16]. To our knowledge the effect of measurement noise on the enhancement factor has not been investigated. Therefore we present in this chapter an experimental and theoretical study of the in-

fluence of the noise on the enhancement factor using linear algorithms. We show a two-step sequential optimization algorithm that leads to the optimal enhancement using a linear algorithm in the presence of noise. The optimal enhancement in this case is found to be given by basic physical principles, namely quantum noise in the photodetection process.

3.2 The experimental setup

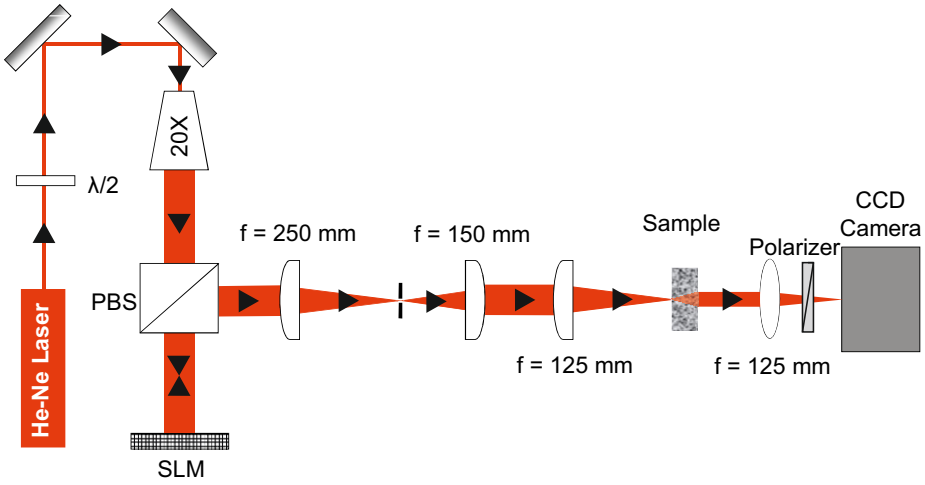

Figure 3.1: The experimental setup for wavefront shaping. Laser light reflected by the SLM is focused on a white ZnO sample. The light transmitted through the sample is detected by a CCD camera. Abbreviations used, SLM: Spatial light modulator, PBS: polarizing beam splitter, $\lambda/2$: half-wave plate, CCD:charge coupled device, 20×: 20× beam expander.

Our experimental setup is shown in Fig. 3.1. The light source is a He-Ne laser with wavelength $\lambda = 632.8$ nm, output power 5 mW, noise level of 0.2% and a long term power drift of 6%. We intentionally use a laser with a high noise and drift. A half wave plate sets the polarization and the beam is expanded to a diameter of 20 mm by a beam expander. The light is transmitted through a polarizing beam splitter and illuminates a spatial light modulator (Holoeye LC-R 2500). The spatial light modulator (SLM) consists of a twisted nematic liquid crystal cell which couples phase and polarization modulation. We used a multipixel modulation method described in reference [30] to obtain independent phase and amplitude modulation with a single SLM. The two lenses and the pinhole after the polarizing beam splitter are a spatial filter used for the amplitude and phase modulation method. The modulated light is reflected by the polarizing beam splitter and focused on the scattering layer of the sample by a lens with a focal

length of 125 mm. The sample is made by spray coating of ZnO nanoparticles on a glass cover slide with a thickness of 170 μm. The scattering ZnO layer has a mean free path of 0.65 μm and a thickness of 10 μm. The Fourier plane of the backside of the sample is imaged on a CCD camera (Allied Vision Technologies Dolphin F-145B) by a lens with a focal length of 125 mm. A polarizer before the CCD camera selects a single polarization. The CCD signal is read out in counts, where we determined that 1 count corresponds to 1.7 photoelectrons. The CCD camera has a read-out noise with a variance of 10 (count^2).

3.3 The enhancement factor in the presence of noise

In the wavefront shaping experiment, the SLM surface is divided into a large number of segments N. We choose $N = 850$ in all experiments described here. Each segment contains several pixels. The first selected segment is phase modulated in quadrant steps between $\Delta\theta = 0$ and $\Delta\theta = 2\pi$. We monitor the target signal I_0 by integrating the intensity in a disk shaped target area on the CCD with the same size of a single speckle spot while modulating the phase, which results in a sinusoidal signal on top of a background. A sketch of the measured signal during one phase cycle is shown in Fig. 3.2. We find the optimal phase for the maximal target signal for the corresponding segment, however we do not immediately display the optimal phase on the SLM. The same procedure is applied to all N segments one by one, which yields one row of the transmission matrix. In the end of the measurement of all N optimal phases, we display all N optimal phases on the SLM. We see in Fig. 3.2 that the target signal on the CCD camera during the phase modulation of a single segment in the presence of noise is

$$\begin{aligned} I_0 &= I_\mathrm{A} + I_\mathrm{B} + 2\sqrt{I_\mathrm{A} I_\mathrm{B}}\cos(\Delta\theta + \phi) + \sigma \\ &= B + S\cos(\Delta\theta + \phi) + \sigma, \end{aligned} \tag{3.1}$$

where I_A is the intensity coming from the total unmodulated SLM segments, I_B the intensity coming from the modulated single SLM segment. Here we define B as the background, S the modulation signal, $\Delta\theta$ the phase, ϕ the phase offset, and σ the standard deviation of noise. The average amplitude of the modulation signal is

$$S = 2I_\mathrm{A}\sqrt{\frac{1}{N}}. \tag{3.2}$$

We use a constant area on the SLM, therefore the segment size decreases with segment number N. In Eq. (3.2) we see that a larger N leads to a smaller signal S.

Since we update all phase values in the end of the optimization, the signal S and the noise do not change during the optimization. For a phase determination based on quadrature phase detection (measurements 90°out of phase) we find a

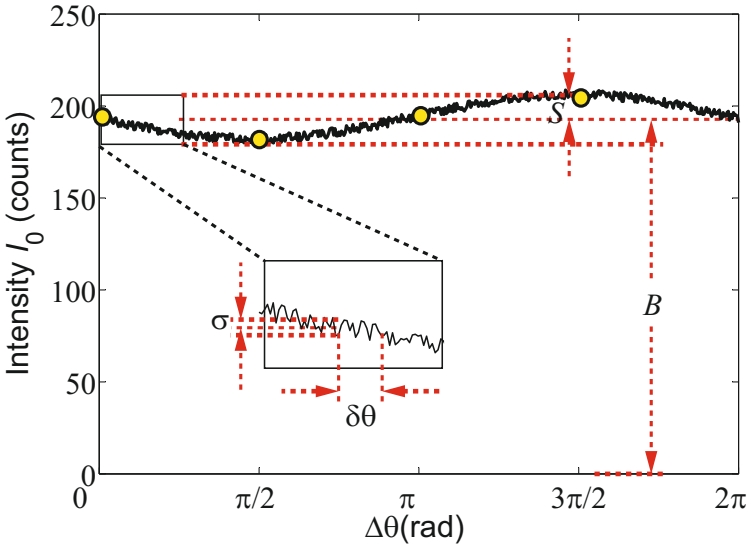

Figure 3.2: Cartoon showing the effect of the noise on phase estimation. The target intensity I_0 is shown versus the phase $\Delta\theta$. The modulation signal S and the background B at the target position are shown during the phase modulation $\Delta\theta$ of a single segment. The standard deviation of the noise is represented by σ, and the standard deviation of the phase is represented by $\delta\theta$. Yellow dots represent the measurements used to construct the quadratures.

phase error $\delta\theta$ [31] in the measurement equal to

$$\langle\delta\theta\rangle_{\mathrm{RMS}} = \frac{\sigma}{S}. \tag{3.3}$$

Here the standard deviation of noise σ and the signal S is considered for a given photon budget per optimized segment. The root mean square phase error $\langle\delta\theta\rangle_{\mathrm{RMS}}$ is averaged over all segments and is assumed to be $\langle\delta\theta\rangle_{\mathrm{RMS}} << 1$. Assuming uncorrelated phase errors, the enhancement factor η becomes

$$\eta = \frac{\pi}{4} N \langle\cos^2\delta\theta\rangle, \tag{3.4}$$

which is valid for a large number of segments $N >> 1$. For small phase errors ($\delta\theta << 1$) the expression simplifies to

$$\eta = \frac{\pi}{4} N (1 - \langle\delta\theta^2\rangle). \tag{3.5}$$

Inserting Eq. (3.3) into Eq. (3.5) we obtain the enhancement

$$\eta = \frac{\pi}{4} N \left(1 - \frac{\sigma^2}{S^2}\right). \tag{3.6}$$

Eq. (3.6) shows that the enhancement depends both on the number of segments N and on the noise σ. Note that Eq. (3.6) is valid under the condition that the modulation signal S is larger than noise σ.

The modulation signal S depends on the number of segments N as $S \propto N^{-1/2}$, whereas the noise σ does not depend on N. Therefore it is useful to define a normalized signal to noise ratio R that does not depend on the number of segments N as

$$R = \frac{SN^{1/2}}{\sigma}. \tag{3.7}$$

We arrive at an expression for the enhancement η in which the dependence on N is explicit,

$$\eta = \frac{\pi}{4} N \left(1 - \frac{N}{R^2}\right). \tag{3.8}$$

It is remarkable in Eq. (3.8) that the enhancement is not proportional to the number of segments N. The enhancement follows a parabolic function which has a maximum equal to

$$\eta_{\max} = \frac{\pi R^2}{16}. \tag{3.9}$$

The maximum is obtained by selecting the optimal number of segments to be equal to $N_{\text{opt}} = R^2/2$. The only way to further increase the enhancement above this maximum is of course to improve the normalized signal to noise ratio R.

3.4 Pre-optimization

In order to improve the normalized signal to noise ratio R without changing the incident photon budget, we perform a two-step optimization procedure [2]. In Fig. 3.3, we show a schematic of this two-step optimization method. We first perform an optimization with a small number of segments N_{pre}, leading to a moderate enhancement η_{pre} (Fig. 3.3(b)). The phase map resulting from the pre-optimization is displayed during the whole duration of the second optimization step. As a result of pre-optimization, we obtain a higher modulation signal S on the target spot in the second step see Fig. 3.3(d). In addition, the pre-optimization step provides a locally constant beam profile on the target position, thereby making the measurement robust against mechanical vibrations in the second step. In the second optimization step, we use a much larger number of segments ($N = 850$) to obtain the final enhancement. We performed the same procedure with different values of N_{pre} several times to obtain different values of η_{pre}.

The target intensity detected on CCD after pre-optimization is equal to

$$I_0 = B + 2I_{\text{A}}\sqrt{\frac{\eta_{\text{pre}}}{N}}\cos(\Delta\theta + \phi) \tag{3.10}$$

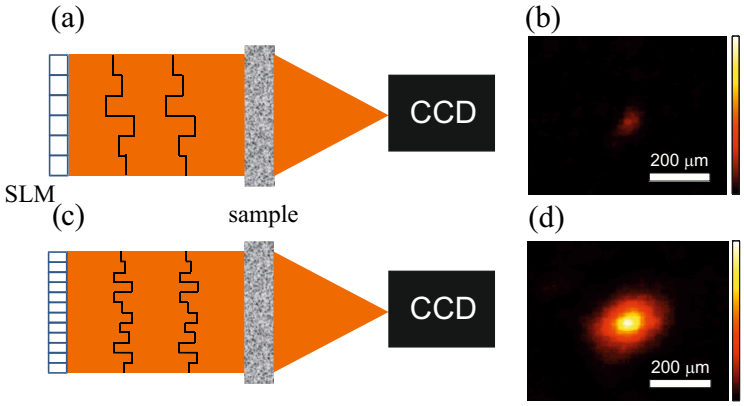

Figure 3.3: Cartoon shows the phase map on the SLM after the pre-optimization (a), and after the second optimization (c). The focal spot at the target position after a pre-optimization (b), and after the second optimization (d).

where the modulation signal S becomes

$$S = 2I_{\mathrm{A}}\sqrt{\frac{\eta_{\mathrm{pre}}}{N}}. \tag{3.11}$$

As seen in Eq. (3.11), a pre-optimization increases S, therefore we expect to improve the normalized signal to noise ratio R.

The desired effect of the pre-optimization is to increase the modulation signal S, but it also has an effect on the noise σ. Different contributions to the noise depend on the pre-enhancement η_{pre} in a different way. In our two-step optimization, there are three different significant noise contributions which are (1) the camera read-out noise, (2) the shot noise, and (3) the laser excess noise. In Fig. 3.4 we show the three types of normalized noise to signal ratio versus η_{pre} for our experimental situation. The camera read-out noise is suppressed with a higher η_{pre}. The pre-optimization step improves R when the experiment is limited by the camera read-out noise. The effect of shot noise on R is independent of the pre-optimization step. A higher η_{pre} leads to a higher intensity in the target and therefore the laser excess noise, which is proportional to target intensity becomes stronger. As a result, an optimal pre-optimization step must be carefully chosen to achieve a shot noise limited signal. The best signal is found for a pre-enhancement that lies in between the low intensity regime where camera read-out noise is significant and the high intensity regime where laser excess noise reduces the enhancement.

Another approach to optimize the incident wavefront is updating each segment immediately after the measurement of optimal phase. Using this algorithm, both S and σ change during the optimization procedure. Essentially this means η_{pre} is being updated in the whole optimization procedure. This procedure has the advantage of rapidly climbing out of the low intensity region where camera read-

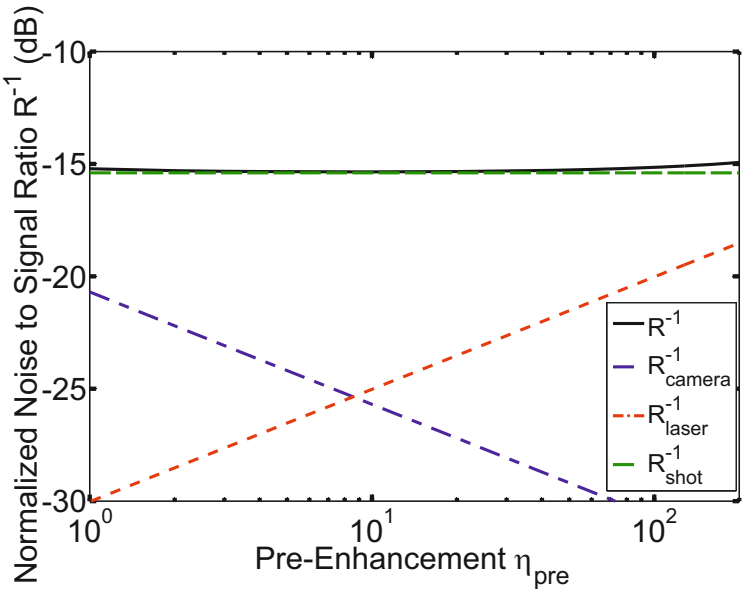

Figure 3.4: Three contributions to the normalized noise to signal ratio versus the pre-enhancement factor at a fixed photon budget. The black curve shows the total noise to signal ratio. The dashed green curve represents the noise to signal ratio when there is only shot noise, the dashed blue curve the noise to signal ratio when there is only camera read-out noise, and the dashed red curve the noise to signal ratio when there is only laser excess noise.

out noise is important. However, as η_{pre} continues to increase the algorithm will leave the low noise region and enters the region where laser excess noise is significant. A two-step optimization gives us the opportunity to perform the complete second step in the optimal region of η_{pre} thereby gathering maximal information per segment measurement.

We obtain the noise parameters from independent measurements. The noise that arises from the camera read out does not depend on the number of counts on the detector and is simply equal to the variance of the dark counts of the CCD. The standard deviation of shot noise is equal to the square root of the ensemble averaged intensity on the target position measured in photoelectrons. The laser excess noise is found by measuring the laser intensity on the target position in time.

In Fig. 3.5 we show the measured final enhancement as well as the result of Eq. (3.8) versus the pre-enhancement. Both the experiments and the model are based on two-step sequential algorithm. Each data point represents a single measurement. Different values of η_{pre} are obtained by varying N_{pre} between 1 and 850 in each measurement. We choose $N = 850$ in all measurements. We used a fixed integration time as 83 ms and fixed laser power for a fixed photon budget

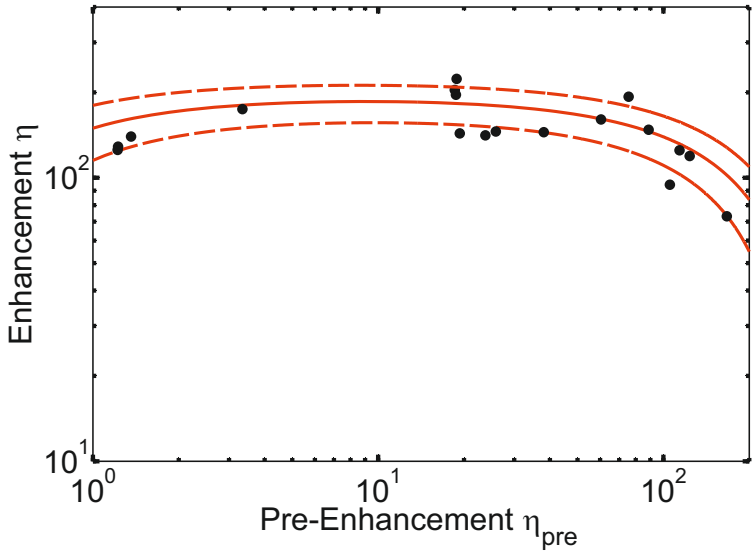

Figure 3.5: The final enhancement versus the pre-enhancement. The black dots show the experimental data. The red curve shows the enhancement according to Eq. (3.8) without adjustable parameters. The area between dashed red lines expresses the uncertainty region of the enhancement factor due to intensity drift at the target position during optimization.

per optimized segment. At low η_{pre}, we observe that the final enhancement rises slightly with η_{pre}, until it reaches a plateau at $\eta_{\mathrm{pre}} \approx 10$. This rise is due to suppression of the camera read-out noise as more signal impinges on the camera. In the plateau the final enhancement is limited only by the shot noise. A further rise in η_{pre} decreases the final enhancement due to increase of the laser excess noise. When the pre-enhancement is very high ($\eta_{\mathrm{pre}} > 100$) the final enhancement is below the pre-enhancement ($\eta_{\mathrm{pre}} > \eta$). In this case, the enhancement is limited by laser excess noise. The measured enhancements vary with an RMS variation of 60 which is caused by the long term laser power drift. The average laser power during the optimization varies by 6%. This leads to a change of the shot noise which results in a variation of the enhancement factor. It is seen in Fig. 3.5 that the measured enhancement agrees very well with the model predictions with no adjustable parameters.

3.5 The maximal enhancement in the shot noise limit

The pre-optimization step with $\eta_{\mathrm{pre}} \approx 10$ suppresses the camera read-out noise which brings the experiment into the shot noise limited regime. In the shot noise limited regime $\sigma = (\eta_{\mathrm{pre}}\langle I_{\mathrm{A}}\rangle)^{1/2}$, therefore using Eq. (3.7) the normalized signal

to noise ratio is $R = 2(\langle I_A \rangle)^{1/2}$. Ensemble averaged target intensity $\langle I_A \rangle$ can be obtained by averaging the target intensity on the CCD over several random incident wavefronts. In Eq. (3.9) we obtain maximal enhancement in shot noise limit shown as

$$\eta_{max} = \frac{\pi \langle I_A \rangle}{4}. \tag{3.12}$$

This equation shows η_{max} is only proportional to the number of ensemble averaged photoelectrons detected per optimized segment in a given photon budget.

In case an optimization is performed with limited laser power and within a limited time, as is relevant in dynamic environments, there is a fixed photon budget for the whole optimization and increasing N will lead to a smaller number of photons per measurement. In the case of a fixed photon budget for the whole optimization we can use the same derivation and find a slightly different result, namely $\eta_{max} = (\pi/6)(I_T/3)^{1/2}$, where I_T is the total number of detected photons. Remarkably for a fixed photon budget per optimization the maximal enhancement is proportional to the square root of the photon budget.

3.6 Conclusion

Wavefront shaping experiments using phase only modulation and linear algorithms reported in literature show a range of enhancements between 50 and 1000. In most of those experiments the limiting factor is likely to be noise. Therefore we have investigated wavefont shaping by feedback in the presence of experimental noise. We distinguish the effect of three types of noise namely the camera read-out noise, the shot noise, and the laser excess noise. The camera read-out noise can be reduced using a two-step optimization procedure. Two-step optimization is remarkably robust; even with a low-end camera and a very noisy laser, we show this procedure obtains shot noise limited performance. We obtain a maximal enhancement that is only proportional to the number of photoelectrons detected per optimized segment.

A wavefront shaping experiment requires the measurement of one row of the transmission matrix of the multiple-scattering medium. A focusing experiment with high enhancement factor is a signature of a precise transmission matrix measurement. Our measurements show that a wavefront shaping experiment using phase only modulation and linear algorithms is limited by basic physical principles, namely quantized detection of light. Therefore we conclude that our two-step optimization method can be used to realize shot noise limited transmission matrix measurements. In addition, our method can be used to achieve shot noise limited signal for applications such as imaging through opaque biological tissue.

Bibliography

[1] I. Freund, *Looking through walls and around corners*, Physica A **168**, 49 (1990). — p.37.

[2] I. M. Vellekoop and A. P. Mosk, *Focusing coherent light through opaque strongly scattering media*, Opt. Lett. **32**, 2309 (2007). — p.37, 38, 42.

[3] A. P. Mosk, A. Lagendijk, G. Lerosey, and M. Fink, *Controlling waves in space and time for imaging and focusing in complex media*, Nature Photon. **6**, 283 (2012). — p.10, 37, 58, 60.

[4] J. Aulbach, B. Gjonaj, P. M. Johnson, A. P. Mosk, and A. Lagendijk, *Control of light transmission through opaque scattering media in space and time*, Phys. Rev. Lett. **106**, 103901 (2011). — p.37.

[5] O. Katz, E. Small, Y. Bromberg, and Y. Silberberg, *Focusing and compression of ultrashort pulses through scattering media*, Nature Photon. **5**, 372 (2011). — p.37.

[6] D. J. McCabe, A. Tajalli, D. R. Austin, P. Bondareff, I. A. Walmsley, S. Gigan, and B. Chatel, *Spatio-temporal focusing of an ultrafast pulse through a multiply scattering medium*, Nature Commun. **2**, 447 (2011). — p.37.

[7] I. M. Vellekoop, A. Lagendijk, and A. P. Mosk, *Exploiting disorder for perfect focusing*, Nature Photon. **4**, 320 (2010). — p.37.

[8] E. G. van Putten, D. Akbulut, J. Bertolotti, W. L. Vos, A. Lagendijk, and A. P. Mosk, *Scattering lens resolves sub-100 nm structures with visible light*, Phys. Rev. Lett. **106**, 193905 (2011). — p.37.

[9] J. H. Park, C. Park, H. Yu, Y. H. Cho, and Y. Park, *Dynamic active wave plate using random nanoparticles*, Opt. Express **20**, 17010 (2012). — p.37, 38.

[10] Y. F. Guan, O. Katz, E. Small, J. Y. Zhou, and Y. Silberberg, *Polarization control of multiply scattered light through random media by wavefront shaping*, Opt. Lett. **37**, 4663 (2012). — p.37, 38.

[11] J. H. Park, C. Park, H. Yu, and Y. Cho, Y. H. Park, *Active spectral filtering through turbid media*, Opt. Lett. **37**, 3261 (2012). — p.37.

[12] E. Small, O. Katz, Y. F. Guan, and Y. Silberberg, *Spectral control of broadband light through random media by wavefront shaping*, Opt. Lett. **37**, 3429 (2012). — p.37.

[13] Y. M. Wang, B. Judkewitz, and C. H. DiMarzio, C. A. Yang, *Deep-tissue focal fluorescence imaging with digitally time-reversed ultrasound-encoded light*, Nature Commun. **3**, 928 (2012). — p.38.

[14] K. Si, R. Fiolka, and M. Cui, *Fluorescence imaging beyond the ballistic regime by ultrasound-pulse-guided digital phase conjugation*, Nature Photon. **6**, 657 (2012). — p.38.

[15] J. Bertolotti, E. G. van Putten, C. Blum, A. Lagendijk, W. L. Vos, and A. P. Mosk, *Non-invasive imaging through opaque scattering layers*, Nature **491**, 232 (2012). — p.27, 28, 29, 38, 58, 69, 72, 99, 106, 112.

[16] I. M. Vellekoop and A. P. Mosk, *Phase control algorithms for focusing light through turbid media*, Opt. Commun. **281**, 3071 (2008). — p.38.

[17] S. M. Popoff, G. Lerosey, R. Carminati, M. Fink, A. C. Boccara, and S. Gigan, *Measuring the transmission matrix in optics: An approach to the study and control of light propagation in disordered media*, Phys. Rev. Lett. **104**, 100601 (2010). — p.38.

[18] Z. Yaqoob, D. Psaltis, M. S. Feld, and C. H. Yang, *Optical phase conjugation for turbidity suppression in biological samples*, Nature Photon. **2**, 110 (2008). — p.38.

[19] M. Cui and C. H. Yang, *Implementation of a digital optical phase conjugation system and its application to study the robustness of turbidity suppression by phase conjugation*, Opt. Express **18**, 3444 (2010). — p.38.

[20] C. L. Hsieh, Y. Pu, R. Grange, and D. Psaltis, *Digital phase conjugation of second harmonic radiation emitted by nanoparticles in turbid media*, Opt. Express **18**, 12283 (2010). — p.38.

[21] D. Akbulut, T. J. Huisman, E. G. van Putten, W. L. Vos, and A. P. Mosk, *Focusing light through random photonic media by binary amplitude modulation*, Opt. Express **19**, 4017 (2011). — p.38.

[22] M. Cui, *Parallel wavefront optimization method for focusing light through random scattering media*, Opt. Lett. **36**, 870 (2011). — p.38.

[23] D. B. Conkey, A. N. Brown, A. M. Caravaca-Aguirre, and R. Piestun, *Genetic algorithm optimization for focusing through turbid media in noisy environments*, Opt. Express **20**, 4840 (2012). — p.38.

[24] D. B. Conkey, A. M. Caravaca-Aguirre, and R. Piestun, *High-speed scattering medium characterization with application to focusing light through turbid media*, Opt. Express **20**, 1733 (2012). — p.38.

[25] C. Stockbridge, Y. Lu, J. Moore, S. Hoffman, R. Paxman, K. Toussaint, and T. Bifano, *Focusing through dynamic scattering media*, Opt. Express **20**, 15086 (2012). — p.38.

[26] S. Popoff, G. Lerosey, M. Fink, A. C. Boccara, and S. Gigan, *Image transmission through an opaque material*, Nature Commun. **1**, 81 (2010). — p.38.

[27] T. Weise, M. Zapf, R. Chiong, and A. J. Nebro, *Nature-inspired algorithms for optimisation* (Springer, 2009). — p.38.

[28] T. Weise, R. Chiong, and K. Tang, *Evolutionary optimization: Pitfalls and booby traps*, J. Comput. Sci.Technol. **27**, 907 (2012). — p.38.

[29] A. B. Parthasarathy, K. K. Chu, T. N. Ford, and J. Mertz, *Quantitative phase imaging using a partitioned detection aperture*, Opt. Lett. **37**, 4062 (2012). — p.38.

[30] E. G. van Putten, I. M. Vellekoop, and A. P. Mosk, *Spatial amplitude and phase modulation using commercial twisted nematic LCDs*, Appl. Opt. **47**, 2076 (2008). — p.39.

[31] S. A. Tretter, *Estimating the frequency of a noisy sinusoid by linear regression*, IEEE Trans. Inform. Theor. **31**, 832 (1985). — p.41.

CHAPTER 4

Fabrication and characterization of scattering solid immersion lenses for high-resolution optical imaging

High-resolution optical imaging has great importance both in fundamental and applied sciences. One approach to reach a high optical resolution is using solid immersion lenses. The diffraction-limited resolution of a solid immersion lens is inversely proportional to the refractive index of the lens material. So far, aberration-free solid immersion lenses of very high index materials have not been demonstrated in the visible range. Scattering solid immersion lenses exploit high-angle internal scattering in high-index materials. They are easy to fabricate, however until recently it was difficult to characterize them, as there was no convenient method to measure the intensity of high-angle internal light scattering in very high-index substrates. In this chapter, we demonstrate a method to measure the high-angle internal scattering efficiency of scattering solid immersion lenses. We apply this method to a new scattering solid immersion lens that is made of a gallium phosphide (GaP) substrate with an unpolished rough surface. Our new scattering solid immersion lens offers sub-100 nm optical imaging of nanostructures with a higher light efficiency than the existing electrochemically etched porous scattering solid immersion lenses.

4.1 Introduction

Solid immersion lenses have many applications such as high-density optical data storage [1, 2], high light collection efficiency [3], near-field scanning optical microscopy [4], high-resolution photolithography [5], and integrated circuit failure analysis [6–8]. Solid immersion lens microscopy enables high-resolution optical imaging of nanostructures [9]. A hemisphere of a high-index material such as gallium phosphide (GaP) is used as both a lens and a surrounding medium that ensures a high numerical aperture (NA) [10]. However, a hemispherical solid immersion lens introduces wavefront errors that are proportional to the refractive index contrast and the fabrication errors on the surface of the hemisphere. The full resolving power of a GaP solid immersion lens has not yet been achieved due to the limitations on fabrication of these lenses [11]. Moreover, multiple internal reflections reduce the resolution and contrast of solid immersion lenses [12].

As an alternative approach, a diffraction-based solid immersion lens has been demonstrated [13]. However, a diffraction-based solid immersion lens does not suit for imaging nanostructures under ambient conditions, since its performance depends critically on the environmental conditions and it is very challenging to obtain diffraction-limited images because of unavoidable fabrication defects.

Light scattering offers an alternative way to access to high-spatial-frequency information [14]. This principle is exploited with scattering lenses [15]. It has been shown that a scattering lens enables a diffraction-limited bright focus even with a low-intensity and noisy light source [16]. A high-NA scattering solid immersion lens (SSIL) offers sub-100 nm resolution with visible light [17]. A high-NA SSIL is a slab of a very high-index material of which one surface is strongly scattering. An ideal SSIL has a high transmission of scattered light, a low transmission of ballistic light, a high scattering efficiency at high internal-angles, and a mechanism for suppression of multiple internal reflections. So far, high-NA SSILs have been made using a GaP substrate, of which one surface is polished and one surface is porous. The polished surface is coated with an absorptive silicon (Si) layer to suppress multiple internal reflections. The porous layer is prepared by electrochemical etching [18, 19]. The porous layer is optically very thick; about 10 transport mean free paths. Therefore, there is no transmission of ballistic light. However, most of the incident light on the porous layer is scattered back. A thinner scattering layer is necessary for a more efficient SSIL. GaP wafers with one surface polished and one rough surface unpolished are commercially available. Here, we systematically measure the angular dependence of scattered light intensity from a rough GaP SSIL and a porous GaP SSIL. We found the scattering surface of a rough GaP SSIL obeys Lambert's cosine law even for very high internal-angles, whereas the scattering layer of a porous GaP SSIL deviates from Lambert's cosine law. We found there is more scattered light from a rough GaP SSIL compared to a porous GaP SSIL. We imaged a gold nanoparticle with a size of 50 nm using a rough GaP SSIL. We showed a rough GaP SSIL enables a sub-100 nm resolution with visible light.

4.2 Principle of the scattering solid immersion lens

In Fig. 4.1 the principle of a high-NA SSIL is shown. A slab of a high-index material such as gallium phosphide (GaP) refracts incident light to the normal of the slab. Considering the very high refractive index up to $n = 3.4$ of the material, light is refracted to a very narrow range of angles close to the surface normal inside the material as seen in Fig. 4.1a. The useful information density of an arbitrary random wavefront is not enhanced. Therefore a slab of a high-index material is not sufficient for high-resolution solid immersion microscopy. In Fig 4.1b a high-NA SSIL that is composed of a high-index substrate with a scattering layer on one side is shown. A scattering layer enables light injection at high internal-angles inside the high-index slab. The information density of the wavefront is enhanced due to random scattering of the incident light beam and the possible resolution is extended to the full resolution of a solid immersion lens.

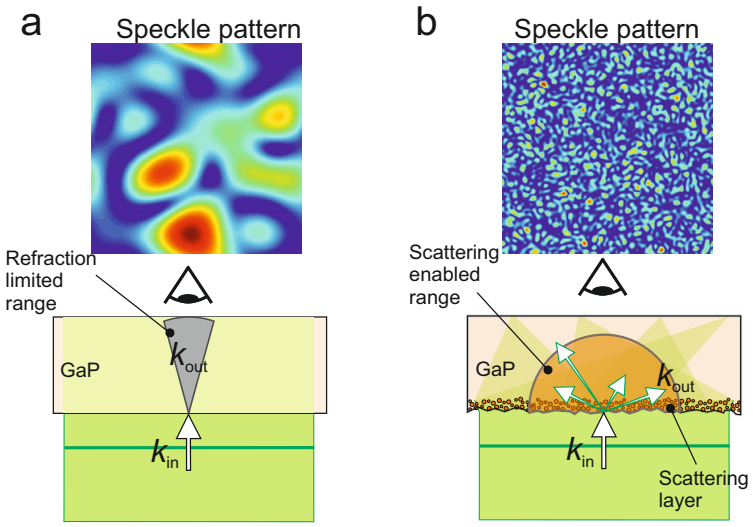

Figure 4.1: The concept of the high-NA scattering solid immersion lens (SSIL). (a) An incident wavefront on a very high-index substrate refracts to a very narrow range of angles close to the normal of the substrate. The speckle grain size of a random incident wavefront cannot be higher than the diffraction-limited beam size in the air. Information density of the wavefront does not change. (b) An incident wavefront scatters to all directions inside the substrate due to the scattering layer. The speckle grain size inside the substrate is $n = 3.4$ times smaller compared to the speckle grain size in the air. The information density of the wavefront is enhanced by a factor of $n^2 = 11.5$. The figure is adapted from reference [20].

4.3 High internal-angle scattered light of the GaP scattering solid immersion lenses

It has been shown that interfaces of scattering layers affect the angular distribution of transmitted light through a scattering medium [19]. The angular redistribution of the scattered light is partly due to the Fresnel-like refractions on interfaces [21]. Theories based on effective medium concepts [21] do not predict strong scattering to high internal-angles. Therefore it is expected that interface roughness between the scattering layer and the substrate of a high-NA SSIL dominates the scattered light intensity for high internal-angles. To obtain high resolution with a SSIL, the scattered light intensity for high internal-angles should be high enough to obtain a reasonable signal-to-noise ratio. In this section, we demonstrate a method to measure high internal-angle scattering at the interfaces of SSILs. We measured the scattering properties of two types of GaP SSILs at very high internal-angles. We compared the scattered light intensity of the GaP SSIL as in Ref. [17] to a GaP SSIL with an unpolished rough surface. We found there is sufficient high internal-angle scattering of a rough GaP SSIL for high-resolution optical imaging.

4.3.1 Experiment

In order to compare the scattered light intensity of two different types of GaP SSILs at high internal-angles, we designed an experiment as shown in Fig. 4.2. We placed both rough GaP SSIL and porous GaP SSIL on a cover slide. The rough GaP SSIL is made of a 400-µm-thick GaP substrate, one side is polished and coated with a 200-nm-thick Si antireflection layer, and one side is unpolished. The porous GaP SSIL is a similar scattering lens to the scattering lens in Ref. [17]. Briefly, the GaP wafer was electrochemically etched [18] to produce a 2-µm porous scattering layer. We focused a laser beam with a wavelength of 640 nm (OBIS LX 640-100) on the center of the edge of the porous GaP SSIL using a microscope objective (Zeiss: Infinity corrected, 63×, NA = 0.95). We imaged the scattering surface onto a CCD camera (Allied Vision Technologies Dolphin F-145B) in 2f-2f configuration using a lens with a focal length of 200 mm. We recorded the image of the scattered light from the porous GaP SSIL. We repeated the same procedure for the rough GaP SSIL.

In Figs. 4.3a and 4.3b the out of plane scattering intensity images of the porous GaP SSIL and the rough GaP SSIL are shown respectively. In Figs. 4.3c and 4.3d the integrated scattered light intensity in the transversal direction versus the x position plots from the porous GaP SSIL and the rough GaP SSIL are shown respectively. The first two peaks in the plots in Figs. 4.3c and 4.3d are due to the back reflection from the edges of the GaP SSILS. The peak intensities at about 1 mm are due to the incident light cones on the scattering surfaces of GaP SSILs. It is evident that there is much more scattered light from the rough GaP SSIL compared to porous GaP SSIL.

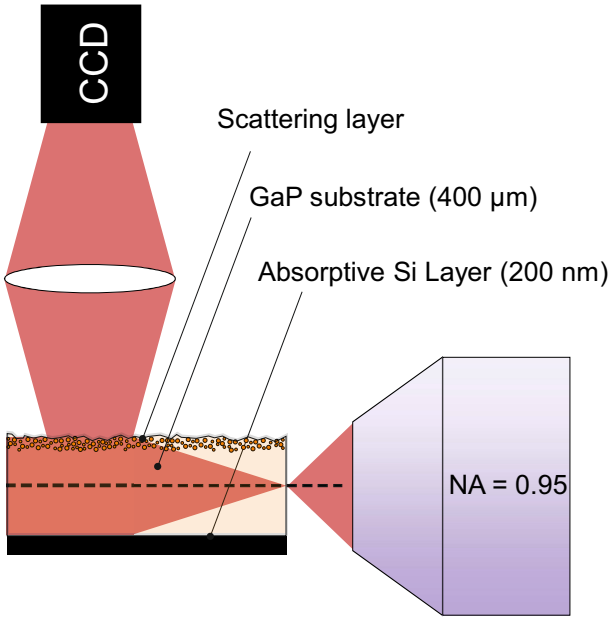

Figure 4.2: Cartoon of the experiment to measure high internal-angle scattered light. A laser beam is focused on the edge of the scattering solid immersion lens (SSIL). The scattering surface of the SSIL is imaged on a CCD camera with a lens in 2f-2f arrangement. An absorptive silicon (Si) layer on the back surface makes it sure that there is no multiple internal reflection.

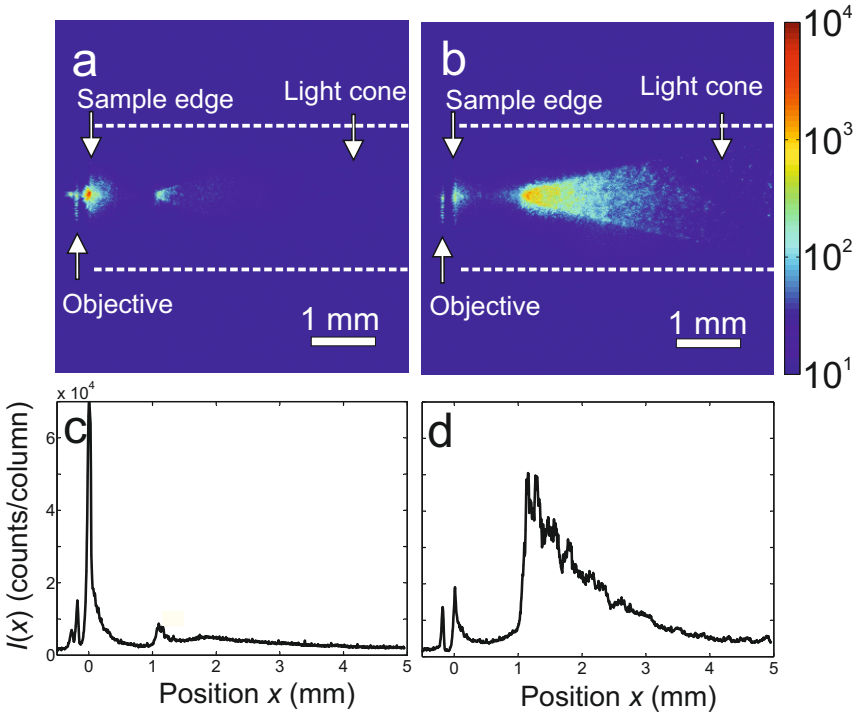

Figure 4.3: Images of the out of plane scattered light. (a) An image of the scattered light from the scattering surface of a porous GaP scattering solid immersion lens (SSIL). (b) An image of the scattered light from the scattering surface of a rough GaP SSIL. (c) Out of plane scattering intensity integrated in the transversal direction within the range that is limited by the dashed white lines (vertical axis in (a)) of a porous GaP SSIL. (d) Out of plane scattering intensity integrated in the transversal direction within the range that is limited by the dashed white lines (vertical axis in (b)) of a rough GaP SSIL. It is clear that there is more scattered light from the rough GaP SSIL compared to the porous GaP SSIL.

4.3.2 High internal-angle scattering efficiency

To compare the scattered light intensities of two different types of GaP SSILs, we define the scattering efficiency as

$$\alpha = \frac{1}{I_0}\frac{\mathrm{d}I(\cos\theta)}{\mathrm{d}(\cos\theta)}, \tag{4.1}$$

where I_0 is the total intensity of light incides on the scattering surface, $I(\cos\theta)$ the out of plane scattering intensity integrated in the transversal direction, θ is the internal-angle of incidence on the interface of the substrate and the scattering layer. We calculated $\cos\theta = \cos(\arctan(x/z))$ from the geometrical relations as seen in Fig. 4.4, where $z = 200$ µm.

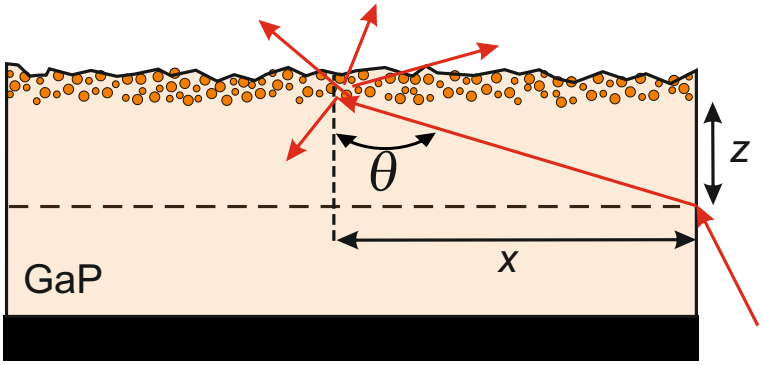

Figure 4.4: A zoom in of Fig. 4.2. A cartoon showing the internal-angle of incidence on the interface of the substrate and the scattering layer.

Figs. 4.5a and 4.5b show $I(\cos\theta)$ versus $\cos\theta$. We calculate $I(\cos\theta)$ from $I(x, y)$ as

$$I(\cos\theta) = J\sum_{y=y_\mathrm{i}}^{y_\mathrm{f}} I(x, y), \tag{4.2}$$

with the jacobian J as,

$$J = \frac{\mathrm{d}x}{\mathrm{d}(\cos\theta)} = \frac{z\cos^2\theta}{(1-\cos^2\theta)^{\frac{3}{2}}} + \frac{z}{\sqrt{1-\cos^2\theta}}, \tag{4.3}$$

and obtain the $\cos\theta$ dependent intensities. Here the summation boundaries $y = y_\mathrm{i}$ and $y = y_\mathrm{f}$ are positions in the transversal direction. For our microscope objective with NA $= 0.95$, we expect to observe the scattered light intensity for $\cos\theta \leq 0.28$. However, from our measurements we see a cut-off for $\cos\theta = 0.17$ which corresponds to an effective $\mathrm{NA}_\mathrm{eff} = 0.6$ probably due to incomplete filling of the microscope objective pupil. For a Lambertian surface, the scattering

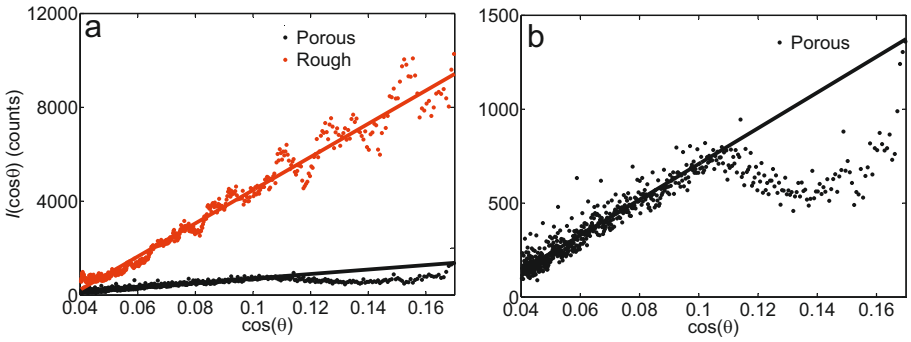

Figure 4.5: The angular dependence of the out of plane scattering intensity. (a) Out of plane scattering versus cosθ for the rough GaP SSIL and the porous GaP SSIL. The black dots represent the experimental data for the porous GaP SSIL, the red dots represent the experimental data for the rough GaP SSIL, and the curves represent the linear fitting functions. (b) A zoom in of the out of plane scattering versus cosθ for the porous GaP SSIL.

efficiency α is independent of cosθ, resulting in $I(\cos\theta) \propto \cos\theta$. In order to have a quantitative comparison of the scattering efficiencies of two different surfaces, we fit linear functions to the data for the rough GaP SSIL and the porous GaP SSIL. In Fig. 4.5a we show there is a good agreement between the linear fit and the data for the rough GaP SSIL, which suggests that even for very high internal-angles, the rough surface of an unpolished GaP wafer obeys Lambert's cosine law. In Fig. 4.5b, we show a zoom in of Fig. 4.5a for the porous GaP SSIL. For the porous GaP SSIL, we see a deviation from Lambert's cosine law between $\cos\theta = 0.1$ and $\cos\theta = 0.17$. The reason for the deviation from the Lambertian distribution may be the Fresnel-like reflections on the interfaces of the substrate, the scattering porous layer and the air [19, 21]. It is evident in Fig. 4.5a that the scattering efficiency of the rough GaP SSIL is much higher than the scattering efficiency of the porous GaP SSIL. We found a scattering efficiency ratio of $\alpha_{\text{rough}}/\alpha_{\text{porous}} = 6.8$. This result suggests that a rough GaP SSIL is even better suited for high-resolution optical imaging than the porous GaP SSIL used in experiments so far.

4.4 Angular speckle correlations of GaP scattering solid immersion lenses

Angular speckle correlations, especially the correlations known as the optical memory effect [22–25] are an important property of scattering media [26]. Imaging through scattering media based on the optical memory effect has been an active research area recent years [17, 27–32]. The optical memory effect is a first order speckle correlation effect that is observable when the momentum transfer of the incident light equals that of the transmitted light. In practice this means if

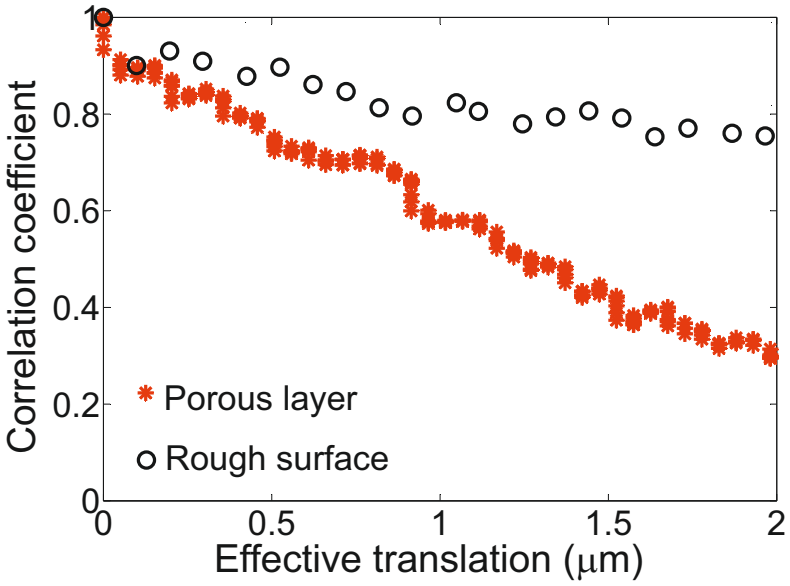

Figure 4.6: Angular speckle correlation coefficients. The black circles represent the angular speckle correlation coefficient with respect to the effective speckle pattern translation on the back surface of the rough GaP scattering solid immersion lens (SSIL). The red stars represent the angular speckle correlation coefficient with respect to the effective speckle pattern translation on the back surface of the porous GaP SSIL.

an incident light beam is tilted on a scattering medium, the transmitted speckle pattern will be translated in far-field without a significant change. Although the optical memory effect is trivial in the single scattering regime, it is surprising that such an effect exists for thick diffusive samples. However, the angular range of the optical memory effect is limited for thick layers as $\Delta\theta < \lambda/2\pi d$, where λ is the wavelength of the incident light and d the thickness of the scattering layer. In this section, we investigate the optical memory effect range of our GaP SSILs.

To observe the optical memory effect range of our SSILs we shone a laser beam with a wavelength of $\lambda = 561$ nm on the scattering surface of our porous GaP SSIL. We imaged the back surface of the SSIL on a CCD camera using a microscope objective and a tube lens. We tilted the beam on the scattering surface for a range of angles of incidence and recorded the images for each angle of incidence. We repeated the measurement for the rough GaP SSIL. We calculated the cross-correlation coefficients of each image with the first image as follows;

$$C(\delta) = \frac{\max(I_1 * I_\delta)}{\max(I_1 * I_1)}, \tag{4.4}$$

where $*$ denotes a convolution product, $C(\delta)$ the normalized correlation coefficient, I_1 the first image, and I_δ a consecutive image with an effective speckle pattern translation of δ.

In Fig. 4.6 the relation between the correlation coefficients and the effective speckle translation on the back surface of the two types of GaP SSILs are shown. It is evident that the angular speckle correlation coefficient for an unplolished rough surface is preserved for a much larger range compared to the angular speckle correlation coefficient for a porous layer. The fact that a porous GaP SSIL has already enabled a sufficient range in the previous study [17] suggests a rough GaP SSIL is even more appropriate for high-resolution optical imaging applications based on the optical memory effect.

4.5 High-resolution of the rough GaP scattering solid immersion lens

In a previous experiment, a sub-100 nm resolution image of gold nanospheres was obtained by scanning a high-resolution focus through the scattering layer of a porous GaP SSIL over gold nanospheres by using the optical memory effect [17]. In this section, we demonstrate experimentally that our rough GaP SSIL is at least equally well-suited for high-resolution optical imaging.

4.5.1 Experimental concept

In this section, we describe a scanning-focus experiment on a single gold nanosphere with a diameter of 50 nm. The wavefront of a continuous laser source (Cobolt Jive, 100 mW continuous wave at 561 nm) is spatially modulated through the scattering layer [26, 33] using a spatial light modulator (Hamamatsu X10468-04)

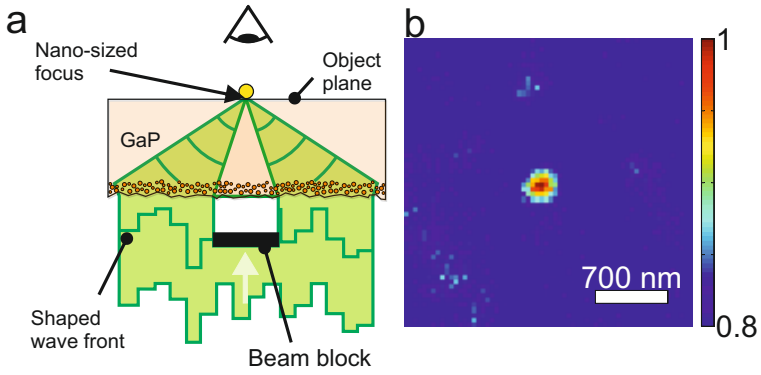

Figure 4.7: Wavefront shaping on a single gold nanosphere. (a) First, the rough GaP scattering solid immersion lens (SSIL) is illuminated by a coherent beam that is blocked in the center. The beam is focused on a gold nanosphere by wavefront shaping. (b) A dark-field image of the single gold nanosphere by averaging over many different wavefront illuminations. Fig. 4.7a is adapted from reference [20].

and focused tightly on a selected gold nanosphere on the polished surface as seen in Fig. 4.7a. The spatial light modulator is imaged onto a steering mirror. A lens and a microscope objective (Nikon: 20×, NA = 0.45) demagnify the plane of the steering mirror onto the rough surface of the GaP SSIL. The beam is 0.8 mm in size and the center is blocked by a 0.4-mm-size disk-shaped beam stop to enable dark-field microscopy. Any light that could be scattered directly into the immersion objective is blocked by the beam stop. As a result only scattered light is observed on a dark background. The polished surface of the SSIL is imaged on a CCD camera (Allied Vision Technologies Dolphin F-145B) using an oil immersion microscope objective (Nikon: 60×, NA = 1.49) and a tube lens with a focal length of 500 mm. Then, we scanned the focused beam on the gold nanosphere with steps of 14 nm using the steering mirror. For each focus position, we recorded the CCD camera images. In Fig. 4.7b, a dark-field image of the single gold nanosphere is shown with a resolution limited by the NA of the oil immersion microscope objective.

4.5.2 Results and discussion

In Fig. 4.8, a one dimensional scanning-focus image of a single gold nanosphere is shown. The black dots are calculated by taking the maximum pixel value of each recorded image for corresponding focus position on the polished surface of the SSIL. We fit an Airy disk function to the data,

$$I(r) = I_0 \left[k_{\max}^2 \frac{J_1(k_{\max} r)}{k_{\max} r} - k_{\min}^2 \frac{J_1(k_{\min} r)}{k_{\min} r} \right]^2 , \tag{4.5}$$

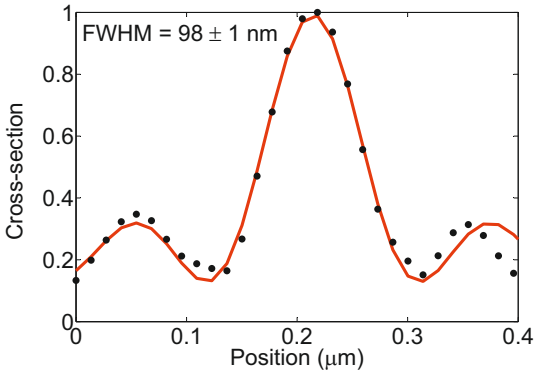

Figure 4.8: A one dimensional scanning-focus image of a single gold nanosphere. The black dots are the experimental data points, and the red curve is an Airy disk fitting function.

where J_1 is a Bessel function of the first kind, and I_0, $k_{\max}$, $k_{\min}$ are fitting parameters. The minimum and maximum transversal wave vectors, $k_{\min}$ and $k_{\max}$, are directly related to the inner and outer radius, $R_{\min}$ and $R_{\max}$, of the illuminated area: $k_{\max} = nk_0 \left(1 + L^2/R_{\max}^2\right)^{-1/2}$ (and similar for $k_{\min}$). We observed a full-width-half-maximum of 98±1 nm which is similar to the previously reported result with a porous GaP SSIL [17].

4.6 Conclusion

We presented a method to investigate high internal-angle scattering of high-NA scattering solid immersion lenses (SSILs). We have demonstrated our method on porous and rough GaP SSILs. We conclude that a rough GaP SSIL provides 6.8 times larger scattering efficiency compared to the porous GaP SSIL. We have measured the range of the optical memory effect for both porous and rough GaP SSILs. We have found that a rough scattering GaP lens has a much larger optical memory effect range compared to a porous GaP SSIL. Finally, we presented a 1-D scanning-focus experiment result on a single gold nanosphere. We observed a full-width-half maximum of 98 ± 1 nm for a 1-D scanning-focus image of the gold nanosphere. Our results imply that a rough GaP SSIL is appropriate for high-resolution optical imaging. A rough GaP SSIL has the advantages of more signal and wider optical memory effect range compared to a porous GaP SSIL which is especially important if one aims to enhance the resolution even further. Single side polished GaP wafers are commercially available, therefore fabrication of a rough GaP SSIL is much simpler since it does not require an additional electrochemical etching step. Scattering lenses are robust against environmental instabilities such as mechanical or thermal fluctuations. Therefore, a rough GaP SSIL is well suited for high-resolution optical imaging applications with visible light under ambient conditions.

Bibliography

[1] S. M. Mansfield, W. R. Studenmund, G. S. Kino, and K. Osato, *High-numerical-aperture lens system for optical storage*, Opt. Lett. **18**, 305 (1993). — p.51.

[2] I. Ichimura, S. Hayashi, and G. S. Kino, *High-density optical recording using a solid immersion lens*, Appl. Opt. **36**, 4339 (1997). — p.51.

[3] K. Koyama, M. Yoshita, M. Baba, T. Suemoto, and H. Akiyama, *High collection efficiency in fluorescence microscopy with a solid immersion lens*, Appl. Phys. Lett. **75**, 1667 (1999). — p.51.

[4] L. P. Ghislain and V. B. Elings, *Near-field scanning solid immersion microscope*, Appl. Phys. Lett. **72**, 2779 (1998). — p.51, 105, 111.

[5] L. P. Ghislain, V. B. . Elings, K. B. Crozier, S. R. Manalis, S. C. Minne, K. Wilder, G. S. Kino, and C. F. Quate, *Near-field photolithography with a solid immersion lens*, Appl. Phys. Lett. **74**, 501 (1999). — p.51.

[6] E. Ramsay, N. Pleynet, D. Xiao, R. J. Warburton, and D. T. Reid, *Two-photon optical-beam-induced current solid-immersion imaging of a silicon flip chip with a resolution of 325 nm*, Opt. Lett. **30**, 26 (2005). — p.51, 105, 111.

[7] B. B. Goldberg, A. Yurt, Y. Lu, E. Ramsay, F. H. Köklü, J. Mertz, T. Bifano, and M. S. Ünlü, *Chromatic and spherical aberration correction for silicon aplanatic solid immersion lens for fault isolation and photon emission microscopy of integrated circuits*, Microelectron. Reliab. **51**, 1637 (2011). — p.51, 105, 111.

[8] K. Vigil, Y. Lu, A. Yurt, T. B. Cilingiroglu, T. Bifano, M. S. Ünlü, and B. B. Goldberg, *Integrated circuit super-resolution failure analysis with solid immersion lenses*, Electronic Device Failure Analysis **16**, 26 (2014). — p.51, 105, 111.

[9] S. M. Mansfield and G. S. Kino, *Solid immersion microscope*, Appl. Phys. Lett. **57**, 2615 (1990). — p.9, 51, 105, 111.

[10] Q. Wu, G. D. Feke, R. D. Grober, and L. P. Ghislain, *Realization of numerical aperture 2.0 using a gallium phosphide solid immersion lens*, Appl. Phys. Lett. **75**, 4064 (1999). — p.51, 105, 111.

[11] M. Baba, T. Sasaki, M. Yoshita, and H. Akiyama, *Aberrations and allowances for errors in a hemisphere solid immersion lens for submicron-resolution photoluminescence microscopy*, J. Appl. Phys. **85**, 6923 (1999). — p.51.

[12] Y. Zhang, *Multiple reflection effect inside a hemispherical solid immersion lens*, Opt. Commun. **266**, 94 (2006). — p.51.

[13] R. Brunner, M. Burkhardt, A. Pesch, and O. Sandfuchs, *Diffraction-based solid immersion lens*, J. Opt. Soc. Am. A **21**, 1186 (2004). — p.52.

[14] F. Zernike, *The concept of degree of coherence and its application to optical problems*, Physica **5**, 785 (1938). — p.20, 52.

[15] I. M. Vellekoop, A. Lagendijk, and A. P. Mosk, *Exploiting disorder for perfect focusing*, Nature Photon. **4**, 320 (2010). — p.52, 68.

[16] H. Yılmaz, *Advanced optical imaging with scattering lenses, Chapter 3*, Ph.D. thesis, University of Twente, 2015. — p.52.

[17] E. G. van Putten, D. Akbulut, J. Bertolotti, W. L. Vos, A. Lagendijk, and A. P. Mosk, *Scattering lens resolves sub-100 nm structures with visible light*, Phys. Rev. Lett. **106**, 193905 (2011). — p.27, 52, 54, 58, 60, 62, 68, 69, 75, 76, 78, 92, 105, 111.

[18] F. J. P. Schuurmans, D. Vanmaekelbergh, J. van de Lagemaat, and A. Lagendijk, *Strongly photonic macroporous gallium phosphide networks*, Science **284**, 141 (1999). — p.52, 54, 76.

[19] B. Bret, *Multiple light scattering in porous gallium phosphide*, Ph.D. thesis, University of Twente, 2005. — p.52, 54, 58.

[20] E. G. van Putten, *Disorder-enhanced imaging with spatially controlled light*, Ph.D. thesis, University of Twente, 2011. — p.28, 29, 53, 61.

[21] J. X. Zhu, D. J. Pine, and D. A. Weitz, *Internal reflection of diffusive light in random media*, Phys. Rev. A **44**, 3948 (1991). — p.54, 58.

[22] S. Feng, C. Kane, P. A. Lee, and A. D. Stone, *Correlations and fluctuations of coherent wave transmission through disordered media*, Phys. Rev. Lett. **61**, 834 (1988). — p.27, 58, 69, 97, 106, 112.

[23] I. Freund, M. Rosenbluh, and S. Feng, *Memory effects in propagation of optical waves through disordered media*, Phys. Rev. Lett. **61**, 2328 (1988). — p.27, 58, 69, 97, 106, 112.

[24] X. Yang, C. L. Hsieh, Y. Pu, and D. Psaltis, *Three-dimensional scanning microscopy through thin turbid media*, Opt. Express **20**, 2500 (2012). — p.27, 58.

[25] B. Judkewitz, R. Horstmeyer, I. M. Vellekoop, and C. Yang, *Translation correlations in anisotropically scattering media*, arXiv:1411.7157 (2014). — p.27, 58.

[26] A. P. Mosk, A. Lagendijk, G. Lerosey, and M. Fink, *Controlling waves in space and time for imaging and focusing in complex media*, Nature Photon. **6**, 283 (2012). — p.10, 37, 58, 60.

[27] C. L. Hsieh, Y. Pu, R. Grange, G. Laporte, and D. Psaltis, *Imaging through turbid layers by scanning the phase conjugated second harmonic radiation from a nanoparticle*, Opt. Express **18**, 20723 (2010). — p.27, 58, 69, 76.

[28] I. M. Vellekoop and C. Aegerter, *Scattered light fluorescence microscopy: Imaging through turbid layers*, Opt. Lett. **35**, 1245 (2010). — p.27, 58, 69.

[29] O. Katz, E. Small, and Y. Silberberg, *Looking around corners and through thin turbid layers in real time with scattered incoherent light*, Nature Photon. **6**, 549 (2012). — p.27, 58, 69.

[30] J. Bertolotti, E. G. van Putten, C. Blum, A. Lagendijk, W. L. Vos, and A. P. Mosk, *Non-invasive imaging through opaque scattering layers*, Nature **491**, 232 (2012). — p.27, 28, 29, 38, 58, 69, 72, 99, 106, 112.

[31] C. Ma, X. Xu, Y. Liu, and L. V. Wang, *Time-reversed adapted-perturbation (TRAP) optical focusing onto dynamic objects inside scattering media*, Nature Photon. **8**, 931 (2014). — p.58.

[32] K. T. Takasaki and J. W. Fleischer, *Phase-space measurement for depth-resolved memory-effect imaging*, Opt. Express **22**, 31426 (2015). — p.27, 29, 58.

[33] I. M. Vellekoop and A. P. Mosk, *Focusing coherent light through opaque strongly scattering media*, Opt. Lett. **32**, 2309 (2007). — p.10, 12, 27, 60.

CHAPTER 5

Speckle correlation resolution enhancement of wide-field fluorescence imaging

High-resolution fluorescence imaging is essential in nanoscience and biological sciences. Due to the diffraction-limit, conventional imaging systems can only resolve structures larger than 200 nm. Here, we introduce a new fluorescence imaging method that enhances the resolution by using a high-index scattering medium as an imaging lens. Simultaneously, we achieved a wide field-of-view. We developed a new image reconstruction algorithm that converges even for complex object structures. We collect two-dimensional fluorescence images of a collection of 100-nm diameter dye-doped nanospheres. We demonstrate a deconvolved Abbe resolution of 116 nm with a field-of-view of 10 µm × 10 µm. Our method is robust against optical aberrations and stage drifts; thereby it is well suited to image nanostructures with high-resolution under ambient conditions.

5.1 Introduction

A conventional optical microscope produces images with a resolution determined by the numerical aperture (NA) of the imaging lens [1]. The NA of an imaging lens is defined by the highest wave vector that is accessible in the transversal direction. Many methods have been introduced that enable optical resolution beyond the resolution limit of a conventional optical microscope, by exploiting evanescent waves with near-field scanning optical microscopy (NSOM) [2], by exploiting moiré fringes as in structured-illumination microscopy (SIM) [3, 4] or blind structured-illumination microscopy (blind-SIM) [5], by exploiting nonlinear optical phenomena as in saturated structured-illumination microscopy (SSIM) [6] or stimulation emission depletion (STED) microscopy [7, 8], by exploiting specific photophysical properties of dyes as in stochastic optical reconstruction microscopy (STORM) [9], photoactivated localization microscopy (PALM) [10], or super-resolution optical fluctuation imaging (SOFI) [11]. Nevertheless, NSOM has a field-of-view limited by the scan range of the probe, moreover a scanning

This chapter has been published as: H. Yılmaz, E. G. van Putten, J. Bertolotti, A. Lagendijk, W. L. Vos, and A. P. Mosk, Optica **2**, 424-429 (2015).

probe usually greatly affects the measurement itself. SIM provides a resolution that is potentially two times higher than a conventional optical microscope [3, 4]. SIM requires a precise knowledge of the illuminating intensity patterns on the structure of interest. Recently, a *blind-SIM* method [5] has been demonstrated which exploits the statistical properties of speckle patterns and does not require precise knowledge of the illuminating intensity patterns. Since STED requires intense laser pulses, it is a question how to use it for delicate samples with a low damage threshold. STED, STORM, PALM, and SOFI require dyes with specific photo-physical properties. Although aforementioned far-field microscopy methods realize an optical resolution beyond the diffraction-limit, the resolution remains strongly dependent on the NA of their conventional optics.

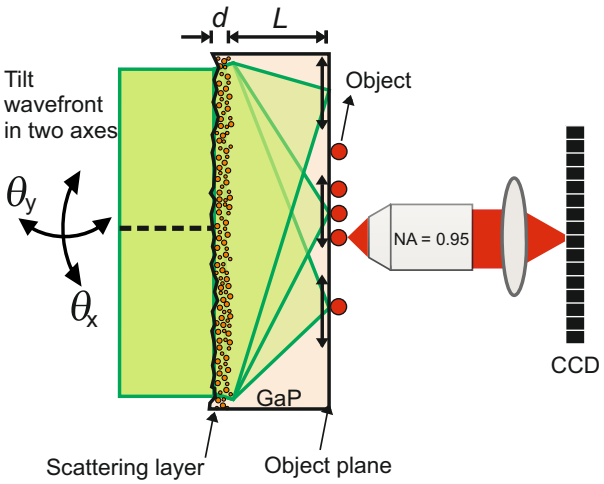

Figure 5.1: The concept of the wide-field, high-resolution speckle scanning microscopy. A beam of coherent light illuminates a scattering layer on a gallium phosphide (GaP) substrate. The scattered light generates a speckle pattern that enables high-resolution imaging on the object plane. The incident beam is tilted by angles θ_x and θ_y, and as a result the speckle pattern is scanned across the sample. Fluorescent nanospheres on the object plane are imaged on a CCD camera. With parallel speckle detection, the field of view is wider than the single speckle-scan range. d denotes the thickness of the scattering layer; L denotes the thickness of the substrate.

It has been shown that a scattering medium enhances spatial resolution for acoustic waves [12], microwaves [13], and light waves [14, 15], and turns a high-index substrate into a high-NA solid immersion lens by breaking the translational invariance on the interface of the substrate [16]. Coherent light illumination on such a scattering medium generates a speckle pattern of apparently randomly distributed bright and dark regions behind the scattering medium. Correlations of speckle patterns are used to obtain images of astronomical objects through turbulent atmosphere with diffraction-limited resolution [17, 18]. The concept of exploiting correlations between such speckle patterns to obtain images of micro-

scopic objects has started a new class of optical microscopy [19]. Within a speckle pattern there is a correlation effect called the optical memory effect [20, 21] that has recently been exploited for optical imaging using a high-NA scattering lens [16] and through scattering media [22–28]. A tilt of the incident beam within an angle of $\Delta\theta < \lambda/2\pi d$ (λ is the wavelength of light and d the thickness of the scattering medium) results in a translation of the speckle pattern behind the medium without a significant change in the pattern. The optical memory effect has been employed to obtain optical images of microscopic objects hidden by a scattering medium with diffraction-limited resolution [26–28]. Previously, a high-NA gallium phosphide (GaP) scattering lens has been used to image gold nanoparticles with elastically scattered coherent visible light [16]. However, the available field-of-view with speckle correlations is limited to 2 µm × 2 µm due to the finite range of the optical memory effect, and the high-index scattering lens has so far not been applied to incoherent imaging modalities such as fluorescence microscopy.

Here we introduce and demonstrate speckle correlation resolution enhancement (SCORE) microscopy that combines the high-resolution of speckle scanning microscopy with a wide field-of-view of parallel speckle-scan detection. Fig. 5.1 shows the concept of our method. The main element of the experiment is a scattering lens, consisting of a GaP substrate with a thickness of $L = 400$ µm and a refractive index of $n = 3.42$ of which one surface has a scattering layer with a thickness of $d = 2$ µm and one surface is polished [16]. The polished surface is coated with silicon (Si) with a thickness of 100 nm to reduce internal reflections (see appendix). The Si coating is removed in a 10-µm-scale window to place objects directly on the polished GaP surface. A beam of coherent light with a diameter of 0.8 mm and a wavelength of $\lambda_{\mathrm{ill}} = 561$ nm is incident onto the scattering surface of the substrate. The scattering layer generates a speckled intensity pattern $S(x, y)$ that illuminates a fluorescent object $O(x, y)$. The fluorescence intensity distribution on the object plane is imaged on a camera with a resolution of $R = \lambda_{\mathrm{flu}}/(2\mathrm{NA})$, with $\lambda_{\mathrm{flu}} = 612$ nm and NA = 0.95. We raster scan the speckle pattern on the object plane by tilting the incident beam by angles $\delta\theta_{\mathrm{x}}$ and $\delta\theta_{\mathrm{y}}$, within the angular range of the optical memory effect ($\Delta\theta \approx 1\,^{\circ}$) that leads to a speckle-scan range of 2 µm on the object plane. We record fluorescence images at every $\delta\theta_{\mathrm{x}}$, $\delta\theta_{\mathrm{y}}$ for a range of angles of incidence, resulting in perpendicular speckle pattern displacements $\delta x \approx \delta\theta_{\mathrm{x}}\ L/n$ and $\delta y \approx \delta\theta_{\mathrm{y}}\ L/n$ in the object plane. This procedure results in a four-dimensional data-cube $I(x, y, \delta x, \delta y)$, which contains sufficient information to reconstruct a wide-field image that has a resolution of the average speckle grain size [26].

5.2 High-resolution spatial information retrieval

In Fig. 5.2 we show the data analysis procedure. We divide the data-cube (Fig. 5.2a) into N sub-data cubes by applying N square window functions of $W_m(x, y)$ with a 96% overlap that each have a width and a height equal to half of the speckle-scan range (1 µm) that each can be processed in parallel. We construct

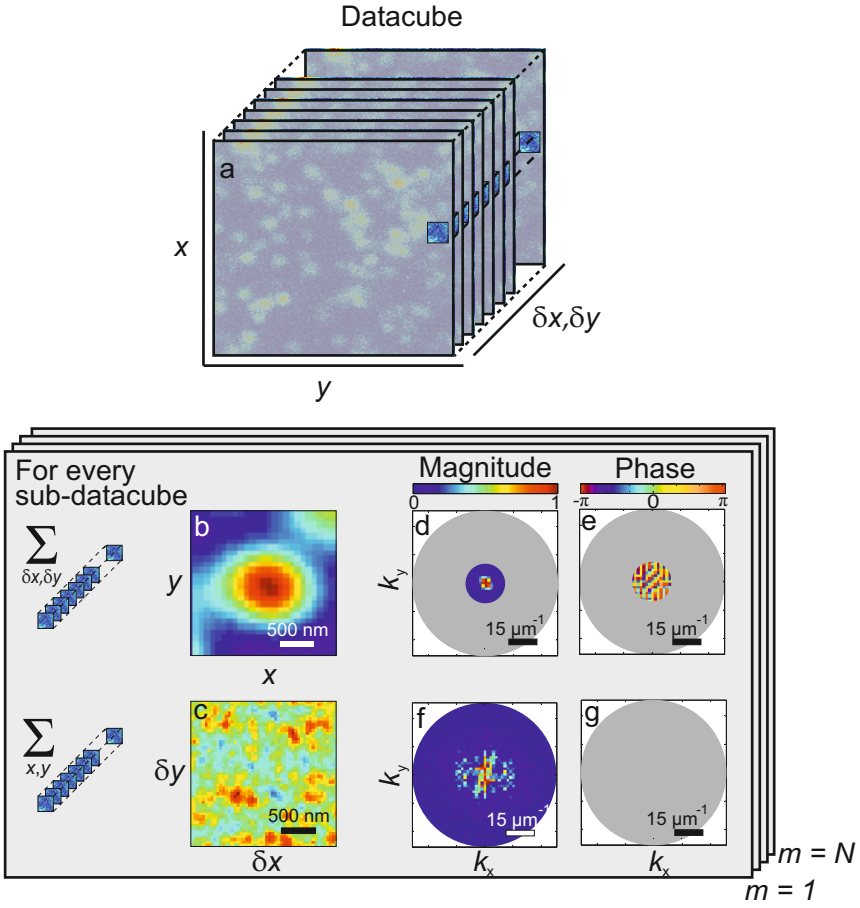

Figure 5.2: The data analysis procedure on a single sub-data cube. (a) Data-cube $I(x, y, \delta x, \delta y)$. (b) The obtained standard resolution sub-image $J_m(x, y)$ by summing the sub-data cube shown by the square non-grayed out area over δx and δy. (c) The obtained speckle-scan matrix $K_m(\delta x, \delta y)$ by summing the sub-data cube shown by the square non-greyed out area over x and y. (d) The magnitude of the Fourier components of $J_m(x, y)$. (e) The phase of the Fourier components of $J_m(x, y)$. (f) The magnitude of the Fourier components of $K_m(\delta x, \delta y)$. (g) The phase of the Fourier components of $K_m(\delta x, \delta y)$.

a standard resolution sub-image $J_m(x, y)$ (Fig. 5.2b) and a speckle-scan matrix $K_m(\delta x, \delta y)$ (Fig. 5.2c) from the corresponding sub-data cube as follows: We sum our sub-data cube over δx and δy, and obtain the standard resolution sub-image $J_m(x, y)$. In our approach, it is useful to represent $J_m(x, y)$ in the Fourier domain, where its spatial information is given by the magnitude and the phase of the Fourier components (Fig. 5.2d,e). To obtain the speckle-scan matrix $K_m(\delta x, \delta y)$, we calculate the following summation

$$\begin{aligned} K_m(\delta x, \delta y) &= \sum_{x,y} I(x, y, \delta x, \delta y) W_m(x, y) \\ &= \sum_{x,y} O(x, y) S(x - \delta x, y - \delta y) W_m(x, y) \\ &= [(O \cdot W_m) * S](\delta x, \delta y), \end{aligned} \tag{5.1}$$

where the symbol $*$ denotes a convolution product and where in the last step we assumed that the scan range stays within the optical memory effect range. In Figs. 5.2f and 5.2g we represent the speckle-scan matrix $K_m(\delta x, \delta y)$ in the Fourier domain. We obtain the magnitude of the high-frequency Fourier components of the object from its speckle-scan matrix as follows:

$$\begin{aligned} |\mathcal{F}\{K_m\}| &= |\mathcal{F}\{O \cdot W_m\}| \cdot |\mathcal{F}\{S\}| \\ &= C|\mathcal{F}\{O \cdot W_m\}| \end{aligned} \tag{5.2}$$

where $C = |\mathcal{F}\{S\}|$ is the optical transfer function of the GaP scattering lens, and $\mathcal{F}\{\}$ denotes a Fourier transform. Here we use the approximation that within the NA of the GaP scattering lens, the absolute value of the spatial spectrum of the field is constant for a fully developed speckle pattern [29], therefore the magnitude of the spatial spectrum of S will be approximately a cone-shaped function in the Fourier domain with a cut-off at the highest Fourier component of the GaP scattering lens [30]. Equation 5.2 shows that the magnitude of the high-frequency Fourier components of the object is retained behind the scattering layer (Fig. 5.2f). The phase information of the object's Fourier components is lost due to the random and unknown phase of the speckle pattern (Fig. 5.2g). Fortunately, it is often possible to infer the lost phase information using an iterative phase retrieval algorithm [31–34]. In essence, our approach relies on reducing the light scattering problem to a phase retrieval problem.

5.3 Image reconstruction

We have developed a new Gerchberg-Saxton-type algorithm that uniquely retrieves the high-frequency phase information of the Fourier components of our object by using the low-frequency phase information of the Fourier components of the object as a new constraint (see appendix). In general, a Gerchberg-Saxton-type algorithm retrieves the phase of the Fourier components of an image from the magnitude of the Fourier components by using some constraints on the im-

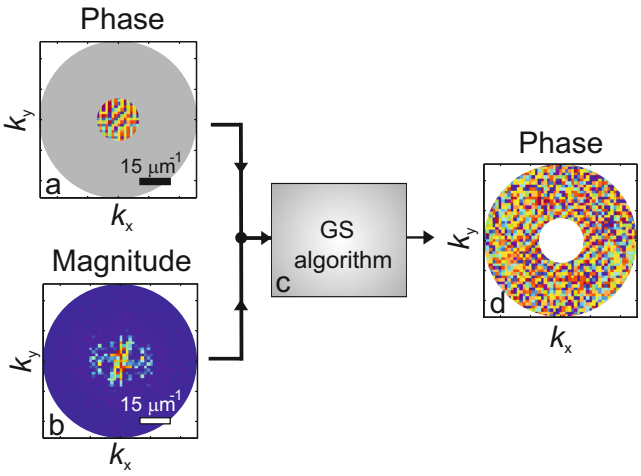

Figure 5.3: Phase retrieval in the Fourier domain. (a) The phase of the Fourier components of the object. (b) The magnitude of the Fourier components of the object. (c) The Gerchberg-Saxton-type algorithm. (d) The retrieved phase of high-frequency Fourier components of the object. (The phase data comes from Fig. 5.2e and the magnitude data comes from Fig. 5.2f. Colourbars are as in Fig. 5.2).

age or the Fourier domain. Using only the magnitude of the Fourier components gives rise to ambiguities that lead to stagnation problems in the reconstruction [33, 35]. In ptychography and Fourier ptychography, such ambiguities are discarded by overlapping many wide-field images [36–39]. However, both ptychography and Fourier ptychography algorithms work only for diffractive objects. For non-diffractive objects such as fluorescent objects, these ambiguities are absent since the object is represented with real and positive numbers and the object can be determined up to a trivial flip and translation [26–28]. In our Gerchberg-Saxton-type algorithm, we employ constraints both in the image domain and in the Fourier domain to discard even trivial flip and translation ambiguities. In the image domain we use the well-known information that the measured intensity of our fluorescent object is real and positive. In the Fourier domain, we introduce as a new feature the phase of the low-frequency Fourier components. Combining these two types of information the algorithm converges to a unique solution which gives us the shape, the position and the orientation of the object. This is a major improvement over previous approaches [26–28] that do not provide position and orientation information. We analyzed the convergence probability of our algorithm on a complex test object composed of six letters of the Latin alphabet (see appendix). We found that when the detection NA ($\mathrm{NA_{det}}$) is higher than 13% of the illumination NA ($\mathrm{NA_{ill}}$), our algorithm always converges to a unique solution. If the $\mathrm{NA_{det}}$ is lower than the 13% of the $\mathrm{NA_{ill}}$, the convergence probability drops. For our experimental situation the $\mathrm{NA_{det}}$ is always larger than

30% of the NA_{ill} and convergence is fast. The low rate of convergence at very low NA_{det}/NA_{ill} can almost certainly be considerably improved by implementing anti-stagnation mechanisms [40]. However even without these mechanisms, we obtain a sufficient convergence rate for our experimental situation.

In Fig. 5.6 the phase retrieval procedure of high-frequency Fourier components is shown for a single sub-data cube. First, we Fourier transform both a standard resolution sub-image, $J_m(x, y)$ and the corresponding speckle-scan matrix, $K_m(\delta x, \delta y)$. We discard the magnitude of the Fourier components of $J_m(x, y)$ and the phase of the Fourier components of $K_m(\delta x, \delta y)$. We input the phase information of low-frequency Fourier components of $J_m(x, y)$ and the magnitude information of high-frequency Fourier components of $K_m(\delta x, \delta y)$ into our Gerchberg-Saxton-type algorithm. The algorithm outputs the phase information of high-frequency Fourier components. Finally, we combine and inverse Fourier transform all available phase and magnitude information of the Fourier components to obtain the high-resolution sub-image. Our algorithm has some conceptual similarity with pattern-illuminated Fourier ptychography [41]. In pattern-illuminated Fourier ptychography, the wide-field images are overlapped in the Fourier domain, whereas we select a sub-area in the x, y plane and project the corresponding sub-data cube on the k_x, k_y plane. We then use phase retrieval to obtain the corresponding high-resolution sub-image. Our method has the advantage of robustness against the drifts compared to pattern-illuminated Fourier ptychography. Our method works as long as the drifts are small compared to the optical memory effect range, whereas pattern-illuminated Fourier ptychography and related methods [5] have much more stringent requirements and only converges for the drifts smaller than the speckle grain size.

To acquire a wide-field image, we apply our phase retrieval procedure shown in Fig. 5.6 to every sub-data cube (see Fig. 5.2) in parallel. We have approximately N sub-data cubes for a wide-field image with N pixels that corresponds to a 96% overlap of each neighboring sub-data cube. Each reconstructed overlapping high-resolution sub-image is windowed by a smooth window function to minimize edge effects. The detailed shape of the window has little to no effect in the reconstruction, as long as it is soft-edged and thus does not introduce artefacts. We tile the reconstructed high-resolution sub-images to yield a wide-field image of the complete object. The field-of-view of the reconstructed image is wider than the speckle-scan range and spans the field-of-view of the detection optics. Using the optical transfer function of our scattering lens, we inverse apodized the wide-field SCORE image. In order to have a fair comparison, we also inverse apodized wide-field conventional image with the known optical transfer function of the detection objective (see appendix).

5.4 Results and Discussion

To experimentally test our new imaging method we use a collection of fluorescent nanospheres with a diameter of 100 nm as test objects. Fig. 5.4a shows an image of a collection of many fluorescent nanospheres taken with conventional high-NA

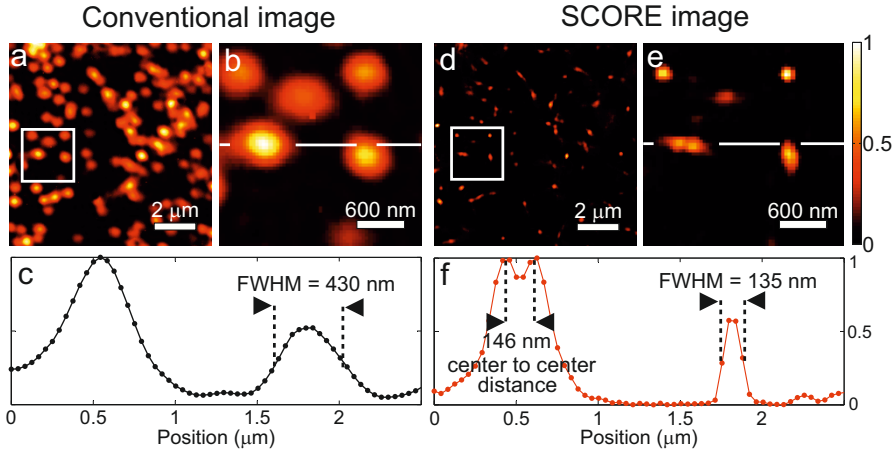

Figure 5.4: Wide-field images of fluorescent nanospheres with diameter of 100 nm. (a) The wide-field image by conventional microscopy. (b) A zoomed image of (a). (c) A cross section of (b) represented by the white line. (d) The wide-field image by SCORE microscopy. (e) A zoomed image of (d). (f) A cross section of (e) represented by the white line. In (c), a single nanosphere is apparent while in (f) two smaller nanospheres are apparent with a center to center distance of 146 nm from each other.

microscopy in a field-of-view of 10 µm × 10 µm. The zoom-in in Fig. 5.4b reveals five separate nanospheres. Fig. 5.4c shows a cross-section of two nanospheres from Fig. 5.4b that have a full-width-half-maximum of about 430 nm. We now turn to the high-resolution SCORE results. Fig. 5.4d shows the same area as in Fig. 5.4a. In Fig. 5.4d the nanospheres are sharper compared to the image in Fig. 5.4a. The zoom-in in Fig. 5.4e shows the same area as in Fig. 5.4b: We see that the nanospheres are much sharper compared to Fig. 5.4b and we see six separate nanospheres, whereas less nanospheres were discernible in Fig. 5.4b. Notably at the left center two nanospheres are distinguished that were observed as one blob on Fig. 5.4b. Fig. 5.4f shows a cross-section of three nanospheres from Fig. 5.4e that have a full-width-half-maximum of about 135 nm. A clear demonstration of the enhanced resolution is given in Fig. 5.4f where we clearly resolve two nanospheres with a center to center distance of 146 nm, and an edge to edge distance of 46 nm. The fact that two 100-nm spheres with a center-to-center distance of 146 nm are clearly resolved suggests that the effective resolution of our current system (according to Sparrow's criterion) must be well below 146 nm [42]. In our SCORE images nanospheres appear as features with a full-width-half-maximum of 135 nm. As the features in the SCORE image are the convolution of the object and the point spread function (PSF), we estimate the effective full-width-half-maximum of the PSF for the image feature as $\Delta_{\mathrm{PSF}} = (\Delta^2_{\mathrm{feature}} - \Delta^2_{\mathrm{object}})^{1/2} = 116$ nm (see appendix). A resolution of 116 nm agrees very well with the expected diffraction-limited resolution from the geometry of

our scattering lens. Our results demonstrate that speckle correlations enhance the resolution of an optical microscope without any restriction on its field-of-view. In essence, SCORE with the combination of a GaP scattering lens is a high-resolution total internal reflection fluorescence (TIRF) microscope. The demonstrated resolution of 116 nm can be achieved as long as the object of interest is very close to the substrate of the GaP scattering lens (see appendix).

Previously, a speckle imaging method has been reported where a high-resolution image is retrieved from a set of low-resolution images [14]. However, a measurement of the high-resolution speckle pattern is required as *a priori* information. A high-NA scattering lens could only be used in abovementioned method with a very challenging pre-calibration using NSOM [43]. In cases when a very high-resolution speckle pattern is desired, a high-NA scattering lens is inevitable [16]. It is interesting to compare the performance of SCORE to blind-SIM [5] which has conceptual similarities. An information-theoretical analysis shows that the two methods perform differently for different NA ratios. For NA ratio of $\mathrm{NA_{ill}}/\mathrm{NA_{det}} \approx 1$, blind-SIM offers a higher resolution and a better signal-to-noise ratio (SNR). At the high NA ratio of our experiment, blind-SIM is not able to provide useful SNR, whereas SCORE can work with acceptable SNR up to very high NA ratios (see appendix).

5.5 Methods

Speckle-scan matrices contain high-resolution information of imaging object. In order to measure a speckle-scan matrix $K_m(x, y, \delta x, \delta y)$, the speckle pattern has to stay correlated over the resolution $\delta r = \lambda_{\mathrm{flu}}/(2\mathrm{NA})$. This constraint is met when $\delta r < \lambda_{\mathrm{ill}} L/(2\pi n d)$ where n is the refractive index of the GaP substrate, L the thickness of the GaP substrate, λ_{ill} the wavelength of the incident light on the GaP porous layer, and d the thickness of the GaP porous layer. In our GaP substrate $\lambda_{\mathrm{ill}} L/(2\pi n d)$ is in the order of 2 µm. Our detection optics has a resolution ($\delta r = 322$ nm) that is high enough to fulfill this condition. The average speckle grain size of a GaP scattering lens is $\delta S = \lambda_{\mathrm{ill}}/[2n\sin(\tan^{-1}(W/2L))]$, where W is the beam width. In our case, an average speckle grain size is $\delta S = 116$ nm. We scan the speckle pattern with steps of 40 nm over a range of 2 µm in two dimensions, requiring $N = 2500$ measurements. For each measurement the full camera image is stored, which allows us to retrieve the object at any position of the captured field-of-view. The data acquisition takes about 1 hour. The time scale of the data acquisition is independent of the field-of-view, while it follows a square law with respect to the targeted resolution. However 1 hour is not a fundamental limit. The data acquisition time can be reduced by an order of magnitude by using a more sensitive camera.

5.6 Conclusion

In summary, we experimentally demonstrate a new method to obtain high-resolution and wide-field fluorescence images. In combination with a gallium

phosphide scattering lens, speckle correlation resolution enhancement (SCORE) has the ability to acquire very high-resolution images with a field-of-view that is much wider than the speckle-scan range. The preparation of a GaP scattering lens is easy and versatile by a standard method [44]. SCORE is thus excellently suited to be used for imaging of two-dimensional objects as large as a few hundred micrometers with subcellular resolution. *A priori* characterization of the scattering lens by methods such as wavefront shaping [16], digital optical phase conjugation [22] or transmission matrix measurement [45, 46] is not needed. If one uses the information of both the detection and the illumination NA as in structured illumination microscopy and pattern-illuminated Fourier ptychography, our method has a higher potential resolution than presented here. Using only the illumination NA of our microscope we have the advantage of robustness on ambient conditions such as optical aberrations and mechanical drifts. Even using only the illumination NA, our method provides a remarkable resolution under ambient conditions. With a setup optimized for stability, our analysis method can be modified to improve the resolution even further. Our method can provide resolution enhancement in various scenarios where collecting low-resolution wide-field images is possible. In case one can take pictures using a camera with a low-NA objective and wants pictures with higher resolution than the objective can achieve, the scattering environment can be used as a high-NA lens with our method as follows: The object of interest can be illuminated by low-intensity laser light that generates speckle pattern reflected from a wall. The generated speckle pattern on the object can be translated by the optical memory effect. Taking several low-resolution pictures for a scanning-range in the order of the resolution of the low-NA camera objective is sufficient to reconstruct high-resolution images with the wide field-of-view of the camera objective.

5.A Details of experiment and data analysis

In this appendix, we describe the details of our experimental and data analysis methods. We describe the sample preparation and the experimental set-up. We describe the new phase retrieval algorithm, convergence properties of the algorithm, and the inverse apodization procedure that we have developed. We describe the effective object size and the effective scattering lens NA estimation that yields the resolution of our experimental results. In the last section, we describe and present the information-theoretical analysis of our method and compare it to a similar method.

5.A.1 Sample and experimental setup

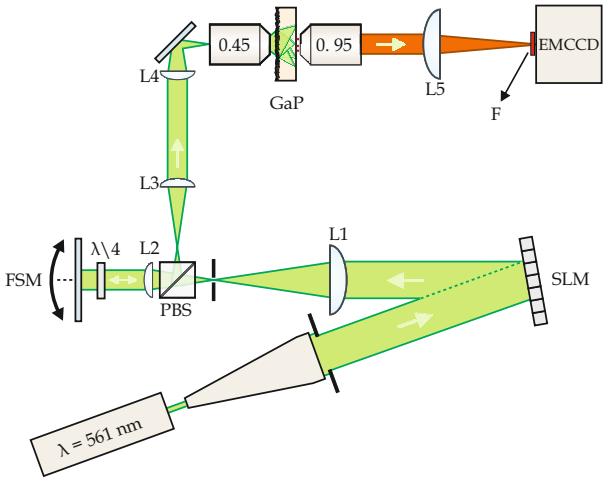

Figure 5.5: Experimental setup: An expanded CW laser at 561 nm illuminates a spatial light modulator (SLM). The beam size on the SLM is 0.8 cm. The 0th order diffracted beam is imaged on a two-axis steering mirror. The 90° polarized beam is reflected from a polarizing beam splitter (PBS) is imaged on the scattering surface of the GaP wafer. The fluorescence from nanoparticles on the back side of the GaP wafer is imaged on an EMCCD camera. $\lambda/4$ is a quarter wave plate, and L1, L2, L3, L4, L5, lenses with a focal distance of 200 mm, 100 mm, 100 mm, 50 mm, and 500 mm, respectively.

We prepared a GaP scattering lens containing a low density of dye doped fluorescent nanospheres in the object plane. A porous layer with a thickness of 2 µm is prepared by electrochemical etching. The polished side of the GaP substrate is coated with 100 nm silicon (Si) layer by chemical vapor deposition to minimize internal reflections in the GaP lens that reduce the effective range of the optical memory effect. Dye-doped polystyrene nanospheres are drop-casted

on a 10-µm-scale window of the Si coating side. Nanospheres have a diameter of 100 nm and have their absorption peak at 542 nm and emission peak at 612 nm.

The details of the experimental setup is shown in Fig. 5.5. The light source is a diode pumped solid state laser (Cobolt Jive, 100 mW continuous wave at 561 nm). We use a phase only spatial light modulator (Hamamatsu X10468-04) in the illumination path to generate a parabolic phase correction required for a proper displacement of the scattered light inside the GaP scattering lens [16]. The spatial light modulator is imaged onto a two-axis steering mirror and another lens and a microscope objective (Nikon: 20×, NA = 0.45) then demagnify the plane of the two-axis mirror onto the porous surface of the GaP substrate. An air microscope objective (Zeiss: Infinity corrected, 63×, NA = 0.95) images the object plane of the GaP substrate onto an EMCCD camera (Andor Luca DL-658M). Multiple band-pass filters (Semrock FF01-620/52-25) in front of the camera ensure that only the fluorescence light is detected.

5.A.2 The Gerchberg-Saxton-type algorithm

We have developed a Gerchberg-Saxton-type (GS) algorithm for phase retrieval. Our Gerchberg-Saxton-type algorithm is shown by a block diagram in Fig. 5.6. We use the following procedure to retrieve the phase information of high-frequency Fourier components. As an initial guess, we use the standard resolution sub-image. The "Hybrid Input-Output" [32] algorithm is employed for β ranging from 2 to 0 in steps of 0.1. For each value of β the algorithm runs 10 iterations. Finally, 100 iterations with the "Error-Reduction" [32] algorithm are used to obtain convergence with a minimal error. In each iteration, we apply a high-pass filter to the retrieved phase and combine it with the low-pass filtered phase of the standard resolution sub-image. Low spatial frequency phase information of the standard resolution image eliminates ambiguities such as flips and translations of the object and satisfies a unique solution.

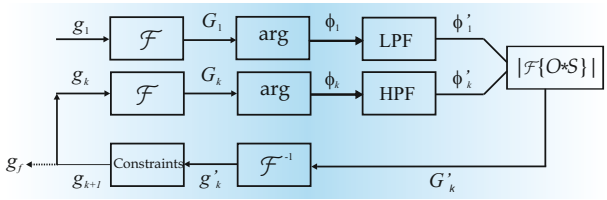

Figure 5.6: Block diagram of our Gerchberg-Saxton-type algorithm: g_1: Initial guess; $\mathcal{F}$: Fourier transform; arg: Argument; LPF: Low-pass filter; HPF: High-pass filter; $|\mathcal{F}\{O * S\}|$: Magnitude of the measured spatial spectrum of the object O; $\mathcal{F}^{-1}$: Inverse Fourier transform; Constraints: Real domain constraints to calculate g_{k+1} out of g_k.

Typically, a Gerchberg-Saxton-type algorithm converges with about 1000 iterations that take in the order of a second with a modern computer. Our new Gerchberg-Saxton-type algorithm uses low-frequency phase of the Fourier components of the object as extra information. In our case, only 300 iterations are

already sufficient. We apply this procedure to 2500 sub-images to obtain the high overlap, therefore the complete reconstruction takes about 20 minutes. The time scale of the reconstruction is independent of the resolution, while it follows a square law with respect to the ratio of the field-of-view and the speckle-scan range. In addition, the algorithm is very easy to parallelize and can run on a graphic card, ideally speeding it up by an order of magnitude.

5.A.3 Convergence properties of the Gerchberg-Saxton-type algorithm

To test the convergence properties of our modified GS algorithm on more complex objects we used a numerical test object composed of six letters on a white background (Fig. 5.7). We simulated the low-resolution imaging by Fourier fil-

Figure 5.7: The numerical test object: The numerical test object consisting of 6 letters on a 164 × 164 pixel canvas.

tering the object with an NA that was between about 1% and 15% of the full bandwidth of the object. Examples at an NA ratio (NA_{det}/NA_{ill}) of 0.05, 0.10 and 0.15 are given in Fig. 5.8.

Figure 5.8: Low-resolution images: Low-resolution images of the numerical object as used as input to the algorithm at an NA ratio of (a) 0.05; (b) 0.10; (c) 0.15.

We ran 6000 steps of our modified GS algorithm to reconstruct the object from the low-resolution image plus the high-resolution autocorrelate. The probability

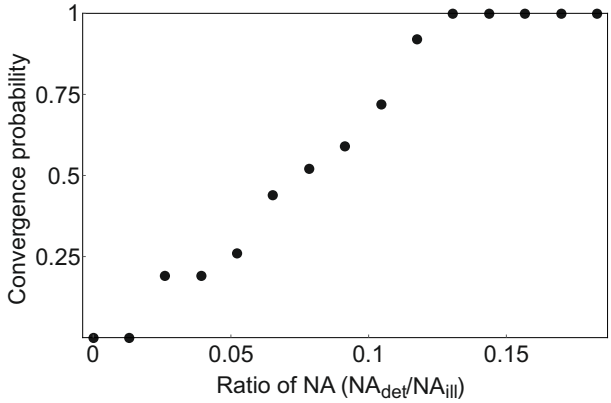

Figure 5.9: Convergence rate: Convergence rate (out of 100 runs seeded with noise as an initial guess) for 6000 steps of our modified GS algorithm, versus NA ratio.

of convergence after 6000 steps is shown versus NA ratio in Fig. 5.9, where we consider the algorithm as converged if the error drops below 1%. An example of a converged and non-converged run are given in Fig. 5.10. In 100 runs we found the algorithm never converged within 6000 steps for the lowest ratios (up to 0.03) and always converged for ratios greater than 0.13.

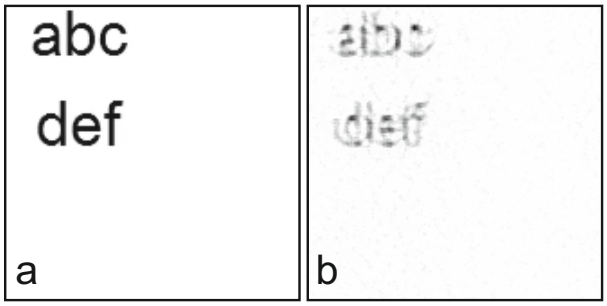

Figure 5.10: Retrieved images: Example of the images retrieved by (a) a converged run and (b) a non-converged run, at a NA ratio of 0.07.

5.A.4 Inverse apodization

In incoherent imaging, optical transfer function of a circular aperture is approximately a cone-shaped function that results in suppression of the high-frequency Fourier components [30]. In our experimental demonstration, both the optical transfer functions of GaP scattering lens and of the detection objective are approximately cone-shaped functions with cut-off spatial frequencies of $k_{\mathrm{ill}} = 27$ µm^{-1} and $k_{\mathrm{det}} = 9.75$ µm^{-1} respectively. We have inverse apodized both wide-

field conventional and SCORE images by dividing Fourier spectra of the wide-field SCORE image and the wide-field conventional image with corresponding inverse apodization functions (see Fig. 5.11).

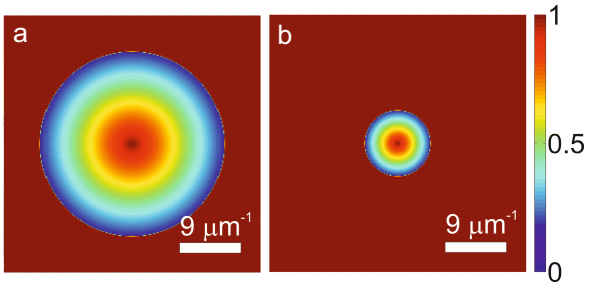

Figure 5.11: Inverse apodization functions: (a) The inverse apodization function of the GaP scattering lens used for the wide-field SCORE image . (b) The inverse apodization function of the collection objective with NA = 0.95 used for the wide-field conventional image.

We used inverse apodization after the reconstruction of the SCORE image, because inverse apodization before the reconstruction affects the positivity of the fluorescence images which makes the reconstruction procedure impossible. We choose the cut-off frequency of our apodization function carefully in order to have minimal artefacts on the final wide-field SCORE image.

5.A.5 Estimation of the object size and the effective NA

In order to estimate the resolution of SCORE results, we deconvolve a SCORE image of a single nanosphere with the known size and shape of the object. In our experiment, we use polystyrene nanospheres with a diameter of 100 nm. Our nanospheres are positioned on the interface between the high-index GaP substrate and the low-index air as shown in Fig. 5.12. Incident light intensity at angles larger than the critical angle ($\theta_c = 17°$) at the interface will be totally internally reflected. However, the incident light will excite the fluorophores in the nanosphere via evanescent wave of the light. The decay length of the evanescent wave intensity depends on the angle of incidence on the interface as shown in Eq. 5.3. The decay length l of the evanescent wave intensity is

$$l(\theta) = \frac{1}{2k\sqrt{n^2 \sin^2\theta - 1}} \tag{5.3}$$

where k is the vacuum wavenumber of the incident light, n the refractive index of the GaP substrate, and θ the internal angle of the incident light on the interface [1]. We take the highest wave vector into consideration, since the highest wave vector determines the resolution. The decay length for the highest wave vector is l = 20 nm. The effective size of a spherical object on the interface will be a Gaussian-shaped object with a full-width-half-maximum of Δ_{object} =70 nm.

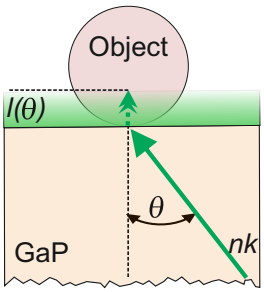

Figure 5.12: Excitation of the fluorophores via evanescent wave: Light of a particular angle $\theta > \theta_c$ excites fluorophores that are buried inside a polystyrene nanosphere. The effective size of the nanosphere is different for each angle of incidence of light, since the decay length l is different for each angle of incidence of light.

In our SCORE images, a single image of a nanosphere has a full-width-half-maximum of Δ_{feature} =135 nm. Therefore we can use the formula to obtain our deconvolved PSF as $\Delta_{\text{PSF}} = (\Delta^2_{\text{feature}} - \Delta^2_{\text{object}})^{1/2} = 116$ nm corresponding to an effective NA = 2.4.

5.A.6 Information-theoretical analysis

In this section, we present an information-theoretical bound on the signal-to-noise ratio of our method and a similar method (blind-SIM). Here, we show how the maximum achievable signal-to-noise ratio of SCORE and blind-SIM images scale with respect to the ratio of the illumination NA and the detection NA ($\text{NA}_{\text{ill}}/\text{NA}_{\text{det}}$).

The information capacity of one degree of freedom of an image is given by

$$H = \frac{1}{2}\log_2(\text{SNR} + 1) \tag{5.4}$$

where signal-to-noise ratio (SNR) is in optical power domain [47]. The information capacity for all degrees of freedom (diffraction-limited spots) of a detected intensity image is

$$H = \sum_{f=1}^{M} \frac{1}{2}\log_2(\text{SNR} + 1) \tag{5.5}$$

where M is the total number of diffraction-limited spots [47].

We assume the noise is uncorrelated between diffraction-limited spots. The autocorrelation has a higher background compared to a standard resolution image and the signal-to-noise ratio drops at high NA ratios due to the finite dynamic range of the detection. Therefore the information capacity of the measured data

of SCORE consisting of N frames of p^2 degrees of freedom is given by

$$H_{\text{in}} = \frac{1}{2} N p^2 \log_2(\text{SNR}_{\text{ac}} + 1) \tag{5.6}$$

$$\text{SNR}_{\text{ac}} = \frac{\text{SNR}_{\text{in}} p}{q} \tag{5.7}$$

where SNR_{ac} is the signal-to-noise ratio of the autocorrelation of the speckle-scan matrix, SNR_{in} the signal-to-noise ratio of a single wide-field image, and q^2 the number of illumination speckle grains in a single wide-field image. Our SCORE algorithm outputs a wide-field image with a resolution of the speckle grain size, and also recovers the illumination speckle pattern, so that the total number of degrees of freedom is $2q^2$. The information capacity of the output data of SCORE is given by

$$H_{\text{out}} = \frac{1}{2} 2q^2 \log_2(\text{SNR}_{\text{out}} + 1) \tag{5.8}$$

where SNR_{out} is the signal-to-noise ratio of the reconstructed SCORE image. The fact that the output cannot contain more information than the input results in

$$H_{\text{out}}^{\max} = H_{\text{in}} \tag{5.9}$$

$$N p^2 \log_2 \left(\frac{\text{SNR}_{\text{in}} p}{q} + 1 \right) = 2q^2 \log_2(\text{SNR}_{\text{out}}^{\max} + 1). \tag{5.10}$$

The number of uncorrelated measurements is $N = q^2/p^2$ assuming our scan area is equal to a diffraction-limited spot of the imaging results in

$$\text{SNR}_{\text{out}}^{\max} = \sqrt{\frac{\text{SNR}_{\text{in}} p}{q} + 1} - 1. \tag{5.11}$$

Here it is evident that as the illumination NA becomes higher compared to the detection NA, the $\text{SNR}_{\text{out}}^{\max}$ drops.

Now we turn to information-theoretical analysis of the blind-SIM method. Information capacity of the measured data of blind-SIM is given by

$$H_{\text{in}} = \frac{1}{2} N p^2 \log_2(\text{SNR}_{\text{in}} + 1). \tag{5.12}$$

Blind-SIM requires illumination of the object with N uncorrelated and different speckle patterns. In essence, this method reconstructs a high-resolution fluorescence image of the object as well as N illuminating high-resolution images of the speckle patterns by a blind-deconvolution-based algorithm with a total number of degrees of freedom of $Nq^2 + (p+q)^2$. Therefore the information capacity of

the reconstructed data of blind-SIM is given by

$$H_{\text{out}} = \frac{1}{2}(Nq^2 + (p+q)^2)\log_2(\text{SNR}_{\text{out}} + 1). \tag{5.13}$$

Here, Nq^2 is the total number of diffraction-limited spots of reconstructed speckle patterns, and $(p+q)^2$ the number diffraction-limited spots of the reconstructed blind-SIM image. The fact that the output cannot contain more information than the input results in

$$H_{\text{out}}^{\max} = H_{\text{in}} \tag{5.14}$$

$$Np^2 \log_2(\text{SNR}_{\text{in}} + 1) = (Nq^2 + (p+q)^2)\log_2(\text{SNR}_{\text{out}}^{\max} + 1). \tag{5.15}$$

Random uncorrelated speckle pattern illumination allows a high oversampling that results in

$$\lim_{N\to\infty} \text{SNR}_{\text{out}}^{\max} = (\text{SNR}_{\text{in}} + 1)^{\frac{p^2}{q^2}}. \tag{5.16}$$

Here it is evident that as the illumination NA becomes higher compared to the detection NA, the $\text{SNR}_{\text{out}}^{\max}$ drops rapidly due to the large number of high-resolution speckle patterns reconstructed from low-resolution images.

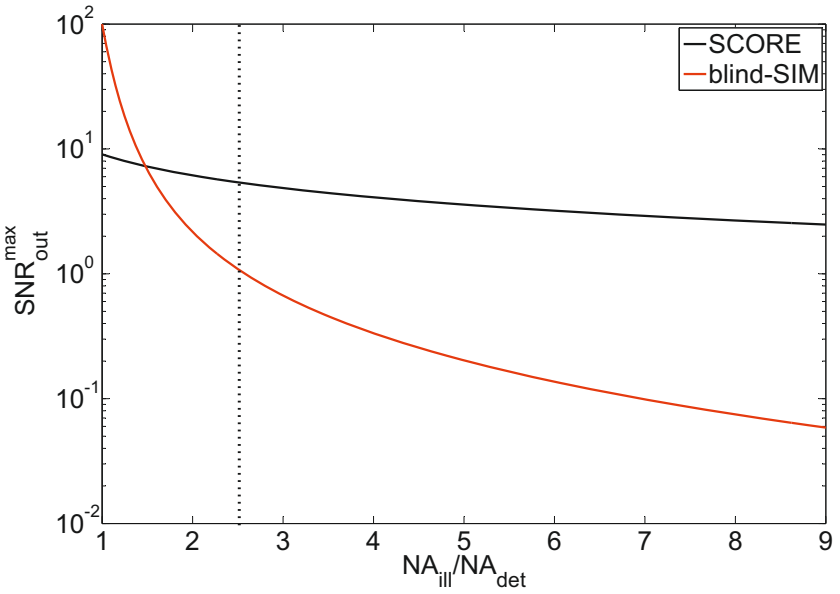

Figure 5.13: Maximum signal-to-noise ratio of the SCORE and the blind-SIM images versus the NA ratio: The black line represents the SNR_{out} of SCORE. The red line represents the SNR_{out} of blind-SIM. The dashed vertical line shows the NA ratio in our experiment.

Fig. 5.13 shows the comparison of the maximum possible SNR_{out} of SCORE to that of blind-SIM. We plotted the graph using equations 5.11 and 5.16 for a $SNR_{in} = 100$ for both methods which is realistic in experimental conditions. The SNR_{out} scaling law is different in each method. Blind-SIM has a higher SNR_{out} if the illumination NA is similar to the detection NA, which is the case when the same microscope objective is used for both illumination and detection. However, SCORE has higher SNR_{out} if the illumination NA is about 1.5 higher than the detection NA. In our case, we use a very high-NA scattering lens in the illumination $NA_{ill} = 2.4$ and a microscope objective in the detection with $NA_{det} = 0.95$. In this regime, SCORE has higher SNR_{out} compared to blind-SIM.

This simple information-theoretical analysis points out the regimes in which each method can be expected to have the best performance.

Bibliography

[1] L. Novotny and B. Hecht, *Principles of nano-optics* (Cambridge Univ. Press, Cambridge, U.K., 2006). — p.9, 67, 81.

[2] E. Betzig, A. Lewis, A. Harootunian, M. Isaacson, and E. Kratschmer, *Near field scanning optical microscopy (NSOM): Development and biophysical applications*, Biophys. J. **49**, 269 (1986). — p.9, 19, 67.

[3] R. Heintzmann and C. Cremer, *Lateral modulated excitation microscopy: Improvement of resolution by using a diffraction grating*, Proc. SPIE **3568**, 185 (1999). — p.9, 19, 67, 68, 91.

[4] M. G. L. Gustafsson, *Surpassing the lateral resolution limit by a factor of two using structured illumination microscopy*, J. Microsc. **198**, 82 (2000). — p.9, 19, 25, 67, 68, 91.

[5] E. Mudry, K. Belkebir, J. Girard, J. Savatier, E. Le Moal, C. Nicoletti, M. Allain, and A. Sentenac, *Structured illumination microscopy using unknown speckle patterns*, Nature Photon. **6**, 312 (2012). — p.19, 27, 67, 68, 73, 75, 92.

[6] M. G. L. Gustafsson, *Nonlinear structured-illumination microscopy: Wide-field fluorescence imaging with theoretically unlimited resolution*, Proc. Natl. Acad. Sci. U.S.A. **102**, 13081 (2005). — p.19, 67, 92.

[7] S. W. Hell and J. Wichmann, *Breaking the diffraction resolution limit by stimulated emission: Stimulated-emission-depletion fluorescence microscopy*, Opt. Lett. **19**, 780 (1994). — p.9, 19, 67, 91, 107.

[8] S. W. Hell, *Far-field optical nanoscopy*, Science **316**, 1153 (2007). — p.9, 19, 67, 91, 107.

[9] M. J. Rust, M. Bates, and X. Zhuang, *Sub-diffraction-limit imaging by stochastic optical reconstruction microscopy (STORM)*, Nat. Methods **3**, 793 (2006). — p.9, 19, 67, 91.

[10] E. Betzig, G. H. Patterson, R. Sougrat, O. W. Lindwasser, S. Olenych, J. S. Bonifacino, M. W. Davidson, J. Lippincott-Schwartz, and H. F. Hess, *Imaging intracellular fluorescent proteins at nanometer resolution*, Science **313**, 1642 (2006). — p.9, 19, 67, 91.

[11] T. Dertinger, R. Colyer, G. Iyer, S. Weiss, and J. Enderlein, *Fast, background-free, 3D super-resolution optical fluctuation imaging (SOFI)*, Proc. Natl. Acad. Sci. U.S.A. **106**, 22287 (2009). — p.9, 19, 67, 91.

[12] A. Derode, A. Tourin, J. de Rosny, M. Tanter, S. Yon, and M. Fink, *Taking advantage of multiple scattering to communicate with time-reversal antennas*, Phys. Rev. Lett. **90**, 014301 (2003). — p.68.

[13] G. Lerosey, J. de Rosny, A. Tourin, and M. Fink, *Focusing beyond the diffraction limit with far-field time reversal*, Science **315**, 1120 (2007). — p.68.

[14] J. García, Z. Zalevsky, and D. Fixler, *Synthetic aperture superresolution by speckle pattern projection*, Opt. Express **13**, 6073 (2005). — p.27, 28, 68, 75.

[15] I. M. Vellekoop, A. Lagendijk, and A. P. Mosk, *Exploiting disorder for perfect focusing*, Nature Photon. **4**, 320 (2010). — p.52, 68.

[16] E. G. van Putten, D. Akbulut, J. Bertolotti, W. L. Vos, A. Lagendijk, and A. P. Mosk, *Scattering lens resolves sub-100 nm structures with visible light*, Phys. Rev. Lett. **106**, 193905 (2011). — p.27, 52, 54, 58, 60, 62, 68, 69, 75, 76, 78, 92, 105, 111.

[17] A. Labeyrie, *Attainment of diffraction limited resolution in large telescopes by Fourier analysing speckle patterns in star images*, Astron. Astrophys. **6**, 85 (1970). — p.68.

[18] J. C. Dainty, *Laser speckle and related phenomena* (Springer, 1984). — p.68.

[19] I. Freund, *Correlation imaging through multiply scattering media*, Phys. Lett. A **147**, 502 (1990). — p.69.

[20] I. Freund, M. Rosenbluh, and S. Feng, *Memory effects in propagation of optical waves through disordered media*, Phys. Rev. Lett. **61**, 2328 (1988). — p.27, 58, 69, 97, 106, 112.

[21] S. Feng, C. Kane, P. A. Lee, and A. D. Stone, *Correlations and fluctuations of coherent wave transmission through disordered media*, Phys. Rev. Lett. **61**, 834 (1988). — p.27, 58, 69, 97, 106, 112.

[22] C. L. Hsieh, Y. Pu, R. Grange, G. Laporte, and D. Psaltis, *Imaging through turbid layers by scanning the phase conjugated second harmonic radiation from a nanoparticle*, Opt. Express **18**, 20723 (2010). — p.27, 58, 69, 76.

[23] I. M. Vellekoop and C. Aegerter, *Scattered light fluorescence microscopy: Imaging through turbid layers*, Opt. Lett. **35**, 1245 (2010). — p.27, 58, 69.

[24] O. Katz, E. Small, and Y. Silberberg, *Looking around corners and through thin turbid layers in real time with scattered incoherent light*, Nature Photon. **6**, 549 (2012). — p.27, 58, 69.

[25] H. He, Y. Guan, and J. Zhou, *Image restoration through thin turbid layers by correlation with a known object*, Opt. Express **21**, 12539 (2013). — p.27, 69.

[26] J. Bertolotti, E. G. van Putten, C. Blum, A. Lagendijk, W. L. Vos, and A. P. Mosk, *Non-invasive imaging through opaque scattering layers*, Nature **491**, 232 (2012). — p.27, 28, 29, 38, 58, 69, 72, 99, 106, 112.

[27] X. Yang, Y. Pu, and D. Psaltis, *Imaging blood cells through scattering biological tissue using speckle scanning microscopy*, Opt. Express **22**, 3405 (2014). — p.27, 29, 69, 72, 106, 112.

[28] O. Katz, P. Heidmann, M. Fink, and S. Gigan, *Non-invasive single-shot imaging through scattering layers and around corners via speckle correlations*, Nature Photon. **8**, 784 (2014). — p.27, 29, 69, 72, 106, 112.

[29] J. W. Goodman, *Statistical Optics* (Wiley, New York, 2000). — p.71.

[30] J. W. Goodman, *Introduction to Fourier Optics* (Roberts & Company, Englewood, 2005). — p.10, 11, 19, 21, 71, 80.

[31] J. R. Fienup, *Reconstruction of an object from the modulus of its Fourier transform*, Opt. Lett. **3**, 27 (1978). — p.29, 71, 99, 106, 112.

[32] J. R. Fienup, *Phase retrieval algorithms: A comparison*, Appl. Opt. **21**, 2758 (1982). — p.29, 71, 78, 99, 106, 112.

[33] R. P. Millane, *Phase retrieval in crystallography and optics*, J. Opt. Soc. Am. A **7**, 394 (1990). — p.29, 71, 72, 106, 112.

[34] A. Szameit *et al.*, *Sparsity-based single-shot sub-wavelength coherent diffractive imaging*, Nat. Mater. **11**, 455 (2012). — p.71.

[35] Y. Shechtman, Y. C. Eldar, O. Cohen, H. N. Chapman, J. Miao, and M. Segev, *Phase retrieval with application to optical imaging: A contemporary overview*, IEEE Signal Processing Mag. **32**, 87 (2015). — p.29, 72, 99, 106, 112.

[36] H. M. L. Faulkner and J. M. Rodenburg, *Movable aperture lensless transmission microscopy: A novel phase retrieval algorithm*, Phys. Rev. Lett. **93**, 023903 (2004). — p.72.

[37] J. M. Rodenburg, A. C. Hurst, A. G. Cullis, B. R. Dobson, F. Pfeiffer, O. Bunk, C. David, K. Jefimovs, and I. Johnson, *Hard-X-ray lensless imaging of extended objects*, Phys. Rev. Lett. **98**, 034801 (2007). — p.72.

[38] A. M. Maiden, J. M. Rodenburg, and M. J. Humphry, *Optical ptychography: A practical implementation with useful resolution*, Opt. Lett. **35**, 2585 (2010). — p.72.

[39] G. Zheng, R. Horstmeyer, and C. Yang, *Wide-field, high-resolution Fourier ptychographic microscopy*, Nature Photon. **7**, 739 (2013). — p.25, 72.

[40] J. R. Fienup and C. C. Wackerman, *Phase-retrieval stagnation problems and solutions*, J. Opt. Soc. Am. A **3**, 1897 (1986). — p.73.

[41] S. Dong, P. Nanda, R. Shiradkar, K. Guo, and G. Zheng, *High-resolution fluorescence imaging via pattern-illuminated Fourier ptychography*, Opt. Express **22**, 20856 (2014). — p.19, 27, 30, 73, 92.

[42] K. Wicker and R. Heintzmann, *Resolving a misconception about structured illumination*, Nature Photon. **8**, 342 (2014). — p.74, 91.

[43] J.-H. Park, C. Park, H. S. Yu, J. Park, S. Han, J. Shin, S. H. Ko, K. T. Nam, Y.-H. Cho, and Y. Park, *Subwavelength light focusing using random nanoparticles*, Nature Photon. **7**, 454 (2013). — p.75.

[44] F. J. P. Schuurmans, D. Vanmaekelbergh, J. van de Lagemaat, and A. Lagendijk, *Strongly photonic macroporous gallium phosphide networks*, Science **284**, 141 (1999). — p.52, 54, 76.

[45] S. Popoff, G. Lerosey, M. Fink, A. C. Boccara, and S. Gigan, *Image transmission through an opaque material*, Nat. Commun. **1**, (2010). — p.10, 27, 76.

[46] Y. Choi, T. D. Yang, C. Fang-Yen, P. Kang, K. J. Lee, R. R. Dasari, M. S. Feld, and W. Choi, *Overcoming the diffraction limit using multiple light scattering in a highly disordered medium*, Phys. Rev. Lett. **107**, 023902 (2011). — p.10, 27, 76.

[47] M. A. Neifeld, *Information, resolution, and space-bandwidth product*, Opt. Lett. **23**, 1477 (1998). — p.10, 11, 82.

CHAPTER 6

Resolution enhancement via periodic pattern illumination through a scattering layer

High-resolution, high-contrast imaging of interfaces and surfaces of nanostructures is of great importance in nanofabrication and biological sciences. Here, we present a new high-resolution and high-contrast fluorescence imaging method that is based on periodic pattern illumination through the scattering layer of a high-index substrate. We demonstrate imaging of a collection of dye-doped polystyrene nanospheres. The resolution of our proof-of-principle images is significantly better than that of our NA = 0.95 microscope objective lens, but could not yet be quantitatively measured. Our method produces high-contrast fluorescence images and has a potential resolution that exceeds any current state-of-the-art linear, deterministic fluorescence imaging method.

6.1 Introduction

High-resolution fluorescence imaging is indispensable to study structure and function of bio- and nano-materials down to single molecule scale [1]. Several methods have been developed that reach a spatial resolution beyond Abbe's resolution limit using specific photophysical properties of fluorescent emitters [2–6]. These methods are based on the assumption that the specimen is made of discrete single fluorescent emitters. Each of these methods uses either a stochastic or a nonlinear process to reach a high resolution. Structured illumination microscopy (SIM) follows a linear and deterministic approach which is independent of the photophysical properties of the fluorescent emitters [7, 8]. SIM is based on exploitation of moiré patterns that are produced by spatial frequency mixing of spatially shaped illumination patterns and the structure of the fluorescent specimen. A periodic illumination pattern shifts the high-frequency Fourier components of the specimen down to the band-pass of the optical transfer function of the conventional optics. A series of measurements using periodic illumination patterns with a few translations and rotations provide sufficient information to reconstruct a high resolution image. A typical implementation of SIM reaches a spatial resolution that is approximately two times finer than the resolution of the involved conventional optics [9, 10]. Higher resolutions can be achieved using a nonlinear

photoresponse of incoherent emitters that have a high damage threshold [11].

SIM requires precise knowledge of the illumination patterns. In order to collect artefact-free high-resolution images, a very precise optical alignment and a very stable mechanical arrangement is indispensable. It has been shown that distorted periodic illumination patterns [12] or even speckle illumination patterns [13, 14] can be used to produce high-resolution images. However unlike traditional SIM, these methods require intense computer algorithms that suffer from noise especially when the Fourier spatial bandwidth of the illumination pattern is higher than the Fourier spatial bandwidth of the detection. This is especially apparent in plasmonic structured illumination microscopy [15–17].

In combination with structured illumination, total internal reflection fluorescence microscopy (TIRF) [18] enables a very high contrast as well as sub-Abbe-resolution of surfaces and interfaces [19, 20]. The gallium phosphide (GaP) scattering solid immersion lens (SSIL) is an excellent candidate for TIRF microscopy because of its very high-refractive index up to $n = 3.4$ and abberation-free imaging potential [21, 22].

In this chapter, we demonstrate a new fluorescence imaging method that is based on periodic structured illumination through the scattering surface of a GaP scattering solid immersion lens (SSIL). We demonstrate enhanced resolution imaging of dye-doped polystyrene nanospheres compared to a state-of-the-art conventional microscope objective. We also show that our method reduces the out of focus background fluorescence signal. Our method makes use of the straightforward reconstruction approach of SIM and does not require an intensive reconstruction algorithm, therefore works with geometries where the Fourier spatial bandwidth of the illumination pattern is higher than the Fourier spatial bandwidth of the detection. Our method offers wide-field, background-free, and sub-Abbe-resolution fluorescence imaging of interfaces and surfaces of nanostructures.

In our approach, the periodic illumination pattern behind the rough scattering surface of the GaP SSIL is generated by two centrosymmetric sharp foci on the rough scattering surface. As the transmitted light through the location of two foci on the rough surface propagates behind the scattering surface, they generate a locally smooth and periodic interference pattern in far-field. The interference pattern can be easily shifted and rotated by adjusting the relative phases of two foci and moving them on the scattering surface. Adjustability of the periodic illumination patterns enables a systematic measurement of the Fourier components of a fluorescent object.

6.2 Experimental setup

In Fig. 6.1 the experimental setup is shown. The heart of our experiment is a GaP SSIL. The SSIL is made of a 400-µm-thick GaP wafer of which one side is a rough scattering surface and one side is polished and coated with 100-nm-thick silicon (Si). Several 10-µm-scale windows were made in this Si layer by thermal cycling. The object plane is the GaP-air interface in such a window. We

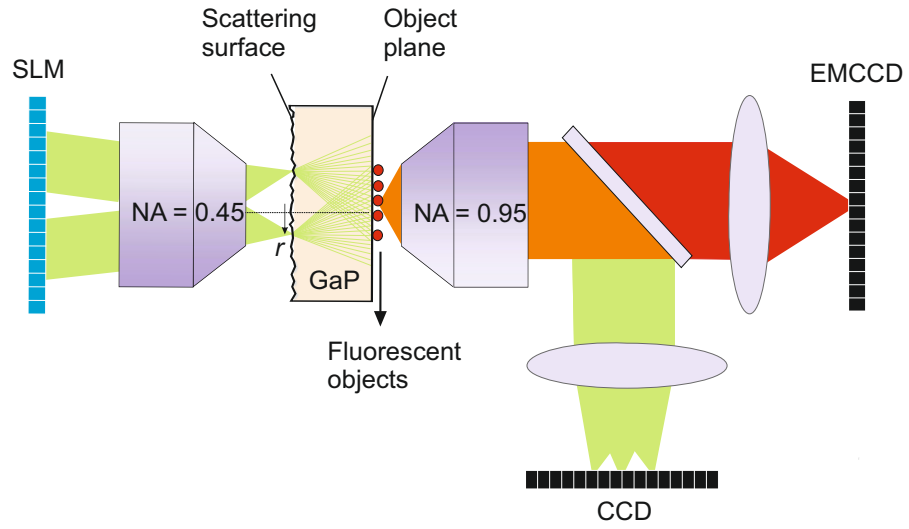

Figure 6.1: The experimental setup. Two plane waves from a spatial light modulator (SLM) are focused on two different positions on the scattering surface of the GaP scattering solid immersion lens (SSIL) using a microscope objective (Nikon: 20×, NA = 0.45). The lenses to image the SLM surface on the pupil of the microscope objective are not shown in the cartoon. The fluorescent nanospheres on the object plane is imaged on a CCD camera and an EMCCD camera using a high numerical aperture microscope objective and a tube lens. A dichroic mirror makes it sure that the CCD camera only detects the illumination light, and the EMCCD camera only detects the fluorescent light.

deposited dye-doped fluorescent nanospheres with a diameter of 50 nm on the object plane. A laser beam (Cobolt Jive, 100 mW continuous wave at 561 nm) is coupled into a single mode optical fiber to clean the beam, the output beam of the optical fiber is expanded and spatially controlled with a spatial light modulator (Holoeye PLUTO-VIS-014-C). The Fourier plane of the spatial light modulator (SLM) is imaged onto the scattering surface of the GaP SSIL. The object plane is imaged onto an electron multiplying CCD camera (Andor iXon Ultra 897) and a CCD camera (Allied Vision Technologies Stingray F-145) using a microscope objective (Zeiss: Infinity corrected, 63×, NA = 0.95) and a tube lens with a focal length of 500 mm. A dichroic mirror separates the illumination light and the fluorescent light and multiple band-pass filters (Semrock FF01-620/52-25) in front of the EMCCD camera ensure that we detect only the fluorescence signal on the EMCCD camera and only the illumination signal on the CCD camera.

6.3 Measurement procedure

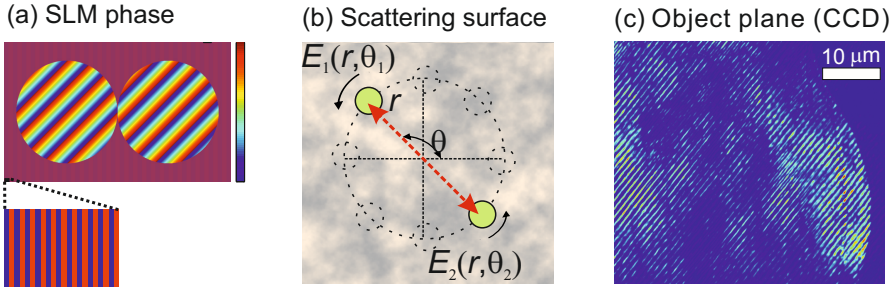

Figure 6.2: Periodic pattern formation on the object plane. (a) An example of a phase pattern displayed on the spatial light modulator (SLM). A zoom in shows the grating pattern displayed in order to suppress the background light. (b) SLM generates two foci E_1 and E_2 on the scattering surface. The foci can be moved on any position on the scattering surface by adjusting parameters r, θ_1, and θ_2. (c) A CCD camera image that shows an example of a periodic pattern on the object plane for $r = 50$ µm, $\theta_1 = 3\pi/4$, $\theta_2 = 7\pi/4$, and $\phi_1 = \phi_2$.

Here, we describe the measurement procedure that enables measurement of sufficient information to reconstruct a high-resolution image of the fluorescent object. The illumination light is structured in a specific way. We displayed two blazed gratings on two separated disk-shaped parts of the SLM (Fig. 6.2a) to generate two centrosymmetric foci $E_1(r,\theta_1)e^{i\phi_1}$ and $E_2(r,\theta_2)e^{i\phi_2}$ on the scattering surface (Fig. 6.2b). Here r, θ_1, and θ_2 are the positions of the foci E_1 and E_2 in polar coordinates where $\theta_1 = \theta_2 - \pi$ and ϕ_1 and ϕ_2 are the phases of the foci E_1 and E_2 respectively where $\Delta\phi = \phi_2 - \phi_1$. We displayed a high-frequency grating pattern on the remaining area of the SLM to remove the background

light. Light from the two foci is scattered at the first surface and forms an interference pattern on the object plane as shown in Fig. 6.2c. The interference pattern locally resembles a set of fringes with a spatial frequency

$$k_{\mathrm{ill}} = \sqrt{k_{\mathrm{x}}^2 + k_{\mathrm{y}}^2} = \frac{2\pi n r}{\lambda_{\mathrm{ill}} \sqrt{r^2 + L^2}} \tag{6.1}$$

and angle θ, but *a priori* unknown phase. The measurement procedure exploits these fringes for resolution enhancement very similar to SIM.

In order to measure all accessible spatial Fourier components of the fluorescent object, we applied the following measurement procedure: We recorded a series of wide-field images labeled $I(m, r, \theta, \Delta\phi)$ for $m = 0, 1, 2$, for $r = 20$ µm to $r = 200$ µm with steps of 20 µm, for $\theta = 0$ to $\theta = \pi$ with steps of $\pi/18$, and for $\Delta\phi = 0$ to $\Delta\phi = 7\pi/8$ with steps of $\pi/8$. Here $m = 0$ corresponds to two foci illumination, $m = 1$ illumination only with focus E_1, and $m = 2$ illumination only with focus E_2. The ensemble of measurements forms our data-cube $I(m, x, y, r, \theta, \Delta\phi)$ which is the basis for construction of sub-Abbe-resolution fluorescence images of our object.

6.4 Resolution enhancement

To produce sub-Abbe-resolution images from our data-cube we implemented the procedure depicted in Fig. 6.3. In our experiment, the scattering surface distorts the periodic illumination patterns. Nevertheless, we observe that the periodic illumination pattern is smooth within the correlation length of

$$l_{\mathrm{c}} = \frac{\lambda_{\mathrm{ill}}}{n} \sqrt{\left(\frac{r^2 + L^2}{La}\right)^2 + \frac{1}{4}} \tag{6.2}$$

of the illumination pattern where λ_{ill} is the wavelength of the illumination beam, n the refractive index of GaP, a the focus size on the scattering surface, r the radial position of the foci, and L the thickness of the GaP SSIL. In our experiment, the correlation length is about $l_{\mathrm{c}} \approx 10$ µm for $r = 80$ µm. To analyse an area smaller than l_{c}, we cropped an area of 2 µm × 2 µm of the data-cube $I(m, x, y, r, \theta, \Delta\phi)$ which corresponds to $N \times N = 26 \times 26$ pixels of the recorded EMCCD camera images. We first applied a Tukey window function to the cropped sub-images. We Fourier transformed the sub-images for $r = 80$ µm, $m = 0, 1, 2$, $\Delta\phi = 0, 5\pi/8, 7\pi/8$, and 18 angles of θ between $\theta = 0$ and $\theta = \pi$. Each Fourier transform of a sub-image contains sub-Abbe-resolution information that is not available with a uniform illumination pattern. However, the high-resolution information is superimposed with the low-resolution information in the Fourier domain, resulting in an image with Fourier components $F_{\Delta\phi}(k)$

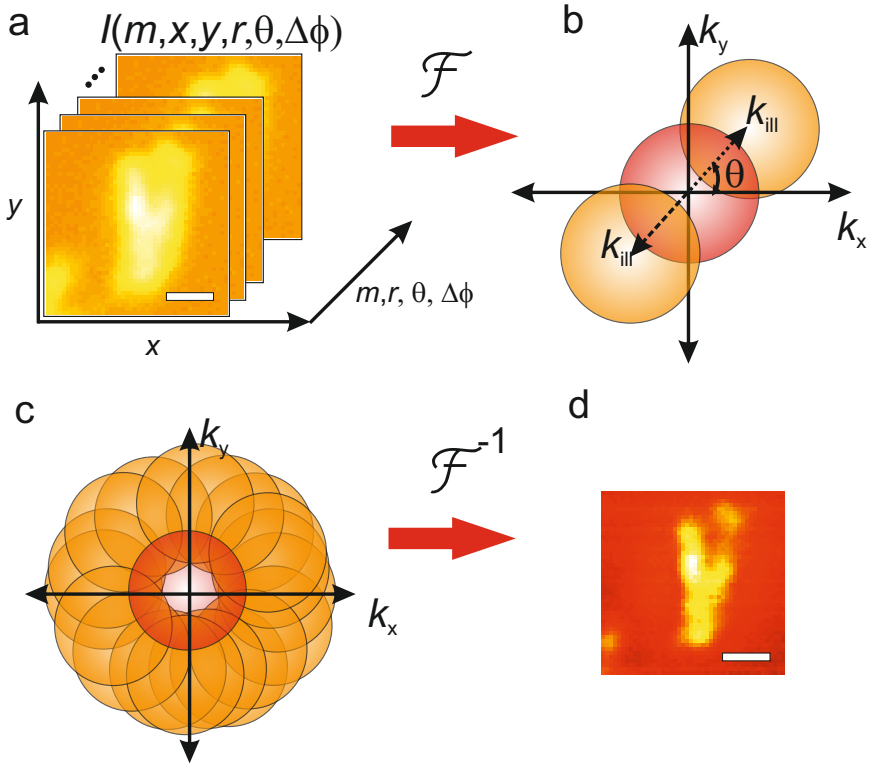

Figure 6.3: High-resolution image reconstruction procedure. (a) The sub-data-cube. (b) Shifting separated high-resolution information of a Fourier sub-image for corresponding θ and k_{ill}. (c) Combining high-resolution information for all measured angles of θ. (d) A reconstructed high-resolution sub-image after the inverse Fourier transform of (c). The scale bar represents 1 µm.

given by

$$F_{\Delta\phi}(k) = I_0 \left(F(k) + \frac{I_1 I_2}{I_1^2 + I_2^2} \left(F(k + k_{\mathrm{ill}}) \mathrm{e}^{\mathrm{i}(\Delta\phi + \delta\phi)} + F(k - k_{\mathrm{ill}}) \mathrm{e}^{-\mathrm{i}(\Delta\phi + \delta\phi)} \right) \right) \tag{6.3}$$

where I_0 is a prefactor, I_1 the total intensity of the object when the object is illuminated only with the first beam, I_2 the total intensity of the object when the object is illuminated only with the second beam, $\delta\phi$ a random phase offset of the periodic illumination pattern, and $F(k)$ the spatial Fourier transform of the object; $F(k + k_{\mathrm{ill}})$ and $F(k - k_{\mathrm{ill}})$ are the shifted high-frequency Fourier components of the object. We found the $F(k)$, $F(k + k_{\mathrm{ill}})$, and $F(k - k_{\mathrm{ill}})$ by constructing three equations for $\Delta\phi = 0, 5\pi/8$, and $7\pi/8$. As shown in Fig. 6.3b, we shifted the center of $F(k + k_{\mathrm{ill}})$ and $F(k - k_{\mathrm{ill}})$ for the corresponding θ and the spatial frequency k_{ill}. Then we combine $F(k + k_{\mathrm{ill}})$ and $F(k - k_{\mathrm{ill}})$ in k-plane for all measured angles of θ as shown in Fig. 6.3c. Here, we take the random phase offset as $\delta\phi = 0$ for every θ. We inverse Fourier transformed the combined Fourier sub-image. We repeated the same procedure $N \times N$ times by cropping a one pixel shifted sub-image in the wide-field images. We finally tiled the overlapping reconstructed sub-images and obtain a high-resolution sub-image as shown in Fig. 6.3d. The fact that limited l_{c} obligates cropping and parallel processing of sub-images for the reconstruction of a wide-field image has conceptual similarity with the image reconstruction method used in speckle correlation resolution enhancement (SCORE) microscopy that is presented in chapter 5. However, in SCORE the limiting factor for the size of a sub-image is the range of the optical memory effect [23, 24] instead of the correlation length l_{c}. In addition the theoretical resolution of SCORE is slightly lower than of the method discussed in this chapter.

6.5 Results and discussion

Fig. 6.4 shows the conventional and the reconstructed fluorescence images of a collection of nanospheres. In Fig. 6.4a we see a conventional fluorescence image, and in Fig. 6.4b its cross-section. We see two peaks on top of a very high background. Now we turn to the reconstructed fluorescence image. In Fig. 6.4c we see the reconstructed fluorescence image, and in Fig. 6.4d its cross-section. Although we still see two peaks in the cross-section image, the background signal is lower compared to conventional fluorescence image.

In our method, we expect a resolution that is given by

$$\delta r = \frac{\pi}{k_{\mathrm{ill}} + k_{\mathrm{det}}} \tag{6.4}$$

where k_{ill} is the spatial frequency for the illumination pattern, and k_{det} the highest spatial frequency of the optical transfer function of the microscope objective in the detection. In the present case, we expect an enhanced resolution of $\delta r = 180$ nm. Note that the resolution of the conventional optics for our NA

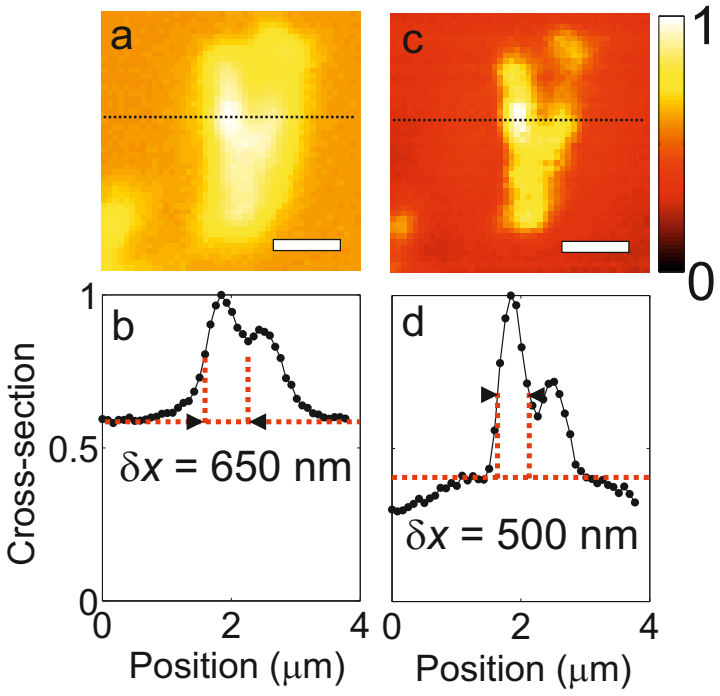

Figure 6.4: Fluorescence images taken by conventional and by scattered structured illumination. (a) Conventional fluorescence image of a collection of nanospheres. (b) A cross-section of (a) shown by the dashed black line. The feature size is estimated as $\delta x = 650$ nm for the left peak. (c) The reconstructed high-resolution fluorescence image. (d) A cross-section of (c) shown by the dashed black line. The feature size is $\delta x = 500$ nm for the left peak. It is evident that the reconstructed fluorescence image is sharper and has a higher contrast compared to the conventional fluorescence image. The scale bar represents 1 μm.

= 0.95 microscope objective lens is $\delta r = 322$ nm. The object is a cluster of several nanospheres, therefore it is very difficult to comment on the resolution of the images. As a rough indication, the width of the left (highest) peak is shown at 50% above the base line. The feature size is estimated as $\delta x = 650$ nm in the standard resolution image, and only $\delta x = 500$ nm in the enhanced image, suggesting a significant improvement comparable to the expected improvement in resolution. A collection of isolated nanospheres has to be imaged in order to retrieve more quantitative information on the resolution.

The resolution of our reconstructed image can be enhanced further with the following improvement in our analysis. In our analysis, we took the random phase offset $\delta\phi = 0$ which reduces the final obtained resolution of our reconstructed image. It is possible to enhance the resolution even further by estimating $\delta\phi$. The random phase offset $\delta\phi$ can be extracted for $k_{\mathrm{ill}} < 2\pi \mathrm{NA}_{\mathrm{det}}/\lambda_{\mathrm{ill}}$ from the measured periodic illumination patterns. For $k_{\mathrm{ill}} \geqslant 2\pi \mathrm{NA}_{\mathrm{det}}/\lambda_{\mathrm{ill}}$ it is possible to estimate $\delta\phi$ from the overlap of the Fourier transforms $F_{\Delta\phi}(k)$.

In our analysis, we processed the data-cube $I(m, x, y, r, \theta, \Delta\phi)$ only for $r = 80$ µm for practical reasons. Here $r = 80$ µm corresponds to a spatial frequency of $k_{\mathrm{ill}} = 7.5$ µm^{-1}. The signal-to-noise for the illumination patterns with higher spatial frequencies have extremely low signal levels. This is probably due to the small size (50 nm in diameter) of the fluorescent nanospheres. Therefore, the phase information for very high-frequency Fourier components is lost. In future, a light source with a higher power or an iterative phase retrieval algorithm [25–28] can be used to retrieve the lost phase information of the high-frequency Fourier components.

6.6 Conclusion

We presented a new high-resolution fluorescence imaging method that is based on periodic pattern illumination through a GaP scattering solid immersion lens (SSIL). We demonstrated a proof-of-principle experiment that produces an improved fluorescence image of a cluster of fluorescent nanospheres. Combining a GaP SSIL with structured illumination methods offers wide-field, high-contrast fluorescence imaging of interfaces and surfaces of nanostructures with a theoretical resolution down to 75 nm. In first experiments we have seen a significant improvement of resolution, but not yet approached the theoretical limit.

Bibliography

[1] J. R. Lakowicz, *Principles of fluoresence spectroscopy, 3rd edition* (Springer, 2006). — p.91.

[2] S. W. Hell and J. Wichmann, *Breaking the diffraction resolution limit by stimulated emission: Stimulated-emission-depletion fluorescence microscopy*, Opt. Lett. **19**, 780 (1994). — p.9, 19, 67, 91, 107.

[3] S. W. Hell, *Far-field optical nanoscopy*, Science **316**, 1153 (2007). — p.9, 19, 67, 91, 107.

[4] M. J. Rust, M. Bates, and X. Zhuang, *Sub-diffraction-limit imaging by stochastic optical reconstruction microscopy (STORM)*, Nat. Methods **3**, 793 (2006). — p.9, 19, 67, 91.

[5] E. Betzig, G. H. Patterson, R. Sougrat, O. W. Lindwasser, S. Olenych, J. S. Bonifacino, M. W. Davidson, J. Lippincott-Schwartz, and H. F. Hess, *Imaging intracellular fluorescent proteins at nanometer resolution*, Science **313**, 1642 (2006). — p.9, 19, 67, 91.

[6] T. Dertinger, R. Colyer, G. Iyer, S. Weiss, and J. Enderlein, *Fast, background-free, 3D super-resolution optical fluctuation imaging (SOFI)*, Proc. Natl. Acad. Sci. U.S.A. **106**, 22287 (2009). — p.9, 19, 67, 91.

[7] R. Heintzmann and C. Cremer, *Lateral modulated excitation microscopy: Improvement of resolution by using a diffraction grating*, Proc. SPIE **3568**, 185 (1999). — p.9, 19, 67, 68, 91.

[8] M. G. L. Gustafsson, *Surpassing the lateral resolution limit by a factor of two using structured illumination microscopy*, J. Microsc. **198**, 82 (2000). — p.9, 19, 25, 67, 68, 91.

[9] R. Heintzmann and M. G. L. Gustafsson, *Subdiffraction resolution in continuous samples*, Nature Photon. **3**, 362 (2009). — p.19, 25, 91.

[10] K. Wicker and R. Heintzmann, *Resolving a misconception about structured illumination*, Nature Photon. **8**, 342 (2014). — p.74, 91.

[11] M. G. L. Gustafsson, *Nonlinear structured-illumination microscopy: Wide-field fluorescence imaging with theoretically unlimited resolution*, Proc. Natl. Acad. Sci. U.S.A. **102**, 13081 (2005). — p.19, 67, 92.

[12] R. Ayuk, H. Giovannini, A. Jost, E. Mudry, J. Girard, T. Mangeat, N. Sandeau, R. Heintzmann, K. Wicker, K. Belkebir, and A. Sentenac, *Structured illumination fluorescence microscopy with distorted excitations using a filtered blind-SIM algorithm*, Opt. Lett. **38**, 4723 (2013). — p.92.

[13] E. Mudry, K. Belkebir, J. Girard, J. Savatier, E. Le Moal, C. Nicoletti, M. Allain, and A. Sentenac, *Structured illumination microscopy using unknown speckle patterns*, Nature Photon. **6**, 312 (2012). — p.19, 27, 67, 68, 73, 75, 92.

[14] S. Dong, P. Nanda, R. Shiradkar, K. Guo, and G. Zheng, *High-resolution fluorescence imaging via pattern-illuminated Fourier ptychography*, Opt. Express **22**, 20856 (2014). — p.19, 27, 30, 73, 92.

[15] F. Wei and Z. Liu, *Plasmonic structured illumination microscopy*, Nano Lett. **10**, 2531 (2010). — p.19, 92.

[16] F. Wei, D. Lu, W. Shen, H. Wan, J. L. Ponsetto, E. Huang, and H. Liu, *Wide field super-resolution surface imaging through plasmonic structured illumination microscopy*, Nano Lett. **14**, 4634 (2014). — p.19, 92.

[17] A. I. Fernández-Domínguez, Z. Liu, and J. B. Pendry, *Coherent four-fold super-resolution imaging with composite photonic-plasmonic structured illumination*, ACS Photonics **2**, 341 (2015). — p.19, 92.

[18] D. Axelrod, N. L. Thompson, and T. P. Bughardt, *Total internal reflection fluorescent microscopy*, J. Microsc. **129**, 19 (1983). — p.92.

[19] R. Fiolka, M. Beck, and A. Stemmer, *Structured illumination in total internal reflection fluorescence microscopy using a spatial light modulator*, Opt. Lett. **33**, 1629 (2008). — p.92.

[20] L. Wang, M. C. Pitter, and M. G. Somekh, *Wide-field high-resolution structured illumination solid immersion fluorescence microscopy*, Opt. Lett. **36**, 2794 (2011). — p.92.

[21] E. G. van Putten, D. Akbulut, J. Bertolotti, W. L. Vos, A. Lagendijk, and A. P. Mosk, *Scattering lens resolves sub-100 nm structures with visible light*, Phys. Rev. Lett. **106**, 193905 (2011). — p.27, 52, 54, 58, 60, 62, 68, 69, 75, 76, 78, 92, 105, 111.

[22] H. Yılmaz, *Advanced optical imaging with scattering lenses, Chapter 4*, Ph.D. thesis, University of Twente, 2015. — p.92.

[23] I. Freund, M. Rosenbluh, and S. Feng, *Memory effects in propagation of optical waves through disordered media*, Phys. Rev. Lett. **61**, 2328 (1988). — p.27, 58, 69, 97, 106, 112.

[24] S. Feng, C. Kane, P. A. Lee, and A. D. Stone, *Correlations and fluctuations of coherent wave transmission through disordered media*, Phys. Rev. Lett. **61**, 834 (1988). — p.27, 58, 69, 97, 106, 112.

[25] J. R. Fienup, *Reconstruction of an object from the modulus of its Fourier transform*, Opt. Lett. **3**, 27 (1978). — p.29, 71, 99, 106, 112.

[26] J. R. Fienup, *Phase retrieval algorithms: A comparison*, Appl. Opt. **21**, 2758 (1982). — p.29, 71, 78, 99, 106, 112.

[27] J. Bertolotti, E. G. van Putten, C. Blum, A. Lagendijk, W. L. Vos, and A. P. Mosk, *Non-invasive imaging through opaque scattering layers*, Nature **491**, 232 (2012). — p.27, 28, 29, 38, 58, 69, 72, 99, 106, 112.

[28] Y. Shechtman, Y. C. Eldar, O. Cohen, H. N. Chapman, J. Miao, and M. Segev, *Phase retrieval with application to optical imaging: A contemporary overview*, IEEE Signal Processing Mag. **32**, 87 (2015). — p.29, 72, 99, 106, 112.

CHAPTER 7
Summary & outlook

7.1 Summary

In this thesis we have demonstrated new advanced optical methods based on spatial control of coherent light for focusing and high-resolution optical imaging applications that benefit from random light scattering through disordered photonic media. In this chapter we summarize all the research in this thesis and we give future directions to further advance our methods.

We have demonstrated optimal focusing of coherent light through scattering media in the presence of experimental noise. In wavefront shaping experiments, noise causes measurement errors in the phase of the transmitted light field through the sample. We used a two-step optimization procedure to minimize the errors in the measurement of the optimal phase in the transmitted light field. We found that a two-step optimization procedure suppresses the camera readout noise and brings the experiment into a shot-noise limited regime. Therefore we concluded that a wavefront shaping experiment is always shot-noise limited with a two-step optimization procedure. We demonstrated that the enhancement factor is proportional to the square root of the total number of photoelectrons detected in a wavefront shaping experiment. In cases where the scattering medium is dynamic such as clouds or biological tissue, the total number of photons (photon budget) that can be detected is fundamentally limited by the decorrelation time of the medium and laser power, therefore shot-noise fundamentally limits the measurable information density. Our results bring new insights to wavefront shaping experiments from an information-theoretical point of view.

High-index substrates of silicon (Si) or gallium phosphide (GaP) are essential materials for high-resolution solid immersion microscopy [1–6]. A scattering solid immersion lens (SSIL) has been reported which enables sub-100 nm resolution with visible light [7]. The high resolution of SSIL is due to injection of high internal-angles into the high-index substrate via random light scattering. However, the previously used SSIL is very inefficient due to the optically thick scattering layer. We addressed the question whether an unpolished rough surface could be sufficient for high internal-angle scattering. Until now there was no convenient method to characterize SSILs. We have developed a new optical characterization method that enables measurement of high internal-angle scattering of high-index substrates. We have confirmed that a SSIL with an unpolished rough surface is at least as good as a SSIL with a thick scattering layer for sub-100 nm optical imaging.

We have developed speckle correlation resolution enhancement (SCORE) imaging that simultaneously produces wide-field and high-resolution fluorescence images. SCORE is a scanning optical microscopy method that benefits from a speckle correlation effect, known as the optical memory effect [8, 9] to scan a high-resolution speckle pattern on a fluorescent object. The high-resolution of SCORE is due to very fine speckle patterns that are generated by a solid immersion medium which is made of a gallium phosphide (GaP) substrate with a scattering layer. The wide-field of SCORE is due to wide-field of view of the detection optics. In essence, SCORE is a computational imaging method that uses a new phase retrieval algorithm that we have developed. Previously reported similar phase retrieval algorithms suffer from ambiguities that causes stagnation problem [10–13] or trivial flips and translations [14–16]. In SCORE, we use conventional images as an extra information for our algorithm which provides a unique solution even for complex object structures. SCORE is robust against optical aberrations or drifts. The statistical nature of speckle patterns enables aberration-free, high-resolution imaging under ambient conditions.

Seeking to improve even the high resolution of SCORE, we have developed and presented a new high-resolution fluorescence imaging method that is based on periodically patterned light illumination through scattering medium. Our wide-field and high-contrast fluorescence imaging method enables sub-Abbe-resolution images of surfaces and interfaces of nanostructures and it has a theoretical resolution of 75 nm. In our initial demonstration we have demonstrated a significant improvement both in resolution and contrast, however we have not reached the theoretical limit yet.

7.2 Outlook

We have studied the effect of noise in wavefront shaping through a scattering medium. With the emergence of digital micromirror devices (DMD) and new wavefront control schemes [17], wavefront shaping experiments can be accelerated by orders of magnitude. In future, one can study information-theoretical limitations of the control of light propagation through dynamic scattering media such as biological tissue or clouds in a regime where the integration time in the detection is the limiting factor of the speed of the experiments. It has been reported that scattering medium can be used as a physically unclonable function (PUF) for quantum-secure authentication [18, 19]. A fundamental information-theoretical study of wavefront shaping or digital optical phase conjugation of single photons [20, 21] is extremely interesting for applications such as quantum-secure authentication with scattering media.

We have developed a new method to measure high internal-angle scattering of scattering layers with a high-index substrate. In future, our method can be used to quantify the effective index of strongly scattering media. It is extremely important to know the effective index to understand the statistics of transmission eigenvalues of a strongly scattering medium in optical transmission matrix measurements [22]. Our new characterization method can shed light to statistics

of optical transmission matrices of strongly scattering media.

We have developed SCORE to image nanostructures simultaneously with a wide field of view and high resolution. Our method can be combined with stimulated emission depletion (STED) microscopy [23, 24]. In essence, a speckle pattern contains several distorted very fine doughnut shaped patterns in a GaP scattering solid immersion lens. With a pump-probe beam, the STED signal can be detected in wide-field. A SCORE procedure with STED can enable an autocorrelation function of the STED speckle pattern with a sharp peak with sub-Abbe-resolution size. The advantage of using a very fine speckle pattern will be a high-resolution with lower pump intensities compared to typical STED microscopy.

We presented initial results of our new high-resolution optical imaging method that is based on periodic pattern illumination through a scattering medium. In future, the data analysis procedure can be improved to explore the full potential of our method. A resolution of about 75 nm with green light illumination is theoretically possible with a sufficient signal-to-noise ratio. As we demonstrated for SCORE imaging, a thorough information theoretical-analysis of scattered structured illumination imaging can be done to estimate the theoretical limitations.

Bibliography

[1] S. M. Mansfield and G. S. Kino, *Solid immersion microscope*, Appl. Phys. Lett. **57**, 2615 (1990). — p.9, 51, 105, 111.

[2] L. P. Ghislain and V. B. Elings, *Near-field scanning solid immersion microscope*, Appl. Phys. Lett. **72**, 2779 (1998). — p.51, 105, 111.

[3] Q. Wu, G. D. Feke, R. D. Grober, and L. P. Ghislain, *Realization of numerical aperture 2.0 using a gallium phosphide solid immersion lens*, Appl. Phys. Lett. **75**, 4064 (1999). — p.51, 105, 111.

[4] E. Ramsay, N. Pleynet, D. Xiao, R. J. Warburton, and D. T. Reid, *Two-photon optical-beam-induced current solid-immersion imaging of a silicon flip chip with a resolution of 325 nm*, Opt. Lett. **30**, 26 (2005). — p.51, 105, 111.

[5] B. B. Goldberg, A. Yurt, Y. Lu, E. Ramsay, F. H. Köklü, J. Mertz, T. Bifano, and M. S. Ünlü, *Chromatic and spherical aberration correction for silicon aplanatic solid immersion lens for fault isolation and photon emission microscopy of integrated circuits*, Microelectron. Reliab. **51**, 1637 (2011). — p.51, 105, 111.

[6] K. Vigil, Y. Lu, A. Yurt, T. B. Cilingiroglu, T. Bifano, M. S. Ünlü, and B. B. Goldberg, *Integrated circuit super-resolution failure analysis with solid immersion lenses*, Electronic Device Failure Analysis **16**, 26 (2014). — p.51, 105, 111.

[7] E. G. van Putten, D. Akbulut, J. Bertolotti, W. L. Vos, A. Lagendijk, and A. P. Mosk, *Scattering lens resolves sub-100 nm structures with visible light*, Phys. Rev. Lett. **106**, 193905 (2011). — p.27, 52, 54, 58, 60, 62, 68, 69, 75, 76, 78, 92, 105, 111.

[8] I. Freund, M. Rosenbluh, and S. Feng, *Memory effects in propagation of optical waves through disordered media*, Phys. Rev. Lett. **61**, 2328 (1988). — p.27, 58, 69, 97, 106, 112.

[9] S. Feng, C. Kane, P. A. Lee, and A. D. Stone, *Correlations and fluctuations of coherent wave transmission through disordered media*, Phys. Rev. Lett. **61**, 834 (1988). — p.27, 58, 69, 97, 106, 112.

[10] J. R. Fienup, *Reconstruction of an object from the modulus of its Fourier transform*, Opt. Lett. **3**, 27 (1978). — p.29, 71, 99, 106, 112.

[11] J. R. Fienup, *Phase retrieval algorithms: A comparison*, Appl. Opt. **21**, 2758 (1982). — p.29, 71, 78, 99, 106, 112.

[12] R. P. Millane, *Phase retrieval in crystallography and optics*, J. Opt. Soc. Am. A **7**, 394 (1990). — p.29, 71, 72, 106, 112.

[13] Y. Shechtman, Y. C. Eldar, O. Cohen, H. N. Chapman, J. Miao, and M. Segev, *Phase retrieval with application to optical imaging: A contemporary overview*, IEEE Signal Processing Mag. **32**, 87 (2015). — p.29, 72, 99, 106, 112.

[14] J. Bertolotti, E. G. van Putten, C. Blum, A. Lagendijk, W. L. Vos, and A. P. Mosk, *Non-invasive imaging through opaque scattering layers*, Nature **491**, 232 (2012). — p.27, 28, 29, 38, 58, 69, 72, 99, 106, 112.

[15] X. Yang, Y. Pu, and D. Psaltis, *Imaging blood cells through scattering biological tissue using speckle scanning microscopy*, Opt. Express **22**, 3405 (2014). — p.27, 29, 69, 72, 106, 112.

[16] O. Katz, P. Heidmann, M. Fink, and S. Gigan, *Non-invasive single-shot imaging through scattering layers and around corners via speckle correlations*, Nature Photon. **8**, 784 (2014). — p.27, 29, 69, 72, 106, 112.

[17] S. A. Goorden, J. Bertolotti, and A. P. Mosk, *Superpixel-based spatial amplitude and phase modulation using a digital micromirror device*, Opt. Express **22**, 17999 (2014). — p.106.

[18] B. Škorić, A. P. Mosk, and P. W. H. Pinkse, *Security of quantum-readout pufs against quadrature based challenge estimation attacks*, Int. J. Quantum Inf. **11**, 135401 (2013). — p.106.

[19] S. A. Goorden, M. Horstmann, A. P. Mosk, B. Škorić, and P. W. H. Pinkse, *Quantum-secure authentication of a physical unclonable key*, Optica **1**, 421 (2014). — p.106.

[20] T. J. Huisman, S. R. Huisman, A. P. Mosk, and P. W. H. Pinkse, *Controlling single-photon fock-state propagation through opaque scattering materials*, Appl. Phys. B **116**, 603 (2013). — p.106.

[21] S. R. Huisman, *Light control with ordered and disordered nanophotonic media*, Ph.D. thesis, University of Twente, 2013. — p.106.

[22] D. Akbulut, *Measurements of strong correlations in the transport of light through strongly scattering materials*, Ph.D. thesis, University of Twente, 2013. — p.12, 106.

[23] S. W. Hell and J. Wichmann, *Breaking the diffraction resolution limit by stimulated emission: Stimulated-emission-depletion fluorescence microscopy*, Opt. Lett. **19**, 780 (1994). — p.9, 19, 67, 91, 107.

[24] S. W. Hell, *Far-field optical nanoscopy*, Science **316**, 1153 (2007). — p.9, 19, 67, 91, 107.

Nederlandse samenvatting

In dit proefschrift hebben we nieuwe geavanceerde optische methoden gedemonstreerd op basis van ruimtelijke controle over coherent licht voor toepassingen van focusseren en optisch afbeelden met hoge resolutie die baat hebben bij willekeurige lichtverstrooiing door wanordelijke fotonische materialen. Hier vatten we al het onderzoek in dit proefschrift samen.

We hebben optimaal focusseren van coherent licht door verstrooiiende materialen in de aanwezigheid van experimentele ruis gedemonstreerd. In wavefront shaping experimenten veroorzaakt ruis meetfouten in de fase van het doorgelaten lichtveld. We gebruikten een twee-staps optimalisatieprocedure om de fouten in de meting van de optimale fase van het doorgelaten lichtveld te minimaliseren. We ontdekten dat een twee-staps optimalisatieprocedure de uitleesruis van de camera onderdrukt en het experiment in het hagelruis regime brengt. Daaruit concludeerden we dat een wavefront shape experiment altijd hagelruis-gelimiteerd is met een twee-staps optimalisatieprocedure. We toonden aan dat de versterkingsfactor evenredig is met de wortel uit het totale aantal gedetecteerde foto-electronen in een wavefront shape experiment. In gevallen waarin het verstrooiende materiaal dynamisch is, zoals in wolken en biologisch weefsel, is het totale aantal fotonen (het foton budget) dat gemeten kan worden fundamenteel beperkt door de decorrelatietijd van het materiaal en door het laservermogen. Daardoor geeft hagelruis de fundamentele limiet voor de meetbare informatiedichtheid. Onze resultaten brengen nieuwe inzichten in wavefront shaping experimenten vanuit een informatie-theoretisch perspectief.

Hoge-index substraten van silicium (Si) of galliumfosfide (GaP) zijn essentiële materialen voor hoge-resolutie immersiemicroscopie [1–6]. Een verstrooiende immersielens is gemeld met een sub-100 nm resolutie voor zichtbaar licht [7]. De hoge resolutie van de immersielens komt door het injecteren van hoge interne hoeken in het hoge-index substraat door middel van willekeurige lichtverstrooiing. De voorheen gebruikte immersielens is zeer inefficiënt door de optisch dikke verstrooiende laag. Wij hebben de vraag beantwoord of een ongepolijst ruw oppervlak voldoende kan zijn voor verstrooiing naar hoge interne hoeken. Tot nu toe was er geen handige methode om immersielensen te karakteriseren. Wij hebben een nieuwe optische karakterisatiemethode ontwikkeld die het meten van verstrooiing naar hoge interne hoeken in hoge-index substraten mogelijk maakt. We hebben bevestigd dat een immersielens met een ongepolijst ruw oppervlak tenminste zo goed is als een immersielens met een dikke verstrooiende laag voor optisch afbeelden met sub-100 nm resolutie.

Wij hebben spikkel correlatie resolutie verbetering (SCORE) afbeelden ont-

wikkeld dat fluorescentie afbeeldingen maakt met zowel een groot beeldveld als een hoge resolutie. SCORE is een scannende optische microscopie methode die gebruikt maakt van een speckle correlatie effect, bekend als het optische geheugen effect [8, 9], om een hoge resolutie spikkelpatroon over een fluorescent object te scannen. De hoge resolutie van SCORE is te danken aan de zeer fijne spikkelpatronen die gemaakt worden door het immersiemateriaal dat bestaat uit een galliumfosfide (GaP) substraat met een verstrooiende laag. Het grote beeldveld van SCORE is een gevolg van het grote beeldveld van de detectieoptiek. In essentie is SCORE een computationele afbeeldingsmethode die gebruikt maakt van een nieuw fase verwervingsalgoritme dat wij ontwikkeld hebben. Voorheen gerapporteerde vergelijkbare fase verwervingsalgoritmes lijden onder dubbelzinnigheden die stagnatie van het algoritme [10–13] of triviale spiegelingen en verplaatsingen [14–16] veroorzaken. In SCORE gebruiken we standaard afbeeldingen als extra informatie voor ons algoritme, waardoor de oplossing uniek is zelfs voor objecten met een complexe structuur. SCORE is robuust ten aanzien van optische vervormingen en drift. De statistische natuur van spikkelpatronen maakt aberratie-vrij afbeelden met hoge resolutie mogelijk in standaard omstandigheden.

Strevend naar het verder verbeteren van de hoge resolutie van SCORE hebben wij een methode ontwikkeld en gepresenteerd voor het maken van hoge-resolutie fluorescentie afbeeldingen gebaseerd op belichting met een periodieke structuur door een verstrooiende laag. Onze fluorescentie afbeeldingsmethode met een groot beeldveld en een hoog contrast maakt het afbeelden van oppervlakken en grensvlakken van nanostructuren mogelijk met sub-Abbe-resolutie en heeft een theoretische resolutie van 75 nm. In onze eerste demonstratie hebben we een significante verbetering van zowel de resolutie als het contrast laten zien, hoewel we de theoretische limiet nog niet bereikt hebben.

Bibliografie

[1] S. M. Mansfield and G. S. Kino, *Solid immersion microscope*, Appl. Phys. Lett. **57**, 2615 (1990). — p.9, 51, 105, 111.

[2] L. P. Ghislain and V. B. Elings, *Near-field scanning solid immersion microscope*, Appl. Phys. Lett. **72**, 2779 (1998). — p.51, 105, 111.

[3] Q. Wu, G. D. Feke, R. D. Grober, and L. P. Ghislain, *Realization of numerical aperture 2.0 using a gallium phosphide solid immersion lens*, Appl. Phys. Lett. **75**, 4064 (1999). — p.51, 105, 111.

[4] E. Ramsay, N. Pleynet, D. Xiao, R. J. Warburton, and D. T. Reid, *Two-photon optical-beam-induced current solid-immersion imaging of a silicon flip chip with a resolution of 325 nm*, Opt. Lett. **30**, 26 (2005). — p.51, 105, 111.

[5] B. B. Goldberg, A. Yurt, Y. Lu, E. Ramsay, F. H. Köklü, J. Mertz, T. Bifano, and M. S. Ünlü, *Chromatic and spherical aberration correction for silicon aplanatic solid immersion lens for fault isolation and photon emission microscopy of integrated circuits*, Microelectron. Reliab. **51**, 1637 (2011). — p.51, 105, 111.

[6] K. Vigil, Y. Lu, A. Yurt, T. B. Cilingiroglu, T. Bifano, M. S. Ünlü, and B. B. Goldberg, *Integrated circuit super-resolution failure analysis with solid immersion lenses*, Electronic Device Failure Analysis **16**, 26 (2014). — p.51, 105, 111.

[7] E. G. van Putten, D. Akbulut, J. Bertolotti, W. L. Vos, A. Lagendijk, and A. P. Mosk, *Scattering lens resolves sub-100 nm structures with visible light*, Phys. Rev. Lett. **106**, 193905 (2011). — p.27, 52, 54, 58, 60, 62, 68, 69, 75, 76, 78, 92, 105, 111.

[8] I. Freund, M. Rosenbluh, and S. Feng, *Memory effects in propagation of optical waves through disordered media*, Phys. Rev. Lett. **61**, 2328 (1988). — p.27, 58, 69, 97, 106, 112.

[9] S. Feng, C. Kane, P. A. Lee, and A. D. Stone, *Correlations and fluctuations of coherent wave transmission through disordered media*, Phys. Rev. Lett. **61**, 834 (1988). — p.27, 58, 69, 97, 106, 112.

[10] J. R. Fienup, *Reconstruction of an object from the modulus of its Fourier transform*, Opt. Lett. **3**, 27 (1978). — p.29, 71, 99, 106, 112.

[11] J. R. Fienup, *Phase retrieval algorithms: A comparison*, Appl. Opt. **21**, 2758 (1982). — p.29, 71, 78, 99, 106, 112.

[12] R. P. Millane, *Phase retrieval in crystallography and optics*, J. Opt. Soc. Am. A **7**, 394 (1990). — p.29, 71, 72, 106, 112.

[13] Y. Shechtman, Y. C. Eldar, O. Cohen, H. N. Chapman, J. Miao, and M. Segev, *Phase retrieval with application to optical imaging: A contemporary overview*, IEEE Signal Processing Mag. **32**, 87 (2015). — p.29, 72, 99, 106, 112.

[14] J. Bertolotti, E. G. van Putten, C. Blum, A. Lagendijk, W. L. Vos, and A. P. Mosk, *Non-invasive imaging through opaque scattering layers*, Nature **491**, 232 (2012). — p.27, 28, 29, 38, 58, 69, 72, 99, 106, 112.

[15] X. Yang, Y. Pu, and D. Psaltis, *Imaging blood cells through scattering biological tissue using speckle scanning microscopy*, Opt. Express **22**, 3405 (2014). — p.27, 29, 69, 72, 106, 112.

[16] O. Katz, P. Heidmann, M. Fink, and S. Gigan, *Non-invasive single-shot imaging through scattering layers and around corners via speckle correlations*, Nature Photon. **8**, 784 (2014). — p.27, 29, 69, 72, 106, 112.

Acknowledgements

"Books break the shackles of time. A book is proof that humans are capable of working magic," says Carl Sagan. This book is not only a product of four years of hard work, but also a signature of collaboration, support, and friendship. I would like to acknowledge people who are a part of this book.

I gratefully acknowledge my supervisor Allard Mosk for his invaluable advice, guidance, and support. Allard, I know that I'm very lucky to have the opportunity to do science with you. You are a great scientist and teacher. Beside your deep knowledge in science, your enthusiasm and energy triggered several interesting ideas during our discussions. I also thank you very much for your understanding and support when I have difficult times because of my health issues.

I would like to express my gratitude to Willem Vos who showed me the value of sincere discussion during a learning procedure. Willem, thank you for being the person that who always tells me the truth, even when the truth hurts. Your advice about seeing the big picture and considering different dimensions of life while doing research are invaluable. I also would like to acknowledge Ad Lagendijk for his critical and inspiring comments during group meetings.

I would like to thank Emre Yüce for his guidance before I start to work at COPS. Emre, thank you for suggesting me applying for a job in such a great research group. I would like to thank you also for your friendship and support.

I acknowledge my colleagues with whom I had the opportunity to have valuable scientific discussions; Amandev, Andreas, Bergin, Bill, Devashish, Diana, Elahe, Evangelos, Femi, Georgios, Ivo, Jan, Jeroen, Jin, Jochen, Jorge, Klaus, Kurt, Lyuba, Marcel, Maryna, Michael, Muharrem, Naser, Paul, Pepijn, Raheleh, Ravitej, Sanli, Sergei, Simon, Sina, Thomas, Timmo, Tom, Tristan, Vanessa, Willem Tjerkstra, Yin, Yonatan, Youwen, and Yuwei.

The research I present in this book is an inspiration from a breakthrough in optical science: wavefront shaping. I deeply thank Ivo for his great PhD research. I also would like to acknowledge Bas, Duygu, Elbert, Henri and Jacopo who patiently listened to my questions and ideas even when they were slightly crazy. Duygu, I learned a lot from our discussions. I appreciate your patience even when I ask you trivial questions. Elbert, thank you for your kind help during your very busy thesis writing procedure. I'm amazed both by your experimental and theoretical skills in science. Jacopo, whatever I write here probably it will not be enough to express my gratitude to you. I asked so many questions to you that, I think only a very small fraction of people could be patient to listen to me. Whenever I asked you a scientific question, you never turned your back on me.

I'm very lucky to meet you not just because you are a very good scientist, but you are also a very good friend. Bas, I think we both have a lot of impact on each other both scientifically and socially. Our friendship is very precious for me. I also would like to thank Henri for his time to teach me a lot of new physics. Henri, I thank you also for your invaluable friendship.

I would like to acknowledge Cock Harteveld for his crucial support on technical issues in the lab. Cock, I thank you also for your friendly help when I moved to a new place. I also acknowledge Marlon for his support on computer related issues. I acknowledge Marscha, Nilda, and Nienke for their assistance on paper work at COPS. Nilda, I miss our interesting conversations during coffee breaks.

I would like to thank my friend Sezer for his help when I first arrived in the Netherlands. I also would like to thank my friend and housemate Recep for his understanding and support for more than three years during my PhD. We have shared a lot of interesting and funny experiences that I will never forget. I would like to thank Engin, Özlem, and Eren for their support and solidarity during the Gezi protests in Turkey which changed my opinions on many things fundamentally. I would like to thank Eren also for being my paranymph.

Hayatta başardığım hiçbir şey beni sevgiyle ve mutlulukla büyüten ailemin emeği olmadan var olamazdı. Bana koşullar ne olursa olsun inanan ve destek olan aileme sonsuz teşekkür ediyorum. Anne, baba, Ozan bana sevmeyi ve dost olmayı sizler öğrettiniz. Sizler benim her zaman en değerli dostum olacaksınız.

Hasan

Advanced Optical Imaging with Scattering Lenses

Hasan Yılmaz